TOWARD IMPROVED COCHLEAR IMPLANT INSERTION USING MAGNETIC GUIDANCE

by

James R. Clark

A thesis submitted to the faculty of
The University of Utah
in partial fulfillment of the requirements for the degree of

Master of Science

Department of Mechanical Engineering

The University of Utah

May 2011

ProQuest LLC
789 East Eisenhower Parkway
P.O. Box 1346
Ann Arbor, MI 48106-1346

The University of Utah Graduate School

STATEMENT OF THESIS APPROVAL

The thesis of **James R. Clark**

has been approved by the following supervisory committee members:

Jake J. Abbott	, Chair	**1/13/11** Date Approved
Stephen A. Mascaro	, Member	**1/13/11** Date Approved
Frank M. Warren	, Member	**1/9/11** Date Approved

and by **Tim A. Ameel**, Chair of the Department of **Mechanical Engineering**

and by Charles A. Wight, Dean of The Graduate School.

ABSTRACT

The human cochlea is a tiny spiral-shaped structure located within the inner ear. In a fully functioning human auditory system, sound wave vibrations propagate through the cochlea and move tiny hair cells. These movements send signals through the auditory nerve that are interpreted by the brain as sound. If these hair cells or other important structures in the cochlea are damaged, sound information may not be transferred correctly to the auditory nerve, resulting in sensorineural hearing loss. A cochlear implant (CI) can provide hearing ability to an individual by stimulating the auditory nerve with electrical impulses delivered via an electrode array inserted into the scala-tympani (ST) chamber of the cochlea. During insertion, delicate cochlear structures can be damaged, which can lead to loss of residual hearing, infection, and decreased implant effectiveness. In this thesis, we propose a CI magnetic steering concept in which a magnetically tipped CI electrode array is guided through the ST during insertion. A rotating-permanent-magnet (RPM) manipulator, consisting of a large permanent magnet attached to a motor, is used to apply magnetic force and torque to the implant tip, causing it to bend during insertion and avoid contact with the ST walls. We describe the principles of magnetic guidance and propose two steering methods (maximum-field, maximum-torque). We create a scaled-up magnetically tipped implant prototype and a custom 3:1 scale ST phantom, and we use these in insertion experiments to validate our magnetic steering methods. We record insertion forces during nonguided and magnetically guided insertion experiments and compare the results. The data show that magnetic steering can result in reduced implant-ST contact and insertion force. For the data in the insertion depth range from 20 mm to 74 mm, we achieved mean force magnitude reductions of 47.4% and 58.2% using the maximum-field and maximum-torque steering methods, respectively. A reduction in

insertion force indicates that insertion trauma would likely be reduced. Although we expect to achieve a greater reduction in force through implant and steering-strategy improvements, the promising results presented in this thesis represent the first steps toward improved cochlear implant insertion using magnetic guidance.

CONTENTS

LIST OF FIGURES

LIST OF TABLES

ACKNOWLEDGMENTS

This work was supported in part by the National Science Foundation under grant IIS-0952718. This research is part of a larger collaboration with Dr. Robert Webster at Vanderbilt University.

CHAPTER 1

INTRODUCTION

The human cochlea is a tiny 3D spiral-shaped structure with $2\frac{1}{2}$ to $2\frac{3}{4}$ turns [1] located within the inner ear, and is divided into three chambers: the scala vestibuli (SV), scala tympani (ST), and scala media (SM). A cross section of the cochlea showing these chambers and several other cochlear structures is shown in Fig. 1.1. In a fully functioning human auditory system, sound wave vibrations are transferred from the ear drum into the scala vestibuli via three small bones in the inner ear. As these vibrations propagate through the scala vestibuli, they are transferred through a thin membrane (Reissner's membrane) into the scala media. Tiny hair cells in the organ of Corti move due to the vibrations. The movement of these hair cells sends signals through the auditory nerve, which is interpreted by the brain as sound.

Important structures in the cochlea, including the delicate hair cells, can be damaged due to congenital conditions or conditions that occur later in a person's life. Damage to these hair cells or other important structures within the cochlea can inhibit the passing of sound signals to the auditory nerve, decreasing an individual's ability to hear, or causing the individual to be completely deaf. This type of hearing loss, where sound information is not properly sent to the auditory nerve, is referred to as sensorineural hearing loss. If the auditory nerve is intact and functioning properly, a cochlear implant can be used to replace hearing functionality that the damaged cochlear structures cannot provide. Whether hearing loss is due to a congenital condition or experienced later in a person's life, cochlear implantation can provide hearing for an individual of any age.

A cochlear implant (CI) system is shown in Fig. 1.1. The system includes an external microphone and speech processor, a transmitter, an internal receiver, and

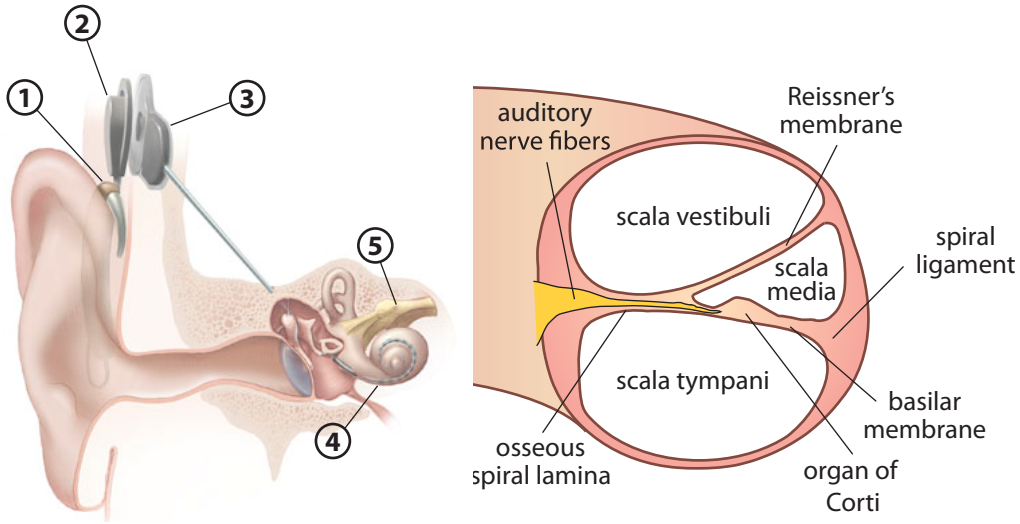

Figure 1.1. Cochlear implant system and cochlea cross section. (left) Cochlear implant system (NIH public domain image with added labels). Labeled items are the (1) microphone and speech processor, (2) transmitter, (3) receiver, (4) electrode array inserted into the cochlea, and (5) auditory nerve. (right) Cochlea cross section diagram showing the location of several cochlear structures.

an electrode array. The microphone, speech processor and transmitter are worn on and behind the patient's ear. Sound information is received by the microphone, decoded by the processor, and sent to the transmitter, which is held in place on the patient's head by a magnet in the receiver, embedded just below the patient's skin. The receiver sends this information to an electrode array, which is inserted into the patient's cochlea. Signals from the receiver are sent as electric impulses to the electrodes in the array, stimulating the auditory nerve. These impulses are interpreted by the brain as sound, effectively providing some hearing ability to the user.

The electrode array of a cochlear implant usually consists of a long silicone carrier with electrodes spaced along its length. The electrode array is optimally inserted into the scala tympani chamber of the cochlea. As the electrode array is inserted into the scala tympani, delicate intracochlear structures are often damaged, which can result in loss of residual hearing and decreased implant effectiveness, especially when the implant deviates into another cochlear chamber. Fig. 1.2 shows causes of intracochlear trauma that can occur during implantation, including tip

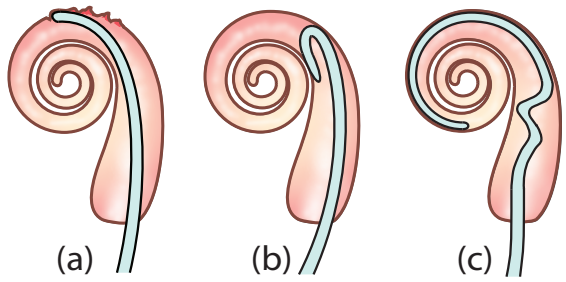

Figure 1.2. Causes of trauma to cochlear structures during implant electrode array insertion. (a) Tip scraping. (b) Tip fold-over. (c) Buckling.

scraping [2], tip fold-over [3], and electrode array buckling [2, 4]. Each of these trauma modes could be decreased or eliminated by steering the implant electrode array during insertion. This would decrease contact between the implant tip and cochlea walls, avoid tip fold over (which occurs when the implant tip gets caught on the inner cochlear wall) and decrease friction between the cochlea and electrode array, avoiding implant buckling.

Decreasing insertion trauma is among the three goals stated by Rebscher et al. [3], which are widely accepted for the development of future cochlear implant (CI) electrode arrays. These goals are (1) deeper insertion into the ST to access lower-frequency cochlear neurons; (2) greater operating efficiency, defined as a reduction in the stimulus charge required to produce a comfortable loudness level; and (3) reduced intracochlear damage associated with surgical insertion. Numerous studies using commercial and experimental implants have been conducted, and CI evaluation and improvement are currently active areas of research.

The CI insertion concept presented in this thesis, described in Chapter 3, utilizes magnetic fields to achieve implant steering. A permanent magnet embedded in the tip of the electrode array is manipulated during insertion using a magnetic field applied by a large external magnet. Using this technique, implant contact with cochlear structures is reduced, which would lead to reduced intracochlear trauma. In our experiments to validate this insertion method, we use a prototype implant with a small permanent magnet embedded in its tip, discussed in Chapter 4. We insert the implant into a custom 3:1 scale ST phantom described in detail in Chapter

5. Several previous studies have used insertion force measurement as a means to compare electrode designs, evaluate prototype implants, or analyze insertion technique [1, 5–12]. A decrease in electrode-array insertion force indicates that insertion trauma would also be reduced. We record insertion forces for nonguided and magnetically guided insertion experiments and compare the results in Chapter 6. The implant prototype used in these experiments is a model of a free-fitting straight array, but the magnetic guidance principles and techniques employed could be used in future work to guide precurled implants or implants inserted with the aid of a stylet. The work and promising results presented in this thesis represent the first steps toward improved cochlear implant insertion using magnetic guidance.

CHAPTER 2

LITERATURE REVIEW

CI evaluation and improvement are active areas of research. Array modifications and design updates are made in an attempt to meet the three widely accepted goals for the development of future cochlear implant arrays, which are (1) deeper insertion into the ST to access lower frequency cochlear neurons, (2) greater operating efficiency, defined as a reduction in the stimulus charge required to produce a comfortable loudness level, and (3) reduced intracochlear damage associated with surgical insertion [3]. The second goal is achieved in part by placing the electrodes close to the cochlear inner wall, near the auditory nerve stimulation sites. The first and second goals should be met without increasing the incidence of insertion trauma. In this chapter, we discuss several studies focused on evaluating intracochlear trauma and its consequences. We also include descriptions of some commercial array designs, as well as descriptions of experimental arrays and automated insertion techniques developed by other research groups. We cite a study and several patents related to guidance of magnetically tipped devices. Finally, we include a review on different fluids used to mimic the fluid-filled environment of the ST for *in-vitro* CI insertion experiments.

2.1 Insertion Trauma

Multiple studies have been done to evaluate insertion trauma that occurs during CI surgery. These studies have been performed using straight electrode arrays, precurved electrode arrays, and arrays with external positioners. Long and straight free-fitting arrays can achieve deeper insertions, whereas precurved arrays and arrays with positioners are designed to place the electrodes closer to auditory nerve fibers. Different array designs result in varying amounts of intracochlear trauma

during insertion. Two major factors that contribute to the extent of damage during insertion are electrode array design and surgical technique, and aspects of each are discussed here as part of the descriptions of various studies. Several arrays described in these studies are included in Fig. 2.1.

Intracochlear damage can lead to loss of residual hearing [15–18], inner-ear infection [3], and incorrect electrode placement, including implant deviation into the scala media or scala vestibuli, which is noted in several of the studies discussed in this chapter. The studies discussed herein have included the use of living CI patients, post-mortem patient temporal bones, cadaver temporal bones that were not previously implanted, and synthetic ST models used to evaluate insertion forces.

Residual hearing is a patient's remaining natural hearing ability, which may be limited to certain (usually low) frequencies. In cases where a patient has lost the ability to hear high frequencies but still has a natural ability to hear low frequencies using a conventional hearing aid, a combined electric-acoustic stimulation (EAS) solution can be used. This approach is described in [18] and involves stimulation of high frequencies using a CI, and amplification of low frequencies using a hearing aid. The patient tested in their study obtained better results in speech understanding tests using EAS than with either a hearing aid or CI alone and subjectively reported that the EAS hearing sounded the best. Preserving an individual's low frequency hearing ability is important, whether or not the individual uses a hearing aid, so intracochlear trauma that could lead to residual hearing loss should be avoided. In [17], Roland et al. discuss methods to preserve hearing in cochlear implant surgery. Their suggestions include avoidance of cochlear trauma during drilling to access the ST; the use of shorter and thinner atraumatic electrodes; the use of steroids to protect the organ of Corti; and drilling a small cochleostomy (access hole) to prevent electrode buckling and loss of cochlear fluid (perilymph).

Electrode arrays are inserted into the ST via either a cochleostomy or through the round-window membrane, which is located at the basal end of the ST. Illustrations showing the location of the round window and a cochleostomy are shown in Fig. 2.2. Each method has advantages and disadvantages. A cochleostomy is an

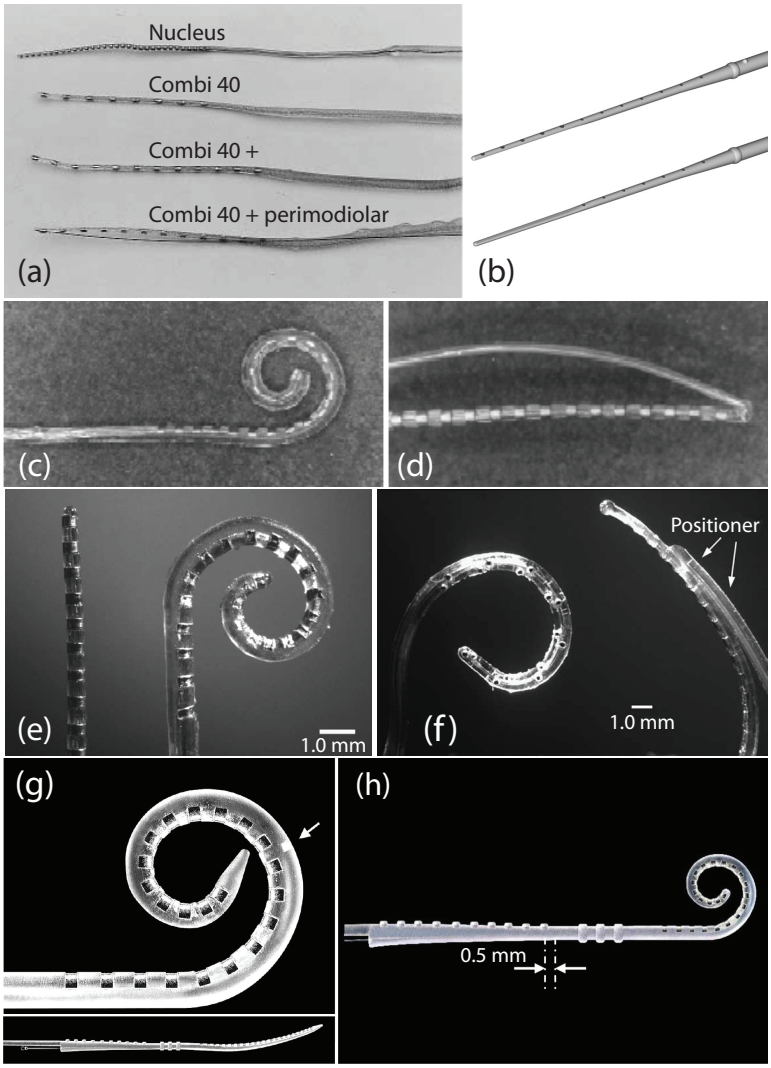

Figure 2.1. Various CI electrode array models. (a) Implants used in [2] reproduced with permission of Taylor & Francis Ltd.; permission conveyed through Copyright Clearance Center, Inc. (b) Electrodes used in [5] (reproduced with permission from Sage Publications): (top) C40+ electrode. (bottom) Flex^{soft} electrode. (c) Precurved array from [13], which was straightened using polyvinyl alcohol (PVA). (d) Array from [13] with attached Teflon strip. Images (c) and (d) used with permission from Wolters Kluwer Health. (e) Electrodes used in [14]: (left) Nucleus banded. (right) Nucleus Contour. (f) Electrodes used in [15]: (left) Spiral Clarion. (right) HiFocus II. Images (e) and (f) reproduced with permission from Elsevier. (g) Nucleus Contour Advance (images from [11] used with permission from John Wiley & Sons, Inc.): (top) Curled after stylet removal. White arrow shows marker to indicate where stylet removal should begin during an advance off-stylet (AOS) insertion. (bottom) Straightened with stylet in place. (h) Nucleus Contour from [1] (© 2007 IEEE).

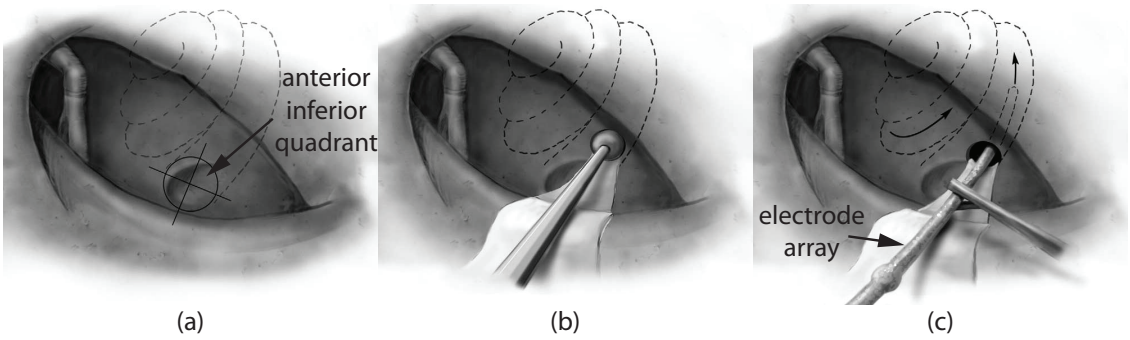

Figure 2.2. Illustrations from [17] showing preparation of a cochleostomy (labels added). The dashed lines show the outline of the cochlea. (a) Round-window niche, in which the round-window membrane is located, divided into quadrants. (b) Cochleostomy drilling. (c) Electrode-array insertion. Illustrations reproduced with permission from Elsevier.

access hole optimally drilled anterior and inferior to the round-window membrane. If the drilling causes disturbance of the fluids between the scala vestibuli and scala media, residual hearing loss may occur [16]. An implant inserted through a cochleostomy may not stimulate some basal cochlear nerve fibers, which could be important for hearing in some individuals [19]. Also, the implant can be mistakenly placed in the scala vestibuli through a cochleostomy approach [20]. Because of the incidence of basal cochlear trauma, which can occur during cochleostomy drilling, Adunka et al. [16] conducted a trauma study focused on round-window membrane insertions. Paprocki et al. [19] suggest that in cases where natural hearing preservation is desired, the round-window membrane should remain intact and a cochleostomy should be used. Adunka et al. state that hearing preservation was achieved in one of their studies in several patients who were implanted using a cochleostomy approach, but they also cite a study in which hearing preservation was preserved in patients implanted via the round-window membrane, showing that preservation can be achieved with round-window insertions. They showed that insertions done via the round-window membrane can cause less trauma to the basal cochlear region than cochleostomy insertions. A study by Roland et al. [21] examined the aspects of round-window insertion that can make insertion difficult, including variation in round-window dimensions and the bony structures

that surround the membrane. These bony structures can cause the implant to point toward the cochlear inner wall or toward the basilar membrane as it is inserted. Drilling these structures allows the implant to be inserted directly down the ST channel, avoiding contact with the cochlear inner wall. The required amount of drilling is minimal but should be performed with care to prevent cochlear damage.

A trauma study using temporal bones from CI patients was conducted by Nadol et al. [22]. They used specimens from eight patients who had been implanted with early models of straight multichannel electrodes via cochleostomy insertions, in some cases into the scala vestibuli and in others into the ST. The study revealed that in all cases the electrode array had caused damage to delicate cochlear structures, and that in three cases the electrode array traversed the plane of the basilar membrane, passing from one scalae into the other, but this did not have any obvious effect on implant performance in those patients. The group also reported that new bone growth and formation of a fibrous sheath surrounding the electrode array were common, and that at least some new bone formation seen after implantation was caused by insertion trauma. There was no obvious correlation between new bone growth in the cochlea and the results of speech comprehension tests for the patients in their study. Patient residual hearing, however, was not evaluated or discussed in the study but could be affected by cochlear trauma, as has already been discussed.

Adunka et al. [5] used cadaveric human temporal bones in their study and focused on the impact of electrode insertion depth on intracochlear trauma. They compared results of insertion experiments using two types of electrodes (C40+ and Flex^{soft}, shown in Fig. 2.1(b)), and forceful and nonforced insertion techniques. Their study indicated that the likelihood of intracochlear trauma increases with increased insertion depth, especially when insertion is continued after the point of first perceived resistance. The Flex^{soft} electrode used in their experiments had a modified tip, specifically designed to be more flexible and have decreased volume. Their findings indicate that modifying the tip in this way led to deeper insertions and less trauma, but they suggest that the increased flexibility could impair the surgeon's ability to sense insertion resistance, possibly tempting further advance-

ment of the implant and causing additional damage. The group suggests that insertions using pre-curved electrodes may result in less traumatic insertions by avoiding outer cochlear wall contact, but insertion depths for these arrays do not exceed 1 full cochlear turn. The group noted that deeper insertions are desirable so that apical regions of the cochlea can be stimulated, which as been shown to be important in speech discrimination in some studies. A study by Gani et al. [23], however, indicates that deep insertions may not always be beneficial. In their study, five Med-El CI users with implanted Combi40+ electrode arrays were tested in vowel and consonant identification. Insertion depths ranged from 605° to up to two full cochlear turns (720°). Two of the five subjects showed significant improvements when the two or three deepest electrodes were deactivated. The group suggests that the deepest electrodes could have been causing pitch confusion: each electrode may have been stimulating some of the same auditory nerve fibers for different pitches. They also suggest that, with the deep electrodes deactivated, the accuracy of mapping sound frequencies to each electrode's stimulation site may have been improved. The group notes that this study demonstrates that deep electrode insertions were not necessarily beneficial with the sound-analysis filters (processors) used by the patients in the study, but that when the processors are able to transmit lower frequencies (e.g., 70 Hz), speech-recognition tests will be of major interest. From these observations, it seems that deep insertions may be more beneficial with improved CI technology.

Several cochlear implant models have been designed to hug the cochlear inner wall. These types of electrodes are often referred to as perimodiolar arrays because they place the array stimulating electrodes near the cochlear inner wall, close to the modiolus. The advantages of such electrodes are: (1) they place the stimulating electrodes close to the auditory nerve, reducing necessary stimulation thresholds; and (2) with some designs, contact with the outer cochlear wall can be avoided, which may reduce insertion trauma [5]. Several studies have been done that include the use of commercial and experimental perimodiolar electrode models [2, 13–15, 24, 25].

A study conducted by Tykocinski et al. [13] included one straight standard electrode array (Melbourne/Cochlear Mini 22 Cochlear Implant) and three different perimodiolar electrode designs. Two of the perimodiolar arrays were precurved and employed different strategies to straighten the array before insertion. One precurved array was inserted using an introducer that held the electrode straight during implantation. The array was designed to reassume its precurved form after the tool was removed. The other precurved array was straightened using a coat of polyvinyl alcohol (PVA), a polymer, which would soften and dissolve after contacting the perilymph fluid within the cochlea, allowing the electrode array to curl into its precurved shape after insertion (Fig. 2.1(c)). The last type of perimodiolar array was a standard array fitted with a Teflon positioner connected to the electrode array tip (Fig. 2.1(d)). After insertion, the Teflon strip was further advanced into the cochlea, pressing against the outer cochlear wall and positioning the stimulating electrodes against the cochlear inner wall. Each perimodiolar array positioned the array closer to the modiolus than the standard straight array and did so with varying degrees of intracochlear damage. The most severe damage was caused by the standard array fitted with the Teflon positioner, which broke through the basilar membrane and caused the positioner and array to project into the scala vestibuli. Surgeons noted that using the insertion tool to insert both the precurved array and the straight array with the Teflon positioner decreased their ability to feel resistance during insertion. Tykocinski et al. suggest that this reduction in resistance sensitivity could contribute to the damage that occurred when inserting the implant with the Teflon positioner. They also suggest that the damage associated with this array could be due to the relative stiffness of the Teflon strip, which was less flexible than the electrode array. The precurved array with the introducer required a larger cochleostomy and did not assume a complete perimodiolar shape after insertion. The precurved array coated with PVA had a final position close to the modiolus, but the authors of the study note that the PVA coating could be problematic since it could flake off before insertion or dissolve earlier than desired. The group concluded that none of the perimodiolar designs

tested fulfilled all three criteria of being easy, safe, and atraumatic to implant.

Gstoettner et al. [2] compared the intracochlear position and trauma associated with several electrode models, which are shown in Fig. 2.1(a). They implanted human cadaver temporal bones with straight electrodes (Nucleus, Combi 40/Combi 40+), and an electrode designed to place the electrode in a perimodiolar position: the Combi 40+ perimodiolar (PM) electrode. The perimodiolar electrode was a developmental model inserted with a nitinol wire in place. After insertion, the wire was held in place and the electrode array was retracted, positioning it close to the inner cochlear wall, and the wire was fixed to the array to maintain this curved position. The final position of the three straight arrays was close to the ST outer wall. The Nucleus array was in close contact with the spiral ligament and basilar membrane near its tip, and the Combi 40 electrodes were in contact with these structures over the entire length of the inserted electrode. Forced insertions (i.e., inserting beyond the point of first resistance) with these electrodes showed that the tip of the Nucleus electrode tended to embed into the outer cochlear wall, and the Combi 40/Combi 40+ electrodes kinked within the ST basal turn, resulting in increased trauma. The Combi 40+ perimodiolar electrode had a final position that was close to the ST inner wall, but cochlear trauma was caused by the nitinol wire pressing against the outer cochlear wall and structures.

Another study by Gstoettner et al. [24] showed that, although the electrodes used in their study achieved near perimodiolar position, the different insertion techniques caused a certain amount of cochlear trauma. The Nucleus 24 Contour (Cochlear) electrode is preformed in a curled, modiolus-hugging shape. It is straightened using a stylet (e.g., a long, thin, stiff wire running through the implant), which is removed during or following insertion to allow the array to curve around the inner wall of the cochlea. The Clarion Preformed electrode (Advanced Bionics) is also preshaped. An insertion tool is used to straighten the array before insertion, and the array curls around the inner cochlear wall after the insertion tool is released. The Clarion HiFocus (Advanced Bionics) model is inserted with a positioner attached to the back of the implant, which holds the electrodes close

to the modiolus. Since the Contour model incorporates a stylet inside the array, a smaller choleostomy is needed for insertion as compared to the Clarion Preformed model, which uses an insertion tool. The Clarion Preformed model with a positioner showed better modiolus-hugging performance than the Contour model, but at the expense of causing more intracochlear trauma; both of the Clarion models tended to shift toward the scala vestibuli in the middle turn of the cochlea. A Combi 40 perimodiolar model (with nitinol wire positioner) in their study also shifted into the scala vestibuli.

Wardrop et al. [14] compared insertions using the straight Nucleus banded electrode, and the Nucleus Contour array (Fig. 2.1(e)). They found that the Contour array resulted in deeper intracochlear positioning and could achieve perimodiolar positioning, but that the rate of insertion-related trauma was similar to that observed with the straight banded electrode. Insertions using both arrays sometimes resulted in penetration of the basilar membrane implant deviation into the scala vestibuli. The group notes that, in several of the cases where the Contour arrays deviated into the scala vestibuli, the intended improvement in perimodiolar electrode positioning was not achieved. In another study, Wardrop et al. [15] compared insertions using the Spiral Clarion and HiFocus II electrodes (Fig. 2.1(f)). The HiFocus II array featured a positioner that could be attached to the array 4 mm or 6 mm from the implant tip, and was designed to position the electrode stimulating contacts close to the ST inner wall. The study showed that the HiFocus II achieved better preimodiolar proximity than the Spiral Clarion array, and that both arrays could be inserted with minimal trauma to an insertion depth of less than 400°. The authors suggest that the construction of these arrays makes them stiffer in the vertical direction (i.e., parallel to the cochlear central spiral axis), a feature which could resist upward deviation into the scala vestibuli. The group notes, however, that for these atraumatic insertions, the arrays were not inserted to the maximum depth specified by the manufacturer. For deep insertions ($>400°$), both arrays resulted in greater injury, and three of the twenty HiFocus II insertions resulted in array deviation into the scala vestibuli. An evaluation of the HiFocus II cross

section revealed that the combined electrode and positioner dimensions were larger than the ST dimensions in some cases.

A study done by Balkany et al. [25] showed that each of the devices evaluated (Nucleus Contour, Combi 40+PM, and Clarion HiFocus II) were effective at placing the electrodes close to the modiolus, but that each had sections of the array where the electrodes were pushed slightly away from the wall. The precurled Contour electrode pressed on the cochlear wall at the tip, forcing some electrodes away from the wall. The other models, each using a positioner, caused electrodes at the distal end of the array to move away from the wall.

Similar arrays were used in a study by Eshraghi et al. [26]. They inserted five each of the Contour, Combi 40+PM, and HiFocus II perimodiolar arrays into cadaver temporal bones. All three arrays caused observable intracochlear trauma in some insertions, including fracture of the osseous spiral lamina with the Contour and Combi 40+PM arrays, rupture of the basilar membrane with the HiFocus II and Combi 40+PM arrays, and displacement into the scala vestibuli with the Contour and HiFocus II arrays. Although each type of electrode was sometimes successfully placed, each showed significant trauma for some insertions.

Briggs et al. [4] also experimented with a Nucleus Contour precurved electrode array. They first used what is referred to by some authors as the standard insertion technique (SIT) [1,11], during which the platinum stylet is inserted in place within the array to allow the it to follow the outer wall of the cochlea as it is advanced into the ST. After insertion, the stylet is removed and the array returns to its precurved perimodiolar shape. Using this technique, the group observed some incidence of basilar membrane perforation, which they attributed in part to the increased stiffness of the array with the stylet in place. To avoid this damage, the group found that, when resistance is first felt, the stylet can be removed 1 to 2 mm, causing the tip of the array to bend away from the outer cochlear wall, resulting in a more atraumatic insertion as the array is further advanced. If the stylet is removed too far, however, the group notes that there is the possiblity of tip fold-over. The group also notes the difficulty of array reinsertion in the case

of accidental displacement after the array has been inserted. The stylet must be reinserted into the array to allow reinsertion, which requires use of a specific tool and possibly a new stylet.

Todd et al. [1] performed insertion experiments using three insertion techniques: SIT, partial stylet withdrawal insertion described in [4], and another technique called advance off-stylet (AOS). Their study included the use of two different types of arrays: the Nucleus 24 Contour and the Nucleus 24 Contour Advance (Fig. 2.1(g)-(h)). The Nucleus 24 Contour Advance is an updated version of the Nucleus 24 Contour. The Advance features a precurved design with a straitening stylet, but a different insertion technique, AOS, is employed. The Nucleus 24 Contour is inserted using the standard technique, SIT. To avoid outer-cochlear-wall contact and its associated intracochlear damage, AOS was developed and is used when inserting the Advance array. The array is inserted until a mark on the carrier is aligned with the cochleostomy site. The stylet is then held in place while the array is advanced into the cochlea, allowing the array to regain its precurved position as it is being inserted. Using this technique, the array does not slide against the cochlear outer wall during insertion. The advance array also has a modified tip designed to be softer and avoid tip fold-over, which is described in detail in [11]. A series of AOS insertion photographs from [3] is shown in Fig. 2.3.

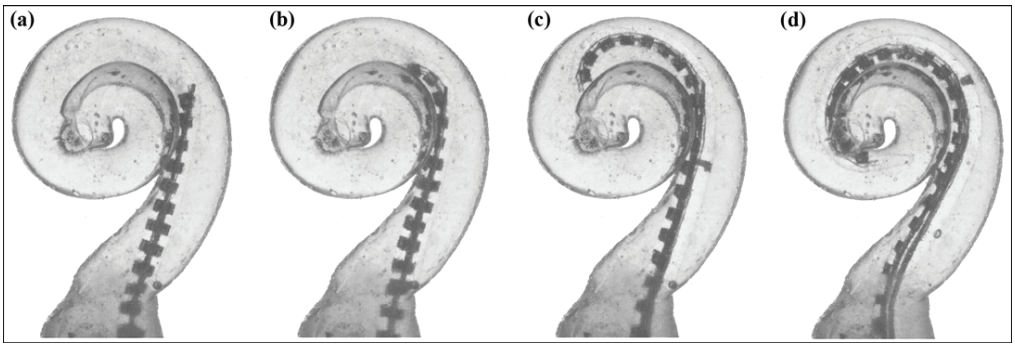

Figure 2.3. AOS insertion, series from [3]. (a) Array and stylet are advanced into the ST. (b) Stylet is held in place while the array is advanced further. (c)-(d) As it is inserted, the precurled array assumes its original shape to achieve a perimodiolar position and avoid contact with the ST outer wall.

In [1], SIT and partial stylet withdrawal were used with the Contour array, and AOS was used with the Advance array. The arrays were inserted into a synthetic ST model which was placed on a load cell to record insertion forces. Reduced insertion forces indicate that insertion trauma would also be reduced. Their results show that SIT resulted in the highest insertion forces. With partial stylet withdrawal, a decrease in insertion force was observed at the point of withdrawal with a steady force increase as the array was further advanced. AOS used with the Advance array showed a notable decrease in forces for nearly the entire insertion procedure with a slight increase in insertion force during the initial insertion attributed to an increase in frictional force as the array slides against the inner cochlear wall. Comparable insertion force results using the same array designs and SIT and AOS techniques are reported in [11]. Experiments were also done to determine the effect of advancing the array off the stylet too early [1]. These experiments showed that early advancement could cause the implant tip to fold over on itself, leading to a non-ideal insertion with an increased chance of inducing trauma. The group used a 1-DOF force sensor in these experiments but suggest that a 6-DOF force sensor be used to capture all force components contributing to the overall insertion force.

Rebscher et al. [3] also reported potential problems with the Advance array and AOS technique. As well as the potential for tip fold-over due to early stylet removal, the group noted that late stylet removal could result in the implant contacting the cochlear outer wall, potentially causing damage. The variability in human cochlea dimensions poses a challenge when using the AOS technique, since the point during insertion when stylet removal should begin can vary between patients. To reduce the risk of trauma, accurate depth of insertion before stylet removal may have to be determined for each patient based on preoperative imaging, which is not currently done in practice.

Including the Cochlear 24 Contour Advance array, Rebscher's report discusses the mechanical properties of eight clinical and prototype CI arrays and summarizes insertion trauma and insertion depth recorded in 79 implanted cadaver temporal bones. A summary of the team's findings is given in Fig. 2.4. The team concluded

Cochlear implant electrode arrays studied.

Electrode	Manufacturer	Type	Scala Tympani Position	No. Studied
Cochlear Banded™	Cochlear Limited	Straight	Lateral	8
Spiral Clarion™	Advanced Bionics	Spiral	Midscala	8
Cochlear Contour ™	Cochlear Limited	Spiral	Perimodular	18
HiFocus II™ with Positioner <400°	Advanced Bionics	Curved with Positioner	Perimodular	14
HiFocus II™ with Positioner >400°	Advanced Bionics	Curved with Positioner	Perimodular	6
Contour Advance™	Cochlear Limited	Spiral	Perimodular	3
Nurobiosys	Nurobiosys	Straight	Lateral	6
Helix™	Advanced Bionics	Spiral	Perimodular	6
Prototype 1	Advanced Bionics	Curved	Midscala	10

Stiffness measurements, insertion damage, and insertion depth.

Electrode	Force (grams)				Trauma Scala Vestibuli (%)	Mean Depth (°)
	V	H	Mean	V/H		
Cochlear Banded™	0.50	0.70	0.60	0.71	37.5	285
Spiral Clarion™	3.27	2.92	3.09	1.15	0.0	445
Cochlear Contour™	1.33	1.97	1.65	0.68	38.9	417
HiFocus II™ with Positioner <400°	1.29	0.47	0.88	2.77	0.0	332
HiFocus II™ with Positioner >400°	1.29	0.47	0.88	2.77	66.6	508
Contour Advance™	1.33	1.97	1.65	0.68	33.0	367
Nurobiosys	1.03	0.58	0.80	1.77	0.0	360
Helix™ Experimental 1	3.58	1.28	2.43	2.79	0.0	390
Helix™ Experimental 2	3.29	1.23	2.26	2.67	10.0	416

H = horizontal, V = vertical.

Figure 2.4. Summary tables from [3] showing electrodes studied, mechanical characteristics, and insertion results including incidence of trauma resulting in array deviation into the scala media or scala vestibuli.

that none of the designs evaluated in the study meet all the criteria for an ideal CI electrode: that the electrode be (1) inserted without damage to the cochlea, (2) reliably inserted to a depth of approximately 1.5 cochlear turns (540° as measured from the round window), and (3) positioned near the modiolus for increased efficiency. The group notes that electrodes with greater proportional stiffness in the vertical plane (parallel to the axis about which the cochlea spirals) were less likely to produce damage. The team also noted that insertion trauma has been shown to increase with insertion depth [5] and, because of channel cross-talk, electrode insertions beyond 1.5 turns may not result in an increase in implant performance, which are potential drawbacks to deep array insertions discussed earlier in this chapter.

2.2 Electrode Array Designs

Several research groups have developed experimental electrode array prototypes. They are designed to achieve a perimodiolar position within the cochlea, and some are actively bent during insertion to minimize insertion trauma.

Researchers at Columbia University have fabricated silicone electrode array prototypes that are actively bent during insertion. The prototypes are actuated using an embedded Kevlar thread which, when pulled, causes the array to curve. The team's goal was to design an implant that can be actively bent to best approximate the shape of the cochlea during insertion, thereby reducing contact with cochlear walls and minimizing insertion forces. Using these prototypes and optimal path planning algorithms for robot-assisted insertion, the researchers have demonstrated the ability to achieve prominently reduced insertion forces compared to forces recorded during insertion trials with the same prototypes inserted without active bending [8, 9]. A diagram of a prototype array is shown in Fig. 2.5.

Researchers at the University of Michigan have developed electrode arrays based on silicon microfabrication technologies. Advantages of fabricating arrays using these technologies include the possibility of including a greater number stimulating electrode sites, integration of on-board position sensors, and batch-fabrication

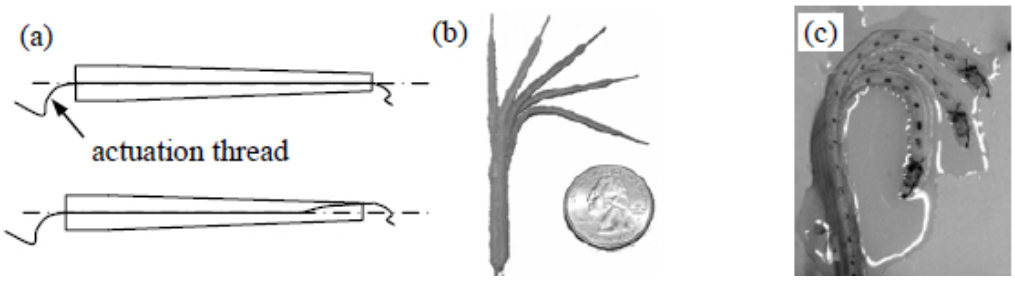

Figure 2.5. Columbia University electrode array prototypes. (a) Top and front view of the electrode, (b-c) Two electrode models with different bending characteristics. Images from [8] used with permission from Springer Science+Business Media.

capabilities for eventual reduced cost. Bell et al. [27] first developed a flexible silicon micromachined electrode array for a cochlear prosthesis. The device was fabricated using standard micromachining processes, and array prototypes were tested in guinea pigs to verify functionality. These arrays were initially fabricated to be straight, and polymeric coatings were added to improve electrode strength and mechanical characteristics. These first prototypes did not include position or curvature sensing, or curvature control, but the group was already looking forward to integrating these features in later-generation devices.

Building on this research, Bhatti et al. [28] produced a steerable electrode array with a multichambered backing device. In its relaxed state, the array assumes a tapered helical shape, which is formed to hug the inner wall of the cochlea. To achieve curvature control, fluid is injected into the chambers at multiple points along the length of the implant, which increases pressure in the chambers and changes the curvature of the device. This allows the device shape to be altered during insertion to minimize forces exerted on the cochlear walls, as well as increase electrode insertion depth and improve modiolar proximity.

The number of stimulating electrodes in current electrode array designs is somewhat limited by the number of electrode lead wires that can be included in the design. Using micromachining technology and the described backing device, the group hoped to create a high-density (i.e., more closely spaced stimulating electrodes) perimodiolar electrode array to provide improved frequency resolution for

better speech perception and perceived sound quality. The group arranged the electrodes in a quadrupolar configuration, in which three collinear electrodes are driven simultaneously, with the two flanking electrodes driven at half the inverse polarity of the center electrode. In this configuration, the team hoped that the resulting field localization would lead to better electrode-pair discrimination and increased speech discrimination, with a high-density array delivering more information along the auditory nerve.

In preparation for the eventual goal of a 128-site, 250-μm pitch array, the team designed a 15-site passive array and tested auditory thresholds during *in-vivo* tests in guinea pigs. Using data from the *in-vivo* testing, the team designed a 32-site active array that would include on-board circuitry for current delivery and data recording.

Wang et al. [29] then embedded micromachined sensors into the previously designed electrode arrays. The sensors include a tip wall contact sensor and eight strain-gauge curvature sensors along the length of the array. The signals read from the tip contact sensor successfully indicated tip contact during the *in-vitro* insertion procedure. Using signals from the curvature-sensing strain gauges, the position of the electrode array could be better than 50 μm at the tip of the array. The team also made improvements to the previous electrode design, making it more flexible and with a better modiolus-hugging shape. The polysilicon piezoresistive position sensors had typical gauge factors of 15, and a group at Michigan [30] explored the use of poly-crystalline diamond piezoresistors to increase the gauge factor. The team achieved a gauge factor of 28 with the new sensors, which would lead to higher sensitivity for position and curvature sensing. More research is being done regarding these new sensors.

Wang et al. [31] developed a method to coat the prosthesis in parylene using a wafer-level process. This allowed the group to successfully encapsulate the prosthesis in parylene, a biocompatible layer, which allowed the electrode array to be flexible and maintain strength.

A paper by P. T. Bhatti and K. D. Wise [32] describes a device that incorporates

many of the features described above, including circuitry details. The prosthesis includes a 32-site high-density four-channel electrode array, eight position sensors, and on-board circuitry for stimulus generation and position-sensing. Fig. 2.6 shows the 32-site array. A 128-site 16-channel human array is under development at the University of Michigan's Engineering Research Center for Wireless Integrated MicroSystems (WIMS-ERC).

Wu et al. [33] developed a curvature controllable electrode array based on bilayer microfabrication technology to achieve a curved deformation during or after the CI surgery. Each layer has a different volume expansion coefficient. The main structure of the electrode is made from gold, silicon-oxide, and SU-8. After fabrication of the main structure, a layer of polypyrrole, a conducting polymer, is deposited on the back of the electrode array. The device is prefabricated in a curved position, formed to hug the inner cochlear wall. When a voltage is applied across the polypyrrole layer, the layer releases Na^+ ions into an aqueous saline solution (similar to to the perilymph fluid inside the cochlea), causing it to shrink and straightening the electrode. This process is shown in Fig. 2.7. During insertion of the electrode array into the cochlea, the precurved shape can be gradually recovered by applying the opposite voltage; Na^+ ions are absorbed, and the increased polypyrrole volume

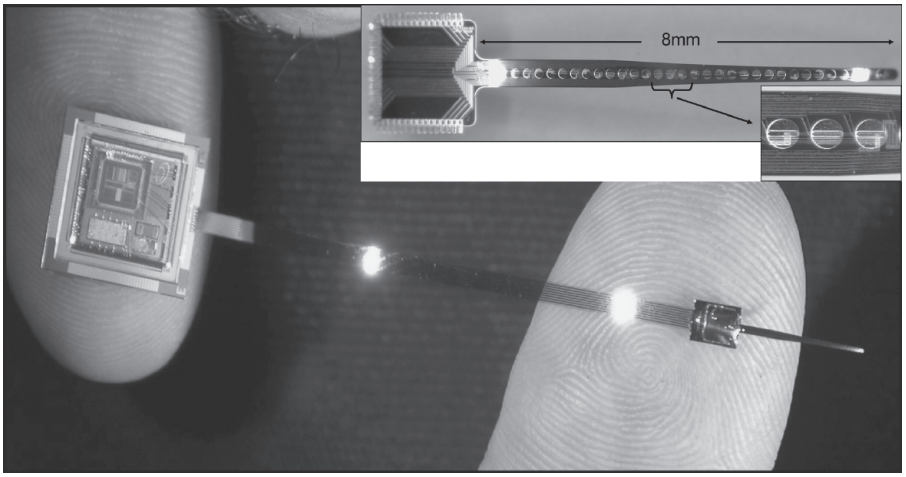

Figure 2.6. The WIMS-ERC cochlear prosthesis. (inset) The 32-site high density electrode array [32] (© 2006 IEEE).

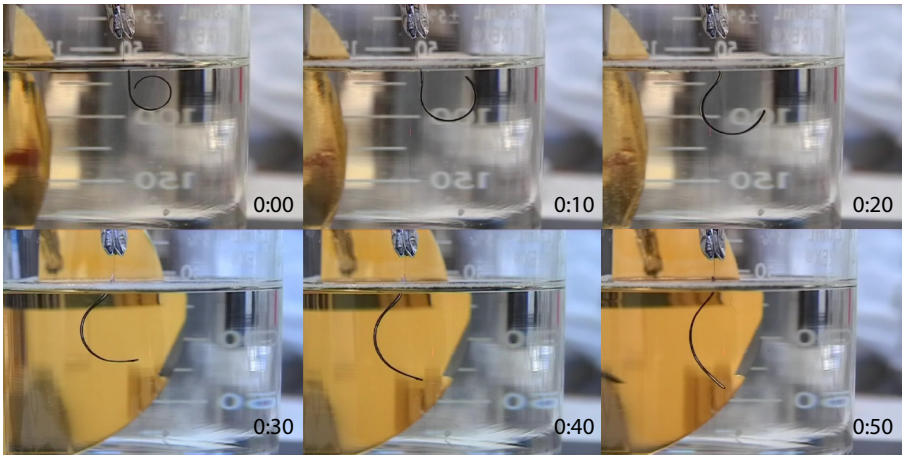

Figure 2.7. Time-lapsed photographs of the device operation in NaCl solution with a 1 volt applied potential over a 50 second time interval. The upper-left image starts at 0:00, and subsequent images were taken at 10-second intervals [33] (© 2005 IEEE).

causes the bilayer electrode to assume its curved, modiolus-hugging shape. Their prototype array has an insertable portion 25 mm long, which would allow insertion around the first turn of the human cochlea.

Another method for curvature control designed for modiolus-electrode proximity has been proposed by Mirzadeh et al. [34]. The implant consists of a hydrophobic section and a hydrophilic section, which are covered in silicone rubber. When the electrode is inserted into a saline solution, the hydrophilic polydimethylsiloxane (PDMS) section absorbs the solution, causing it to increase in volume and detach from the hydrophobic portion of the electrode. The detached PDMS portion presses against the outer cochlear wall and causes the electrode array to curve around the inner wall, as shown in Fig. 2.8(c). The authors of [34] state that this design does not place extra pressure on cochlear walls typical of space-filling or positioner designs because the hydrophilic segment can extrude out of the scala tympani as it swells.

The development of a steerable CI electrode array using shape memory alloy wires is described in [35]. Shape memory alloy (SMA) wires can be bent and heated to a high temperature. When the wire cools to room temperature, it returns to its original straight form. When reheated, the wire assumes its bent position.

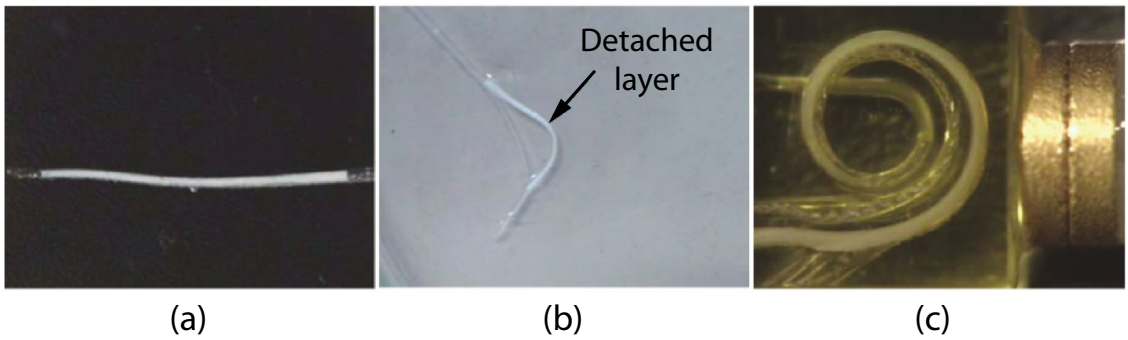

Figure 2.8. Segmented detachable electrode. (a) Before immersion in saline. (b) After swelling in saline. (c) Segmented electrode about 6 hours after insertion into a scala tympani model. Images from [34] used with permission from John Wiley & Sons, Inc.

The authors of [35] used this property of shape-memory-alloy wires to develop an electrode array designed to avoid insertion-induced trauma and to provide a way to optimally place the array within the scala tympani for delivery of neurotrophins (growth factors), which help regenerate auditory neurons lost prior to implant insertion, or neurons lost due to basilar membrane damage during electrode array insertion. The array design consists of three 6 mm lengths of embedded nitinol shape memory alloy wires. Reference [35] describes a 3D finite element model made to evaluate the effectiveness of the design and presents results of simulations of electrode insertions using this model. After the array is inserted up to the first bend of the scala tympani, the most distal SMA wire is activated to bend the array tip away from the basilar membrane and spiral ligament. After the array has been completely inserted, the two other SMA wires are activated to determine the final electrode position, optimized for delivery of neurotrophins. Simulated insertions done using this process showed that the device was effective at avoiding basilar membrane contact and placing the array in a good final position for delivery of neurotrophins.

The electrode array designs described above use mechanical means built into the array to achieve bending. Using a hydrophilic array section that presses against the cochlear outer wall could increase the risk that insertion damage will occur due to those contact forces. The use of an internal thread, external pressure chambers,

bilayer expansion and contraction, and shape-memory-alloy wires could increase the stiffness of the array as it is being inserted. If the array is not formed to fit the ST well or is misdirected down the channel, the increased array stiffness could result in increased intracochlear trauma. Our magnetic steering method does not add this increased stiffness to the array and may provide a more adaptable means of guidance.

2.3 Automating Insertion

Currently, cochlear implant electrode arrays are inserted manually by highly skilled surgeons. There can be wide variability in force application and surgeon technique. This variability could be greatly decreased using robot-assisted insertion techniques, and optimized path planning, insertion speed, and other insertion parameters could be more easily reproduced using robot-assisted insertion. Our magnetic guidance solution could be robotically implemented as either a supervised automated process or a robotics-based system under surgeon manipulation.

Majdani et al. [6] compared forces during insertion of the Cochlear 24 Contour Advance array using surgeon insertion and robotic insertion. Electrodes used in the study were inserted using the AOS technique. A total of 26 manual insertions were performed by three surgeons, and 8 insertions were performed using a custom robotic insertion tool described in detail in [36]. The tool was adapted specifically for use with the Advance array and AOS technique, and consists of two motorized linear stages: one connected to the electrode array silicone carrier using forceps, and the other connected to the the stylet using a hooked wire. Using this tool, the array and stylet can be advanced together up to the point where the stylet should be held in place, and the array can then be further advanced off of the stylet, following the AOS technique. Majdani et al. used a synthetic ST model provided by MED-EL Corp. mounted on a load cell. They recorded insertion forces for the automated AOS insertions and compared these forces with those of the insertions done manually by trained surgeons. Although the results showed an overall greater average insertion force using the robotic insertion tool, there was

greater force variability between surgeon insertions and intermittent force peaks as the array was manually advanced off of the stylet. The robot was able to achieve more repeatable results during the advance-off portion of the procedure.

A force sensing automated insertion tool based on the two-linear-actuator design presented in [36] was developed by Schurzig et al. [12]. Their goal was to create a tool that would ensure safe insertion using integrated force sensing, enable insertion using minimally invasive techniques, and provide a way of identifying optimal electrode deployment profiles and accurately reproducing them. The tool was designed for use with the Nucleus 24 Contour Advance array, inserted using the AOS technique, and provides independent linear control of the electrode silicone carrier and stylet. The design features a custom made force sensor using beam bending and semiconductor strain gauges. The force sensor measures reaction forces during insertion, thereby providing a means of assessing contact between the electrode array and cochlear walls during insertion. During experimentation, the tool provided a maximum deviation between measured and known applied force of 0.003 N. In subsequent experimentation the group used the insertion tool to compare traditional insertion and AOS insertion using a 3D synthetic ST model [12]. Their results showed that AOS insertion was associated with lower average and maximum forces compared to traditional insertion.

Researchers at Columbia University created actively bending array prototypes, which were described earlier in this chapter. In a pilot study using these arrays, the group evaluated the potential benefits of robot-assisted CI surgery. They demonstrated the use of path planning coupled with active array bending using a 1-DOF linear actuator and showed that steering the electrode using 2-DOF (linear translation and active bending) resulted in a reduction of about 70% in the insertion forces as compared to inserting their prototype without active bending [8]. Their path planning algorithm was designed to minimize the shape difference between the inserted portion of the electrode and the cochlea based on mathematical models. In this way, the shape of the implant was actively bent during insertion to best approximate the shape of the ST phantom and reduce insertion forces. A 2D

model of the scala tympani was used in these experiments.

The researchers extended their experiments to explore 4-DOF insertions with the same 2D model [37] and in a 3D model [9]. An experimental robotic insertion system was setup that could provide 2-DOF insertion (as done in [8]) or 4-DOF insertion. Using this system, the group could control insertion depth and electrode bending with 2-DOF control, and angle of approach to the ST, insertion depth, and electrode bending with 4-DOF control. In these studies, the group demonstrated that changing the angle of insertion with respect to the scala tympani was effective in reducing insertion forces using their steerable arrays, showing that using a 4-DOF robot-assisted technique was more effective than a 2-DOF technique. Their results showed that changing the angle of approach may reduce the average insertion forces by up to 40% and the peak force by 19% for 4-DOF insertion vs. 2-DOF insertion.

Another study performed at Columbia University presents a friction model that describes the whole insertion process and investigates the relationship between insertion speed and insertion force [10]. The team developed a mathematical model for straight electrode arrays, which slide along the external wall of the scala tympani during insertion, and used their system of equations and friction models to run insertion simulations for insertion speeds of 0.5 mm/s, 3 mm/s, and 7.5 mm/s. They validated these experiments using commercial straight MedEl electrode arrays. Although the simulated results did not match the experimental results perfectly, results from both approaches showed an overall decrease in insertion force as insertion speed increased. The experimental results showed that the maximal insertion forces were decreased by 24% for $v = 3\,\text{mm/s}$ and 43% for $v = 7.5\,\text{mm/s}$ as compared to $v = 0.5\,\text{mm/s}$. The group suggests that the discrepancy between the simulated and experimental results could be due to hydrodynamic effects in the lubricant, and suggests that analysis on the lubricant's hydrodynamic effect could lead to a further decrease in insertion forces. The collected statistical data from these experiments were used to calculate safety boundaries for insertion speed, which could be used as predictive information for robot-assisted electrode insertion.

2.4 Magnetic Actuation and Guidance

Judy et al. [38] have demonstrated magnetic actuation of polysilicon microstructures. In their experiments, the team fabricated a narrow cantilever beam made of polysilicon that is anchored to the substrate at one end and attached to a wide plate of magnetic material at the other end. When the cantilever structure is placed in a magnetic field, the magnet will rotate to align itself with the direction of the applied field, causing the beam to bend as shown in Fig. 2.9. If the external magnetic field is uniform, the result will be pure torque bending with no linear force component.

The beam curvature depends on the strength and direction of the applied external magnetic field, the geometry and stiffness of the beam, and the characteristics of the magnet fixed to the end of the beam. These magnetic and beam-bending principles can be used to manipulate a magnetically tipped cochlear implant electrode array, providing curvature control during insertion. Details about

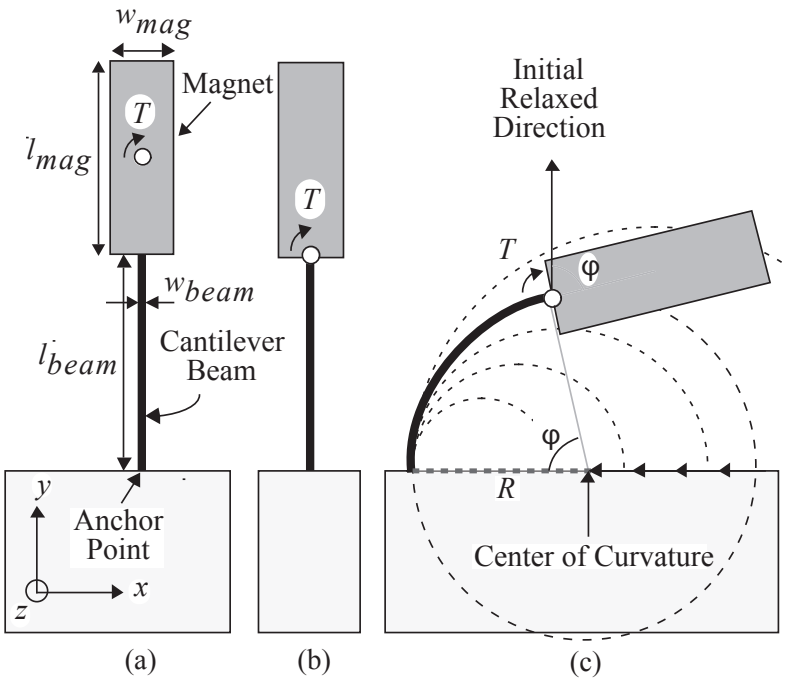

Figure 2.9. Magnetically controlled microdevice [38] (© 1995 IEEE). (a) Mechanical structure of the microactuator. (b) Reduction of the mechanical system. (c) Circular beam bending. The arrows indicate the motion of the center of curvature as the torque T is increased from zero.

magnetic fields and the magnetic principles involved in CI steering are given in Chapter 3.

Stereotaxis, Inc. develops catheters and other interventional devices based on magnetic technologies. Permanent magnets imbedded in these devices are manipulated using external magnetic fields. Reference [39] describes the modeling of such devices containing magnets near their distal tip. For the model, the author assumes that the external field is nearly uniform (negligible field gradient), so the net force on the tip magnet is negligible, and the magnet experiences only a magnetic torque. The author also assumes that the catheter only makes contact with tissue at the catheter tip. When there is tip contact, out-of-plane force components are ignored. The model is based on energy equations, including magnetic potential energy, strain energy of the catheter body, and the strain energy of the deformed tissue. A closed-form solution for the equilibrium configuration is obtained, which enables real-time contact force estimation and control. The position and orientation of the catheter tip is determined in real-time by electromagnetic means, and once the device is at a target point, the control algorithm based on the obtained equations can modify the contact force applied to the tissue. The physician can select anatomical target points, and the algorithm will automatically change the catheter length and orientation to reach those points. The control algorithm is described in more detail in [40], which includes feedback control for a navigation phase and a tissue contact phase. The company holds several patents describing magnetically guided medical devices and concepts. Their innovations include tubes comprised of multiple sections of different flexibility [41], distributing multiple magnets along the length of the device [41–43], including an energizeable coil (electromagnet) on the distal end of the device [42, 44], and attaching a tether to the magnet so that it can be removed after the device has been placed [42, 45].

One patent utilizing magnetic guidance for medical devices describes the use of the device as a cochlear implant [46]. The system consists of a polymer body portion with pieces of magnetic or nonmagnetic material (or both) embedded in the tip, and at least one electronic unit (electrode) in the body of the implant. A

system for controlling movement of the polymer body portion guides the implant through the cochlea utilizing magnetic forces. A diagram of the proposed design is shown in Fig. 2.10. Although the patent mentions the potential use of magnetic forces for guidance, it does not detail how it can be accomplished. It also does not mention the use of magnetic torque, which is described in Chapter 3 and is a key principle of our guidance method.

2.5 Perilymph Fluid

The human ST is filled with a fluid called perilymph fluid, an extracellular fluid with an ionic composition comparable to that of plasma and cerebrospinal fluid. The major cation of the fluid is sodium (Na^+). Research groups have used different aqueous solutions to imitate the perilymphatic fluid found inside the scala tympani. In some studies, a soap solution is used to lubricate the ST and facilitate

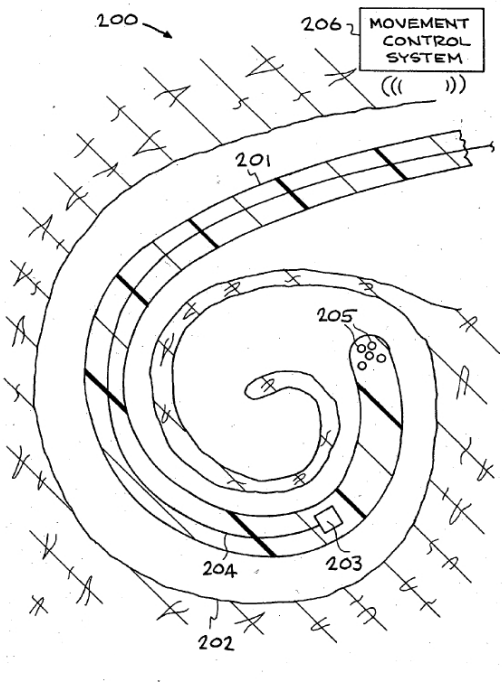

Figure 2.10. Magnetically steered cochlear-implant patent [46]. (200) Proposed cochlear implant system showing (201) the polymer body portion, (202) cochlea structure, (203) electronic unit, (204) circuit connected to the electronic unit, (205) magnetic or nonmagnetic pieces and (206) a system for controlling movement using magnetic forces.

implant insertion. In others, the fluid mimics the saline composition of the actual perilymph.

In a study focused toward force application during implant insertion [1], a soap solution consisting of 10% Bathox and 90% distilled water was used in order to imitate the fluid-filled scala tympani. This solution was used to decrease friction between the implant and scala tympani walls. Majdani et al. [6] also used a soap solution to mimic biological conditions of the ST and minimize friction. Three groups used saline solutions to imitate the perilymph fluid. Wu et al. [33] used a 0.1 M NaCl solution, which is similar to the perilymph environment inside the scala tympani. The group needed a solution containing sodium ions for absorption and desorption, which caused their implant prototype to bend as described earlier in this chapter. Mirzadeh et al. [34] used a saline solution (purchased from Merck), which was needed for water absorption, also described earlier in this chapter. Eshraghi et al. [26] irrigated cadaver cochleae with saline and also infused a small amount of hyaluronic acid lubricant into the cochlear lumen immediately before insertion. Zhang et al. [10] fully filled their scala tympani model with a glycerin solution to simulate *in-vivo* conditions. Their paper cites [47], which provides friction coefficients for a standard straight electrode array inserted into a scala tympani model with and without glycerin.

Physicians at the University of Utah Hospital use a soap solution to lubricate scala tympani models used for CI insertion practice. However, the solution is not physiologic. To approximate perilymph fluid, a salt solution such as IV fluid could be used [48]. The magnetically guided CI insertion procedure described in this thesis does not require the ST to be filled with a saline solution, and we used soap solution to lubricate the ST channel for experiments described in Chapter 6.

CHAPTER 3

MAGNETIC GUIDANCE

3.1 Clinical Concept

CI array steering described in this thesis is achieved using permanent magnets. A clinical concept illustration is shown in Fig. 3.1. To achieve CI steering, a small permanent magnet is embedded in the tip of the implant. A large permanent magnet (manipulator magnet) is used to apply a magnetic torque to the implant tip. The manipulator magnet is attached to a motor with its magnetization direction perpendicular to the axis of rotation. The rotation axis is aligned with the central spiral axis of the cochlea. As the CI array is inserted, the manipulator magnet is rotated to actively bend the implant, directing it away from cochlear walls. The distance between the manipulator magnet and the cochlea can be varied, effectively changing the strength of the applied magnetic field acting on the implant tip.

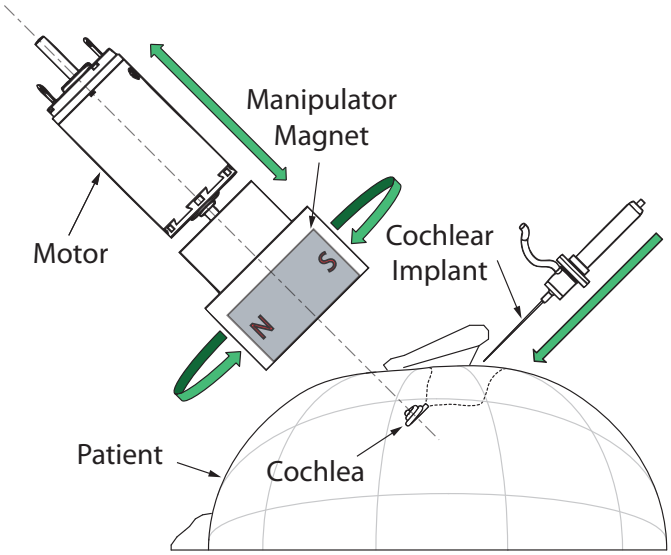

Figure 3.1. Concept for magnetically steered cochlear implant surgery.

The implant prototypes used for insertion experiments in this Thesis are straight, free-fitting arrays, which are not precurled to hug the modiolus after insertion. Images of a prototype free-fitting array insertion, without magnetic steering, are shown in Fig. 3.2. In its relaxed state, the implant is straight (Fig. 3.2(a)). As the implant is advanced into the ST, its tip contacts and scrapes the outer wall (Fig. 3.2(b)). With further insertion, the implant slides along the ST outer wall, conforming to its curved shape (Fig. 3.2(c)). Since the implant is straight in its relaxed state, a mechanical restoring torque due to the stiffness of the implant causes it to press against the ST outer wall as it curls through the chamber. The normal force acting on the wall results in friction according to the equation

$$F_f = \mu N \tag{3.1}$$

where F_f is the frictional force, μ is the coefficient of friction, and N is the normal force. As the implant is inserted further into the chamber, frictional forces build, which can lead to insertion difficulty, buckling, and increased intracochlear trauma.

Magnetic fields can be used to decrease contact forces during CI insertion. The tip of the implant can be directed away from cochlear walls to avoid scraping and tissue damage. Torque applied to the tip of the implant bends it, which decreases the net torque pressing the implant against the wall. The reduced normal force

Figure 3.2. Free-fitting array prototype insertion characteristics. (a) Array is straight in its relaxed state. (b) Tip contact and scraping. (c) Array presses against and conforms to ST outer wall.

leads to a reduction in friction. If the implant is bent away from the wall, the force required for insertion should be reduced, even if the implant is still touching the outer wall. This is shown in the experimental results included in this thesis. If the implant is actively bent enough, the implant is pulled completely away from the ST wall and the normal force, and therefore friction, become zero. Reduced insertion force will likely lead to reduced trauma during CI surgery.

The principles of magnetic guidance for CI insertion described in this chapter were used to guide free-fitting straight arrays during insertion experiments. These same concepts can be used in future work to explore magnetic guidance of other types of CI arrays, including precurled arrays and arrays inserted with the aid of a stylet.

3.2 Magnetic Concepts

3.2.1 Magnetic Fields

Magnetic fields can be described as uniform or nonuniform. In a uniform magnetic field, the field strength and direction are equal everywhere throughout the field. In a nonuniform field, the field strength or direction are not equal everywhere throughout the field. When a permanent magnet is placed in a uniform magnetic field with its dipole direction unaligned with the field direction, a pure torque is exerted on the magnet: only a torque acts on the magnet and no linear magnetic forces act on it in any direction. An unconstrained magnet in a uniform magnetic field will not translate linearly, but will rotate until its dipole direction is aligned with the direction of the applied field. The magnetic field emanating from a permanent magnet, however, is nonuniform; spatial changes exist in field direction and intensity. For a single permanent magnet, the magnetic field strength decreases as distance from the magnet increases, and the field does not point in the same direction everywhere around the magnet, as shown in Fig. 3.3. These spatial changes are referred to as field gradients. As in a uniform field, a torque acts on a magnet placed in a nonuniform field if its dipole direction is unaligned with the field direction. Unlike a uniform field, however, field gradients in a nonuniform field

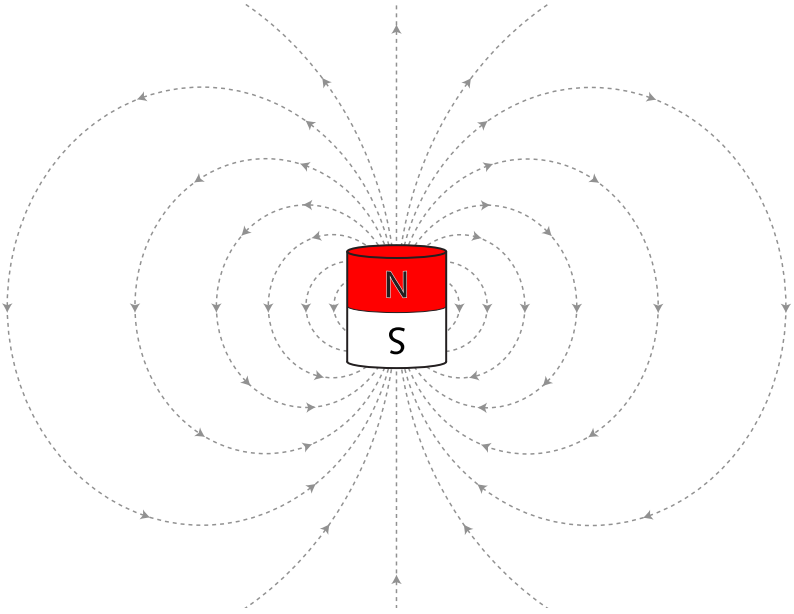

Figure 3.3. Nonuniform field of a permanent magnet. The curved dashed lines are magnetic field lines.

can result in magnetic forces acting on the magnet, which can cause it to translate linearly.

A diagram of a permanent magnet's nonuniform magnetic field is shown in Fig. 3.3. A permanent magnet has a north and south pole and can be referred to as a dipole. The dipole direction, also called the magnetization direction, points from the south pole to the north pole, and magnetic field lines flow from north to south, as shown in the figure. Closer field-line spacing denotes a stronger field intensity, while farther spacing indicates a weaker field. The dipole center is located at the center of the magnet. The cylinder magnet in the figure is magnetized axially: its dipole points along its cylindrical axis of symmetry.

The magnetic field strength of any source is homothetic, which means the field of a permanent magnet is unchanged as the magnet's dimensions are scaled. For example, if we measure the field 1 cm away from a 1 cm cubic magnet as 0.1 T, then the field measured 10 cm away from a 10 cm cubic magnet is also 0.1 T. This means that large magnets project their fields farther than small magnets. The field gradient, however, is not homothetic. The field of a small magnet changes faster

spatially than that of a large magnet. For example, if we measure a 10 T/m gradient 1 cm above a 1 cm cube magnet, we would only measure a 1 T/m gradient 10 cm above a 10 cm cube magnet [49]. Further discussion of these field properties and their importance as they relate to CI guidance is included later in this chapter.

As described in [50], the field generated by a permanent magnet can be described by the point-dipole model

$$\mathbf{B}(\mathbf{p}) = \frac{\mu_0}{4\pi \left|\mathbf{p}\right|^3} \left(\frac{3\left(\mathbf{\Gamma} \cdot \mathbf{p}\right)\mathbf{p}}{\left|\mathbf{p}\right|^2} - \mathbf{\Gamma} \right) \tag{3.2}$$

where μ_0 is the permeability of free space ($\mu_0 = 4\pi \times 10^{-7}$ T·m·A^{-1}), $\mathbf{p}$ is the location of a point in space with respect to the magnet dipole center (m), and $\mathbf{\Gamma}$ is the magnet dipole (A·m^2). A magnet's dipole strength is the product of its volume (m^3) and magnetization (A/m). In our application, a permanent magnet is used as the magnetic field source. The nonuniform field generated by this magnet can be approximated using this point-dipole model. Since the field is nonuniform, the effects of both magnetic torque and magnetic force must be considered when using permanent magnets for CI array steering.

3.2.2 Force and Torque

The governing equation describing the force acting on a magnet placed in a nonuniform magnetic field is

$$\mathbf{F} = v\left(\mathbf{m} \cdot \nabla\right)\mathbf{B} \tag{3.3}$$

where $\mathbf{F}$ is force (N), v (m^3) and $\mathbf{m}$ (A/m) are the magnet's volume and magnetization, $\mathbf{B}$ is the applied magnetic flux density (T), and ∇ is the gradient operator. The equation can be rewritten as

$$\mathbf{F} = v \begin{bmatrix} \frac{\partial}{\partial x}\mathbf{B}^{\mathrm{T}} \\ \frac{\partial}{\partial y}\mathbf{B}^{\mathrm{T}} \\ \frac{\partial}{\partial z}\mathbf{B}^{\mathrm{T}} \end{bmatrix} \mathbf{m}. \tag{3.4}$$

From Eq. (3.4) we see that the force in a given direction is the dot product of the derivative of the field in that direction and the magnetization of the permanent magnet placed in the field [51]. A force will only act on the magnet in a given

direction if a field gradient exists in that direction. If a field gradient does exist in a given direction, a force will only act on the magnet in that direction if some component of **m** lies in that direction.

The governing equation describing the torque acting on a magnet placed in a nonuniform magnetic field is

$$\mathbf{T} = v\mathbf{m} \times \mathbf{B} \tag{3.5}$$

where **T** is the torque (N·m) [51]. The applied torque is the cross product of the magnet's magnetization with the applied field. A torque will only act on the magnet if its dipole direction is not parallel to the direction of the applied field.

3.2.3 Axial Control

Fountain et al. [50] describe control of helical microrobots using a rotating-permanent-magnet (RPM) manipulator. Their RPM manipulator prototype consists of a permanent magnet housed in Delrin and mounted to a DC motor. The magnet is mounted such that its dipole direction is perpendicular to the motor rotation axis. One RPM manipulator control strategy described in [50] is axial control, where the helical microrobot is located along the rotation axis of the magnet. This region of the field can be called the axial control region. In our experimental setups and envisioned clinical implementation, the manipulator is positioned with its rotation axis aligned with the central spiral axis of the cochlea. In this arrangement, the magnet embedded in the implant tip is generally located along the manipulator rotation axis, so the principles involved in axial control can be used to steer the implant during insertion.

Fig. 3.4 can be used to describe axial control and the forces and torques involved. The large magnet is the manipulator magnet and the small magnet is the implant magnet. The global coordinate frame is located at the manipulator magnet dipole center but is shown offset in the figure to avoid graphical clutter. In practice the manipulator magnet would rotate in the xz-plane about the y-axis (the motor rotation axis), but here we will analyze the setup as if the manipulator magnet were fixed in the global frame. The implant magnet is positioned in the axial control

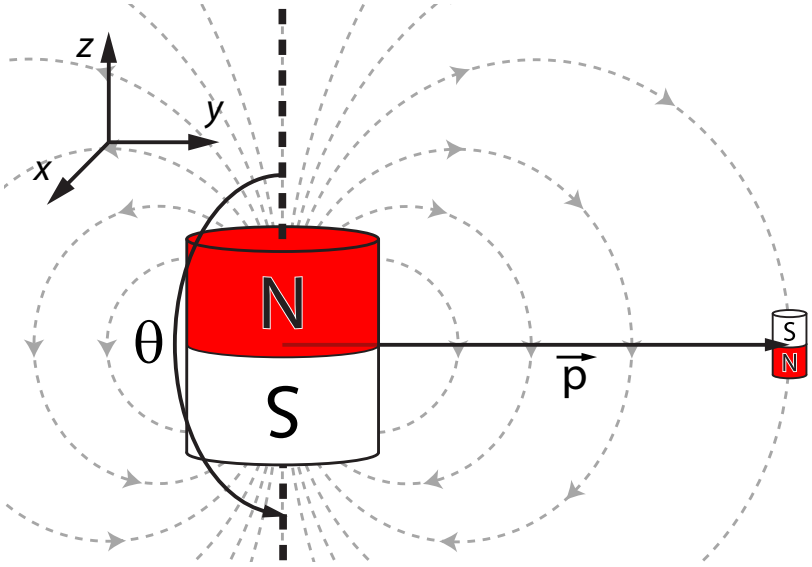

Figure 3.4. Axial control diagram. The large magnet is the manipulator magnet, fixed with the global coordinate frame origin at its dipole center. The implant tip magnet (small magnet) is placed along the manipulator's rotation axis.

region of the field (i.e., along the motor's rotation axis), and can be rotated about the global y-axis in the xz-plane to any rotation angle θ. The vector $\mathbf{p}$ points from the manipulator dipole center to the implant dipole center.

The equations described in the previous section for the applied magnetic field, force, and torque can be simplified for the axial control region. Since the vectors $\mathbf{\Gamma}$ and $\mathbf{p}$ are perpendicular, Eq. (3.2) can be simplified to give the field magnitude, and then differentiated to give the field gradient:

$$|\mathbf{B}| = \frac{\mu_0 |\mathbf{\Gamma}|}{4\pi |\mathbf{p}|^3} \quad , \quad \frac{d|\mathbf{B}|}{d|\mathbf{p}|} = -\frac{3\mu_0 |\mathbf{\Gamma}|}{4\pi |\mathbf{p}|^4}. \tag{3.6}$$

From these equations, we see that the field strength is inversely proportional to $|\mathbf{p}|^3$ and the field gradient is inversely proportional to $|\mathbf{p}|^4$: as the distance from the magnet increases, the field gradient decays more quickly than the field strength.

Taking the partial derivatives in Eq. (3.4) and solving for the axial control region, we can expressed the force as

$$\mathbf{F} = \frac{d|\mathbf{B}|}{d|\mathbf{p}|} \begin{bmatrix} 0 & 0 & 0 \\ 0 & 0 & -1 \\ 0 & -1 & 0 \end{bmatrix} \mathbf{M} \tag{3.7}$$

where $\frac{d|\mathbf{B}|}{d|\mathbf{p}|}$ is the same as in Eq. (3.6), and $\mathbf{M} = v\mathbf{m}$ in A·m^2. The first, second, and third rows of the 3×3 matrix in Eq. (3.7) correspond to the x-, y-, and z-direction field gradients, respectively, and show when forces will act on a magnet placed in the field. A nonzero value in a row indicates that a field gradient exists in that axis direction. We see that no gradient exists in the x-direction (first row) and gradients do exist in the y- and z-directions (second and third rows, respectively). Since there is no x-direction gradient, forces will not act on the magnet in the x-direction for any $\mathbf{M}$. The second row, with a nonzero value only in the third column, indicates that a force will only act in the y-direction if some component of $\mathbf{M}$ points in the z-direction. The third row, with a nonzero value only in the second column, indicates that a force will only act in the z-direction if some component of $\mathbf{M}$ points in the y-direction. Using this equation, we can calculate the forces acting on the implant magnet for any $\mathbf{M}$ and $\mathbf{p}$.

Since the implant is confined within the ST channel during insertion, implant tip rotations are generally confined close to the xz-plane in Fig. 3.4. Using this assumption, Eq. (3.5) can be simplified to yield the torque equation

$$\mathbf{T} = |\mathbf{M}|\,|\mathbf{B}|\sin(\theta). \tag{3.8}$$

where θ is measured from the z-axis and $\theta = 0$ occurs when the manipulator and implant magnet dipoles are pointing in the same direction. The sign of the resulting torque value indicates its direction. In a real insertion some tip rotation can occur out of the xz-plane. This rotation and the associated component of $\mathbf{M}$ pointing out of the plane will be small and are related to the sine of the rotation angle. If rotations do occur out of the xz-plane, the torque can be calculated using Eq. (3.5).

The above magnetic field, force, and torque equations can be used to calculate the forces and torques acting on a magnet in the axial control region of the manipulator magnet field. As an example, assume that the implant magnet is placed 30 mm away from the field source ($\mathbf{p} = \begin{bmatrix} 0 & 0.03 & 0 \end{bmatrix}^{\mathrm{T}}$). An axially magnetized manipulator magnet was described in [50] and was also used for CI insertion experiments for this thesis. The dipole strength $|\mathbf{\Gamma}|$ of the magnet was previously

found to be $10.2\,\mathrm{A{\cdot}m^2}$, which can be used in Eq. (3.6) to calculate $|\mathbf{B}| = 0.0378\,\mathrm{T}$ and $\frac{d|\mathbf{B}|}{d|\mathbf{p}|} = -3.78\,\mathrm{T/m}$. With these values, we compute the forces and torques for three implant magnet orientations using Fig. 3.5 for reference:

1. $\mathbf{M} = |\mathbf{M}| \begin{bmatrix} 0 & 0 & -1 \end{bmatrix}^{\mathrm{T}}$: The implant dipole is pointed in the negative z-direction ($\theta = \pi$), which is the same direction as the applied field at the magnet's location (Fig. 3.5(a)). Using Eq. (3.7), the force vector is calculated as $\mathbf{F} = \begin{bmatrix} 0 & -3.78\,|\mathbf{M}| & 0 \end{bmatrix}^{\mathrm{T}}\,\mathrm{N}$. A force exists only in the negative y-direction. Since the value is negative, the force is an attractive force, pulling the implant magnet toward the field source. Since $\sin(\pi) = 0$, the torque is $\mathrm{T} = 0\,\mathrm{N{\cdot}m}$: no torque acts on the magnet.

2. $\mathbf{M} = |\mathbf{M}| \begin{bmatrix} -1 & 0 & 0 \end{bmatrix}^{\mathrm{T}}$: The implant dipole is pointed in the negative x-direction ($\theta = 3\pi/2$, Fig. 3.5(b)). The force vector becomes $\mathbf{F} = \begin{bmatrix} 0 & 0 & 0 \end{bmatrix}^{\mathrm{T}}\,\mathrm{N}$. No force acts on the magnet in any direction. Since $\sin(3\pi/2) = -1$, the torque is $\mathbf{T} = -0.0378\,|\mathbf{M}|\,\mathrm{N{\cdot}m}$, which would cause the magnet to rotate in the xz-plane in the direction shown in Fig. 3.5(b).

3. $\mathbf{M} = |\mathbf{M}| \begin{bmatrix} 0 & -1 & 0 \end{bmatrix}^{\mathrm{T}}$: The implant magnet dipole is pointed in the negative y-direction (Fig. 3.5(c)). The force vector is $\mathbf{F} = \begin{bmatrix} 0 & 0 & -3.78\,|\mathbf{M}| \end{bmatrix}^{\mathrm{T}}\,\mathrm{N}$. A force exists only in the negative z-direction, which would push the magnet downward. In this case, the magnet rotation is not in the xz-plane, so Eq. (3.8) cannot be used to calculate the torque. Using Eq. (3.5) and $\mathbf{B} = \begin{bmatrix} 0 & 0 & -0.0378 \end{bmatrix}^{\mathrm{T}}\,\mathrm{T}$, the torque is $\mathbf{T} = \begin{bmatrix} 0.0378\,|\mathbf{M}| & 0 & 0 \end{bmatrix}^{\mathrm{T}}\,\mathrm{N{\cdot}m}$: a positive torque acts about the x-axis, which would cause the magnet to rotate in the yz-plane in the direction shown in Fig. 3.5(c).

If the magnet dipoles were pointing in the opposite direction in each of the above cases, the applied forces and torques would have the same magnitudes but opposite directions. Note that as the magnet is moved closer to or farther from the field source in the axial control region, only the field strength changes and the field direction does not. Thus, moving the manipulator toward or away from the ST will

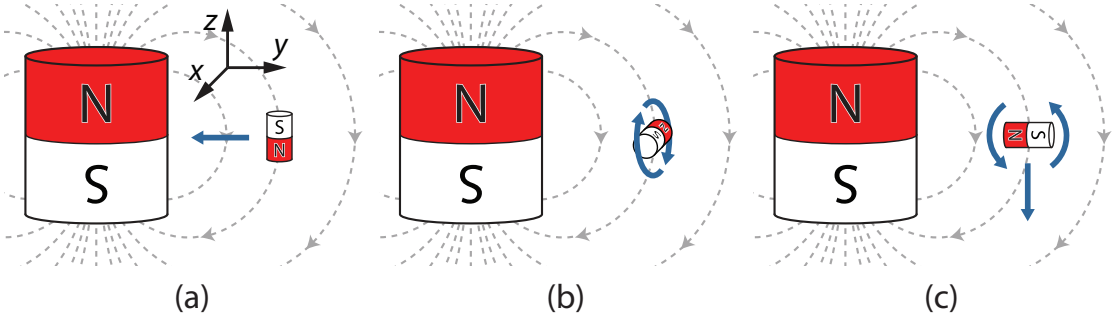

Figure 3.5. Implant tip magnet dipole pointed in three different directions with forces (straight arrows) and torques (curved arrows) shown. (a) Negative z-direction: force in negative y-direction. (b) Negative x-direction: negative torque about y-axis. (c) Negative y-direction: force in negative z-direction, positive torque about x-axis.

change the strength of the field applied at the location of the implant tip, but the field direction will not change unless the manipulator magnet is rotated.

Cases (a) and (b) in Fig. 3.5 are of most interest for magnetically guided CI insertion since implant tip rotations are generally confined to the xz-plane within the ST channel. These cases show when maximum and minimum forces and torques occur. Maximum force occurs when the dipoles of the manipulator and implant magnets are aligned: if their directions are opposite the force is attractive, and if their directions are the same the force is repulsive. Torque in this case is zero. Maximum torque occurs when the magnet dipole directions are perpendicular to one another, and force is zero in this case.

3.2.4 Scaling

Understanding how a magnetic field scales with magnet size is useful when designing systems for magnetically guided CI insertions. Field-gradient forces can cause the implant to press against cochlear walls, so these forces should likely be minimized to reduce friction and insertion trauma. However, since the human ST is a three-dimensional chamber, some field-gradient force may be beneficial in guiding the implant through the helical ST channel. An optimal setup would utilize a magnet that would provide a strong enough field without producing excessive field-gradient forces.

As previously discussed, the magnetic field of a source is homothetic but the field gradient is not. We can use Eq. (3.6) to analytically explore how field strength and gradient scale with magnet size. Consider a magnet and a field measured a distance p away from the magnet. Its field strength and gradient are calculated according to Eq. (3.6). If we scale the magnet's linear dimensions by a factor n then its volume scales as n^3. If the magnetization remains the same, its dipole strength Γ will also scale as n^3 since the dipole strength is the product of the magnet's magnetization and volume. If we measure the field the same distance p away from the center of this scaled magnet, we get

$$|\mathbf{B}| = \frac{n^3 \mu_0 |\mathbf{\Gamma}|}{4\pi |\mathbf{p}|^3} \quad , \quad \frac{d|\mathbf{B}|}{d|\mathbf{p}|} = -\frac{n^3 3\mu_0 |\mathbf{\Gamma}|}{4\pi |\mathbf{p}|^4}. \tag{3.9}$$

We see that both the field strength and gradient scale as n^3. Now suppose that we measure the field a distance $n \cdot p$ away from the scaled magnet so that the distance has been scaled by the same factor as the magnet's linear dimensions. Again, using Eq. (3.6) we get

$$|\mathbf{B}| = \frac{n^3 \mu_0 |\mathbf{\Gamma}|}{n^3 4\pi |\mathbf{p}|^3} \quad , \quad \frac{d|\mathbf{B}|}{d|\mathbf{p}|} = -\frac{n^3 3\mu_0 |\mathbf{\Gamma}|}{n^4 4\pi |\mathbf{p}|^4}. \tag{3.10}$$

Now we see that the measured field strength scales as $n^3/n^3 = 1$: the field strength measured a scaled distance $n \cdot p$ away from a magnet that has been scaled by the same factor n is the same as the field strength measured a distance p away from the original magnet. This is the homothetic property of the field. The field gradient, however, scales as $n^3/n^4 = 1/n$: the field gradient is $1/n$ times the originally measured gradient.

As an example, consider the axially magnetized manipulator magnet used in this thesis for CI insertion experiments. It is a 1-in-diameter, 1-in-long cylinder magnet with a dipole strength $|\mathbf{\Gamma}| = 10.2\,\mathrm{A{\cdot}m^2}$. Its magnetization can be found by dividing the dipole strength by the magnet's volume, yielding $\gamma = 7.93 \times 10^5\,\mathrm{A/m}$. For comparison we calculate the field strength and gradient 30 mm away from our 1 in magnet and 60 mm away from a magnet that is twice as large (2-in-diameter, 2-in-long cylinder) using Eq. (3.6). The scaling factor is $n = 2$ and the magnet's

linear dimensions and the distance at which we measure the field are both scaled by n. Both magnets have a magnetization $\gamma = 7.93 \times 10^5\,\mathrm{A/m}$. For the 1-in-diameter magnet we calculate $|\mathbf{B}| = 0.0378\,\mathrm{T}$ and $\frac{d|\mathbf{B}|}{d|\mathbf{p}|} = -3.78\,\mathrm{T/m}$. For the 2-in-diameter magnet we multiply the magnet's volume ($1.03{\times}10^{-}4\,\mathrm{m}^3$) by γ to get $|\mathbf{\Gamma}| = 81.6\,\mathrm{A{\cdot}m}^2$ and use this to calculate $|\mathbf{B}| = 0.0378\,\mathrm{T}$ and $\frac{d|\mathbf{B}|}{d|\mathbf{p}|} = -1.89\,\mathrm{T/m}$. The measured field strengths of the two magnets are equal, since we measured the field 30 mm away from the original magnet and twice as far away (60 mm) from the magnet that is twice as large ($n^3/n^3 = 1$). The gradient measured for the larger magnet is half as large as the gradient measured for the original magnet, which is expected ($n^3/n^4 = 1/n = 1/2$).

From these results we see how increasing manipulator magnet size and distance from the ST can be beneficial for CI guidance: we can decrease gradient forces without sacrificing field strength. A larger magnet can be used to produce the same field strength as a smaller magnet while producing a smaller gradient. Thus, we can achieve the same torque while decreasing magnetic field-gradient forces.

3.2.5 Beam Bending

Judy et al. [38] demonstrated how a torque exerted on a magnetically tipped beam will cause the beam to bend until an equilibrium position is reached. Equilibrium occurs when the torque acting on the magnet is equal in magnitude and opposite in direction to the mechanical restoring torque of the beam to which the magnet is attached. The experiments in [38] demonstrated this behavior, showing that, because of the stiffness of the beam, the beam tip was not necessarily pointed in the direction of the applied magnetic field. A magnetically tipped CI electrode array will behave similarly: in the presence of an applied field with the implant tip initially unaligned with the field, the implant will bend until an equilibrium position has been reached due to the implant stiffness. The implant generally consists of metal contacts and wires embedded in a silicone carrier, the combined properties of which determine its bending properties [11]. If the magnetic field is strong enough to overcome the implant mechanical restoring torque, the array will bend until its

tip is pointing in the same direction as the applied field. Array stiffness should be considered when using magnetic fields for CI insertion guidance.

3.3 Steering Methods

Two general steering methods were explored in the experiments in this thesis and will be referred to as the maximum-field method and the maximum-torque method (Fig. 3.6). The maximum-field method involves placing the manipulator magnet at a stationary location as close to the ST as possible so that the applied field is as large as possible. In this method, as the implant is inserted, the manipulator magnet is rotated to orient the implant tip away from the ST walls. If the applied field is strong enough to completely overcome the implant's mechanical restoring torque, then the implant tip and manipulator magnetization directions will be nearly parallel throughout the insertion. Note that in Fig. 3.6(a) the dipole of the manipulator magnet is aligned with the implant tip direction. If the field is not strong enough, then the manipulator rotation will have to be increased, applying more torque to compensate for the mechanical restoring torque of the implant. A possible disadvantage of this method is that attractive field-gradient forces are high, which could cause the implant tip to press against cochlear walls and structures, increase insertion friction, and cause cochlear damage.

The maximum-torque method utilizes the implant's mechanical restoring torque to help maintain perpendicularity between the manipulator and implant tip magnetization directions. In this method, the distance between the manipulator and ST can be varied, effectively changing the strength of the magnetic field applied around the implant tip. Since the magnet dipole directions are always perpendicular, the maximum amount of torque for any given manipulator-implant separation distance is applied to the CI tip. The increasing magnet size in the maximum-torque diagram in Fig. 3.6(b) indicates that the manipulator is advancing toward the ST as the implant is inserted, which is necessary to overcome the increasing implant mechanical restoring torque. As the implant is inserted into the ST, the manipulator is rotated and translated to maintain a 90° angle between the manipulator and

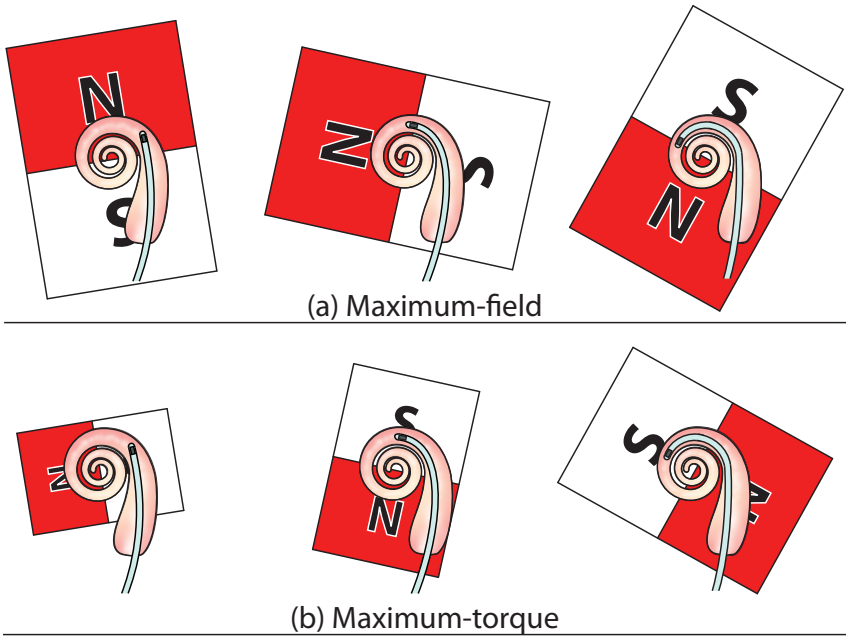

Figure 3.6. General steering methods explored in experiments in this thesis. (a) Maximum-field method. (b) Maximum-torque method. The increasing magnet size in the maximum-torque diagram indicates that the manipulator is advancing toward the ST.

implant tip directions. Forces due to the field-gradient are minimized, avoiding the possible friction increase that is a factor in the maximum-field method. The need to maintain a 90° angle between the manipulator and implant tip directions adds complexity to the insertion process, which could be considered a disadvantage of this method.

The benefit of guiding a CI using magnetic fields can be evaluated experimentally by comparing insertion forces for guided and non-guided insertions. An experimental CI insertion setup is shown in Fig. 3.7. A magnetically tipped free-fitting implant prototype is attached to a force/torque sensor. This assembly is mounted to two motorized linear stages, mounted vertically. A 3:1-scale ST phantom is mounted directly under the implant. An RPM manipulator is attached to a motorized linear stage with its rotation axis aligned with the central spiral axis of the ST channel. The stripe on the front of the manipulator marks the dipole direction of the enclosed 1-in-diameter, 1-in-long axially magnetized manipulator magnet. As

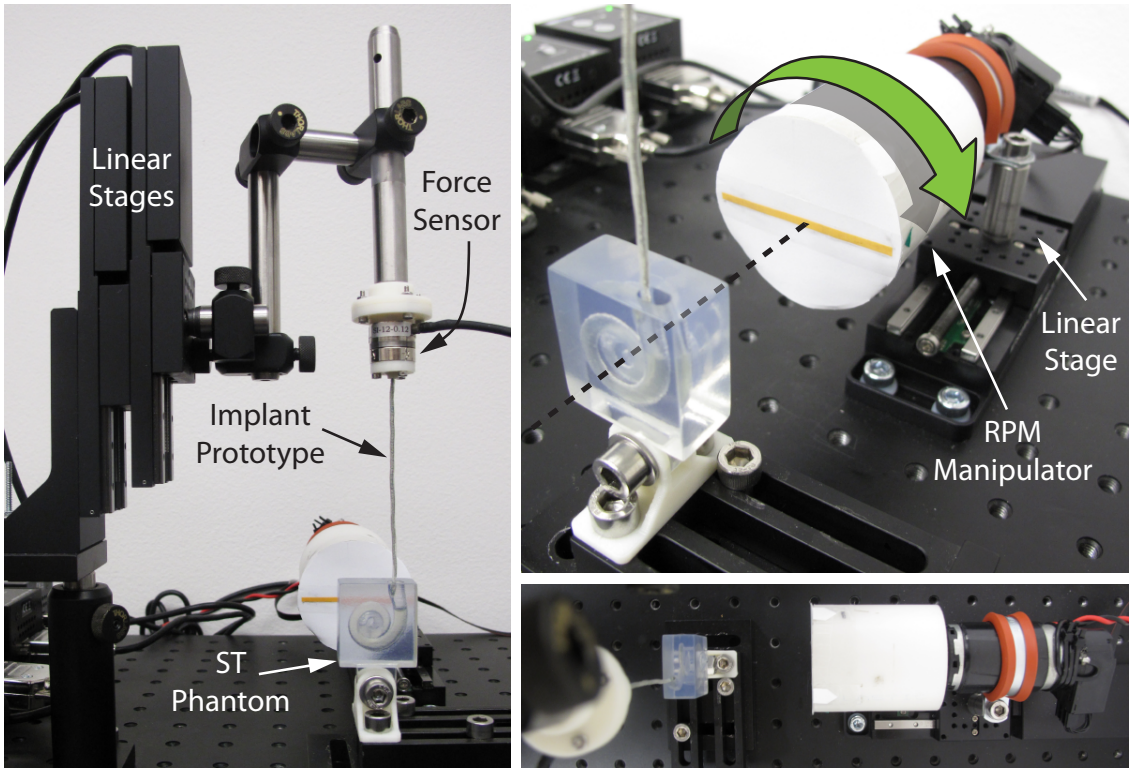

Figure 3.7. CI insertion experimental setup. (left) Front view. (top right) Oblique view. The dashed line shows that the manipulator rotation axis and cochlear central spiral axis are aligned. The curved arrow above the manipulator shows the manipulator rotation direction. (bottom right) Top view.

the implant is advanced into the ST, the manipulator can be translated and rotated to bend the implant away from the phantom channel walls. The setup shown in Fig. 3.7 was used to perform several insertion experiments using magnetically tipped prototype implants. Experimental setup details and results for guided and nonguided insertions are included in Chapter 6.

CHAPTER 4

IMPLANT PROTOTYPES

To validate magnetic steering as a useful strategy for CI surgery, we needed to create magnetically tipped CI prototypes. Commercial electrode arrays consist of electrodes spaced along a silicone carrier. Our goal was to embed a small permanent magnet in silicone rubber and create an implant that had bending properties that qualitatively mimicked those of a straight, free-fitting implant like the MED-EL practice electrode shown in Fig. 4.1. Our scaled-up magnetically tipped implant prototype is also shown in the figure and is described in detail in this chapter. Scaled-up prototypes are easier to make, especially since the smallest commercially available permanent magnet we found has a diameter of 0.75 mm.

MED-EL practice electrode

Magnetically tipped implant prototype

Figure 4.1. The MED-EL practice electrode shown is a straight, free-fitting array with a length of about 32 mm, and it tapers from a base diameter of 1.3 mm to a tip diameter of 0.5 mm. Our scaled-up prototype has a length of about 83 mm and a constant diameter of 1.6 mm.

We constructed an acrylic mold for CI prototype casting. Several views of the completed mold are shown in Fig. 4.2. The mold consists of a 1/4 in thick sheet of acrylic, which we machined into two $6\times6\,\text{in}^2$ squares. These squares were clamped together and a section was cut off, yielding an upper section about 1 9/16 in tall, and a lower section about 4 3/8 in tall. Access holes were drilled through the tip of the mold near the corner, and the portion of the holes extending into the lower section of the mold were tapped. The two sections are fastened together using two 3/4 in long 4-40 screws, which are inserted into the access holes. The assembled mold is about 5 15/16 in tall, 6 in wide, and 1/2 in thick. The mold halves (each 1/4 in thick) for each section are fastened together using four 3/4 in long 4-40 screws and nuts. With the mold assembled, channels were drilled from the top of the mold at the interface of the mold halves, creating cavities used to form electrode array prototypes. If the mold only had one section, the cavity length would be limited to the length of the drill bit used to drill the cavity. With two sections, we can drill through the upper section, remove it, and drill into the lower section using the same drill bit, thereby creating a channel longer than the length of the bit. This was necessary to be able to eventually create a scaled-up implant prototype.

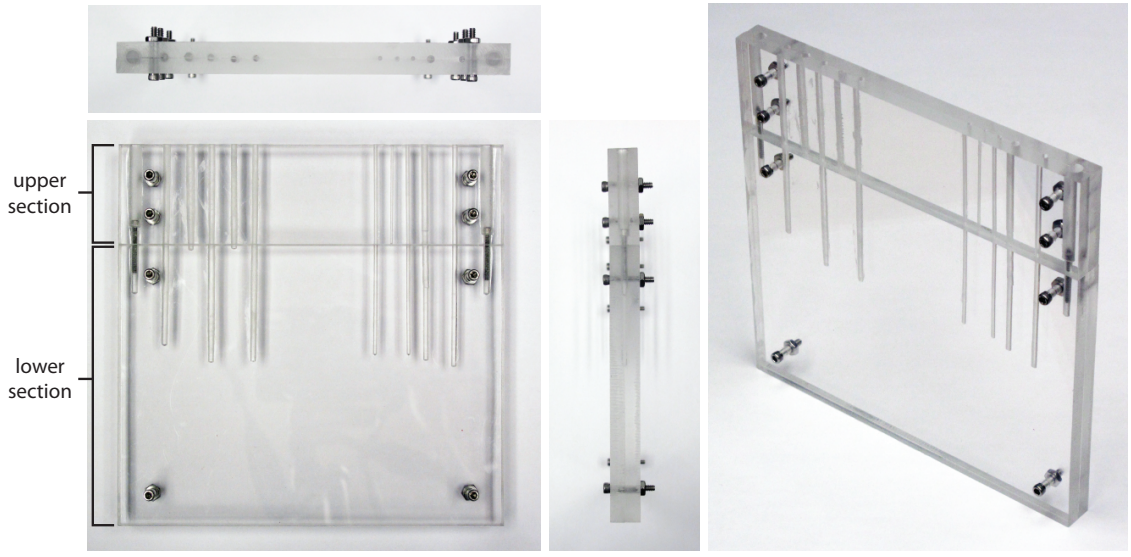

Figure 4.2. Several views of the acrylic mold used to fabricate magnetically tipped CI prototypes.

The first array prototypes were made by assembling the acrylic mold, dropping a magnet into a drilled channel, and injecting liquid silicone rubber into the mold using a syringe until the cavity was completely filled. After the silicone had cured, the mold was taken apart and the prototype was removed. During removal, excess silicone flash was cut away using a sharp knife. These prototypes were easily bent by applying a torque to the embedded magnet using another larger magnet, but we observed that they were too floppy and lacked the qualitative stiffness of commercial arrays. This is a logical result, since real cochlear implant electrode arrays are not only made of silicone; commercial arrays have wires running along the length of the array from its base to the stimulating electrodes. From this observation, we decided to embed wires in the prototypes to increase their stiffness.

Microscale aluminum bonding wire (25 μm-diameter) was obtained from the University of Utah Microfab laboratory and was used to make near-scale array prototypes using the smallest mold cavity, which has a diameter of about 1 mm and a length of about 39 mm. A prototype was made with one straight embedded wire to explore the effect of adding only one wire. After the prototype was removed from the mold, we discovered that embedding a straight wire made the implant sensitive to shape deformation; as the implant was stretched, the position of the wire shifted within the silicone. When the stress was released, the implant assumed a curved shape. Although this was an undesirable result, such a technique could be used to create precurled arrays in future work. Close inspection of a real electrode array revealed that the lead wires have a wavy appearance along the array length, as shown in Fig. 4.3. We concluded that introducing similar bends into the prototype wires could make the implant resilient to shape deformation, since bends in the embedded wires would allow them to extend with the silicone stretching and prevent undesired deformation. Wire also gives commercial arrays some ability to deform plastically, and adding wire to our prototype would provide a similar property.

We created wavy wires by wrapping bundles of microwires in a tight coil around a 0.018 in diameter steel luer lock needle. Removing the wires from the needle and partially extending the coil created the desired wavy effect, which is shown in Fig.

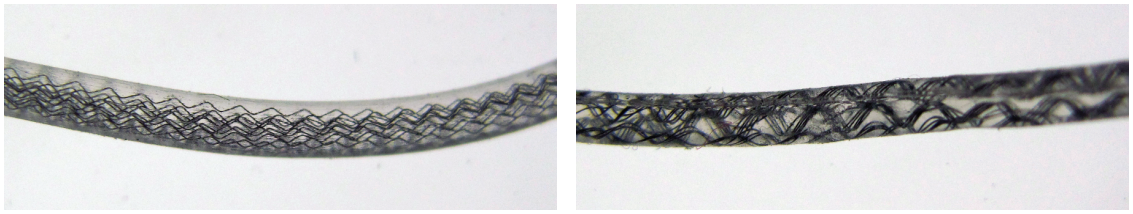

Figure 4.3. Images showing the wavy appearance of microwires in a commercial array and one of our prototype arrays.

4.3. With the acrylic mold disassembled, the wires were placed in one half of a channel and one or two magnets were placed at the channel tip. The other half of the mold was set in place and the mold was fastened together. Silicone rubber was injected into the channel using a syringe. Several prototypes were made using wavy wires. The number of wires used in the prototypes was increased until the implant stiffness seemed to approximate that of a real electrode array.

The best array produced using this method had 30 wires of three different lengths, with the wires extending from the base of the implant toward the tip. This was done to create a tapered stiffness effect that exists in real implants, which are stiffer at the base and become more flexible toward the tip. Part of this tapered stiffness is due to the physical dimensions of the array; it is thicker at its base and thinner at its tip. More wires at the base of the implant also make it stiffer in that region, and the number of wires running along the carrier to the electrodes decreases toward the implant tip, which also makes the implant more flexible in that region. Since our prototypes have a constant diameter, we use different amounts of wire to mimic the graded stiffness property.

The prototype had two 0.78 mm cube magnets embedded in its tip. This prototype was used to perform some preliminary experiments, but was still not stiff enough and would buckle during insertion. During prototype production, as the number of wires was increased, it became increasingly difficult to position the wires correctly inside the mold. We also found that injecting silicone into the channel from the top of the mold with the mold assembled became increasingly

difficult since the microwires took up much of the channel volume. Increasing the number of wires to more than 30 did not seem to be a practical option to create an implant with greater stiffness.

To increase implant stiffness we tried a different wire strategy. A single thicker wire (0.11 mm-diameter) was wrapped in a tight coil around the luer lock needle until the coil was the correct length for the implant channel. A prototype was made using this single-wire coil, but it was not stiff enough. To increase stiffness, four wires were bundled together for the beginning of the coil. To mimic the tapered stiffness of a real electrode array, the number of wires was reduced as the length of the coil increased. Starting with four wires in the coil, the wires were wound around the needle until a desired coil length was reached. One wire was cut and the remaining three wires were coiled until a desired length was reached. Another wire was cut and the two remaining wires were coiled for several wraps. One wire was again cut, and the remaining one wire strand was coiled around the needle until the desired total coil length was reached. This resulted in an implant that was stiffer at the base (where more wires were coiled together) and more flexible toward the tip, creating a tapered stiffness effect. We had observed in previous prototypes that the embedded magnet would sometimes tear through the silicone as torque was exerted on it. To avoid this, the tip of the wire coil was wrapped a few turns around the embedded magnets. This reinforced the implant tip, and also likely assisted to transmit bending through the length of the implant rather than mostly bending only the silicone rubber at the implant tip. This stiffer implant was used for some preliminary insertion experiments but there was not enough silicone rubber around the magnets embedded in the implant tip, which eventually weakened and tore; with the wire wrapped around the 0.78 mm cube magnets, the diameter of the wire and magnet core appeared to be about 1 mm, which was the diameter of the channel in the acrylic mold used to form the implant.

A scaled-up implant prototype was made using a similar wire coiling technique. It was made to be used with the 3:1 ST phantom described in Chapter 5, and was used to perform the insertion experiments described in Chapter 6. Because

of its larger dimensions, this prototype was easier to make and the silicone more completely covered the wire core and embedded magnet. Several key steps in the process are shown in Fig. 4.4 and are referenced by letter in our process description: (a) The ends of 8 wires were twisted together and wrapped around the luer lock needle. (b) When the desired coil length was reached, one wire was cut. The remaining wires were twisted together and wrapping was continued. The procedure was repeated until only one wire remained to be coiled around the needle, which was wrapped to a desired length. (c) A piece of small plastic tubing had been slid onto the needle, and its outside diameter when on the needle was 0.72 mm. The wire was wrapped around this tubing to create a coil with a larger diameter into which the tip magnet would be placed. The wire should be wrapped loosely to facilitate placement of the magnet inside the coil tip. (d) The end of the wire was trimmed as needed and the coil was removed from the needle. (e) A 1 mm-diameter × 2 mm-long grade N50 cylinder magnet was placed in the end of the coil, and the coil and magnet were encased in silicone using our acrylic mold. We found that the molding process was easiest if the mold was disassembled and one half of the channel was filled with liquid silicone. The wire core with attached magnet were placed in the silicone-filled half channel. The channel on the corresponding mold half was then filled with silicone, and the two halves were fastened together.

The implant has a diameter of 1.6 mm and is close to 83 mm long. Preliminary testing showed that the implant base was not stiff enough. A piece of 0.007 in diameter shape-memory-alloy wire was inserted into the base of the prototype

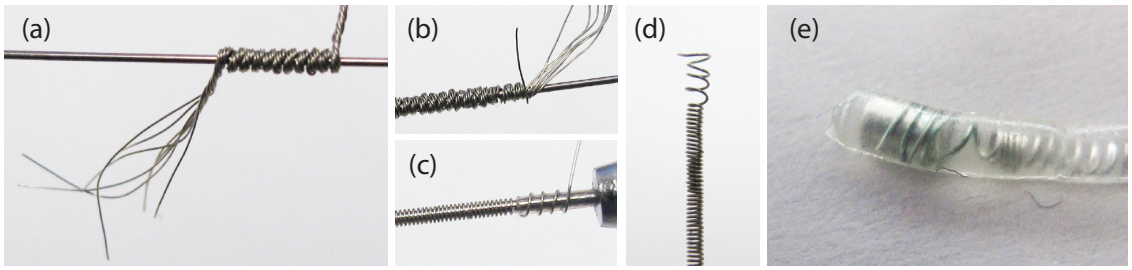

Figure 4.4. Key steps for production of the wire core used in a scaled-up implant prototype. A description of each image is given in the chapter text.

through the center of the wire core to a depth of roughly 25 mm. This provided the stiffness to prevent most implant buckling.

A described earlier, the MED-EL electrode diameter tapers from base to tip. This shape contributes to its increased stiffness at its base and flexibility at the tip. Since our prototypes are not tapered, we use varying amounts of wire to achieve a graded stiffness effect. Our prototype is not meant to be a scaled version of the MED-EL array, but was made to mimic some important properties of a real array, including graded stiffness and the use of silicone rubber. The use of a wire core also resulted in some plastic deformability, which we observed in the MED-EL practice electrode. Possible improvements to the array design are discussed in Chapter 7. Our main goal was to create a prototype that could be used to validate our magnetic steering concept. An image of the implant being bent by a magnetic field during an insertion experiment is shown in Fig. 4.5. The graded stiffness of the implant causes it to bend most at the tip and progressively less toward the implant base. Insertion experiments performed using this implant are described in Chapter 6.

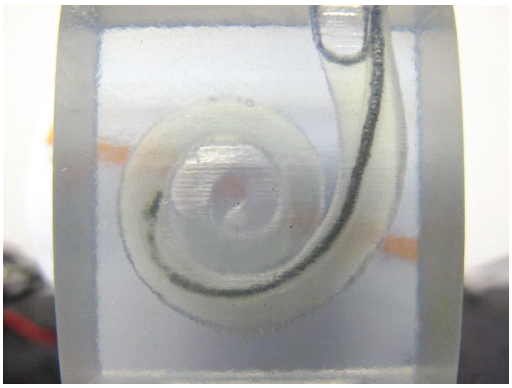

Figure 4.5. Example of implant bending using magnetic fields. The implant pictured is the scaled-up implant described in this chapter.

CHAPTER 5

A SCALABLE MODEL FOR SCALA TYMPANI PHANTOMS

In CI insertion experiments, ST phantoms are often used in place of cadaver cochleae. Synthetic phantoms have been developed or used by several research groups. Rebscher et al. [52] developed a transparent human ST phantom by making casts of human cadaver cochleae. The group created both epoxy and silicone elastomer phantoms, and a silicone phantom was used in insertion studies described in [3, 7]. Included in [7] is a description of how the casts were measured to create a 3D digital model of the ST channel for use in evaluating electrode array designs. Zhang et al. created custom scaled-up prototype electrode arrays. They designed and used scaled 2D and 3D ST phantoms for insertion experiments using the custom arrays [8, 9]. Two-dimensional phantoms from Cochlear were used in [1, 10] for insertion studies. A 3D ST phantom from MED-EL was used in [6, 12, 34, 36].

Each of the above phantoms can be useful for *in-vitro* experimentation, but each has its limitations. Two-dimensional phantoms lack the true three-dimensional form of the human cochlea and do not offer a true representation of the ST's spiral form. The phantoms described in [52], cast from cadaver cochleae, offer accurate dimensions but are not reproducible without a physical mold. The group created a digital model of the ST channel, but we find no indication in the literature that this has been used or is available to create a phantom. The 3D phantom from MED-EL has a spiral shape, but from images of the phantom it appears that it does not faithfully represent ST dimensions along the channel length (e.g., the channel tapers too quickly) and it does not permit insertions past $1\frac{1}{4}$ turns. The method of ST modeling described in this chapter is patterned after that employed

by Zhang et al., but it is unclear from the literature whether their model took into account some shape and sizing aspects discussed herein. A 1:1 scale 3D phantom has been produced by Advanced Bionics that allows insertion up to 2 turns into the channel, but creating a 1:1 scale CI prototype is sometimes difficult during the development of novel technology such as steerable CIs. We also do not know how accurate the model is or the exact method by which it was dimensioned and designed. The model described in this chapter, and the phantoms produced from the model, address the limitations of current ST models and provide the following benefits:

- Reproducibility: the modeling method described in this chapter can be reproduced using common engineering software and commonly available fabrication resources.
- Accuracy: the model represents a mean ST with size and shape informed by published anatomical data.
- Scalability: the model can be easily scaled to accommodate research needs.

5.1 Prior ST Models

Cohen et al. [53] describe a method of fitting a template spiral to the shape of the images of implanted free-fitting CI electrode arrays. Radiographic images were selected from 30 CI patients, as well as images from nine cadaver temporal bones. For each radiograph, the positions of several points along each implanted array were digitized, and software was used to fit a mathematical spiral curve to the data for each array. The group found that the spiral shape of an implanted array could be modeled by the expressions

$$\theta < 100^\circ : \quad R = C\left(1 - D\ln(\theta - \theta_0)\right) \tag{5.1}$$

$$\theta \geq 100^\circ : \quad R = Ae^{-B\theta} \tag{5.2}$$

where R is the distance from the spiral center, θ is the angle in degrees, and A, B, C, D, and θ_0 are constants.

Yoo et al. [54] created a 3D model of the cochlea for viewing on the internet. Their model was based on the work done in [53], using Eqs. (5.1) and (5.2) and a height equation

$$z = E(\theta - \theta_1) \tag{5.3}$$

where z is the height value of each discrete spiral point, E is a constant, and θ_1 is the starting angular degree. The group used the resulting 3D spiral as the central path of their cochlea model with cross-section data from [55] to create a generalized 3D cochlea model (i.e., individual channels are not differentiated).

Zhang et al. [9] used the work of [53] and [54] to create 2D and 3D ST phantoms and used ST dimensions given by Wysocki [56] to define elliptical channel cross sections along the length of the 3D spiral curve. However, the authors did not publish the specifics of their model.

5.2 The ST Model

Using a method similar to the work of Zhang et al., we design an ST model based on [53, 54, 56] and include some modifications to increase the model's dimensional accuracy and qualitative appearance, as will be discussed hereafter.

Equations (5.1)–(5.3) are implemented in Matlab to generate a 3D spiral path. The values for A, B, D, and θ_0 are given in [53], and the value for C is determined by setting Eqs. (5.1) and (5.2) equal to each other with $\theta = 100°$ and solving for C as described in [53]. The values for θ_1 and the final spiral angle, θ_f, are given in [54]. The value for the constant E is determined by solving Eq. (5.3) using the mean value of cochlear axial height, $z = 2.75\,\text{mm}$, and $\theta = \theta_f$ as described in [54]. The values for the constants listed above are given in Table 5.1. The constants given in Table 5.1 with Eqs. (5.1)–(5.3) can be used to create a 1:1 scale 3D spiral path. A scaling factor s can be used to scale the ST model (e.g., $s = 3$ would

Table 5.1. ST Spiral Constants.

A (mm)	B (mm)	C (mm)	D (mm)	E (mm)	θ_0 (deg)	θ_1 (deg)	θ_f (deg)
3.762	0.001317	7.967	0.1287	0.003056	5.0	10.3	910.3

create a 3:1 scale model). The values of R for discrete points along the curve are calculated using Eqs. (5.1)–(5.3), where θ varies from $\theta_1 = 10.3°$ to $\theta_f = 910.3°$ in $0.1°$ increments. For each value of θ, the (x, y, z) coordinates of the corresponding 3D point on the curve are calculated using the equations

$$x = sR\cos(\theta) \tag{5.4}$$

$$y = sR\sin(\theta) \tag{5.5}$$

$$z = sE(\theta - \theta_1) \tag{5.6}$$

Several views of the 3D spiral path are shown in Fig. 5.1.

ST channel width and height dimensions for this model are based on the work of Wysocki et al. [56], who created latex casts of the human cochlea from 25 cadaver temporal bones and measured the width and height of the ST at 1 mm intervals along its length from the beginning of the ST. All but one of the values used

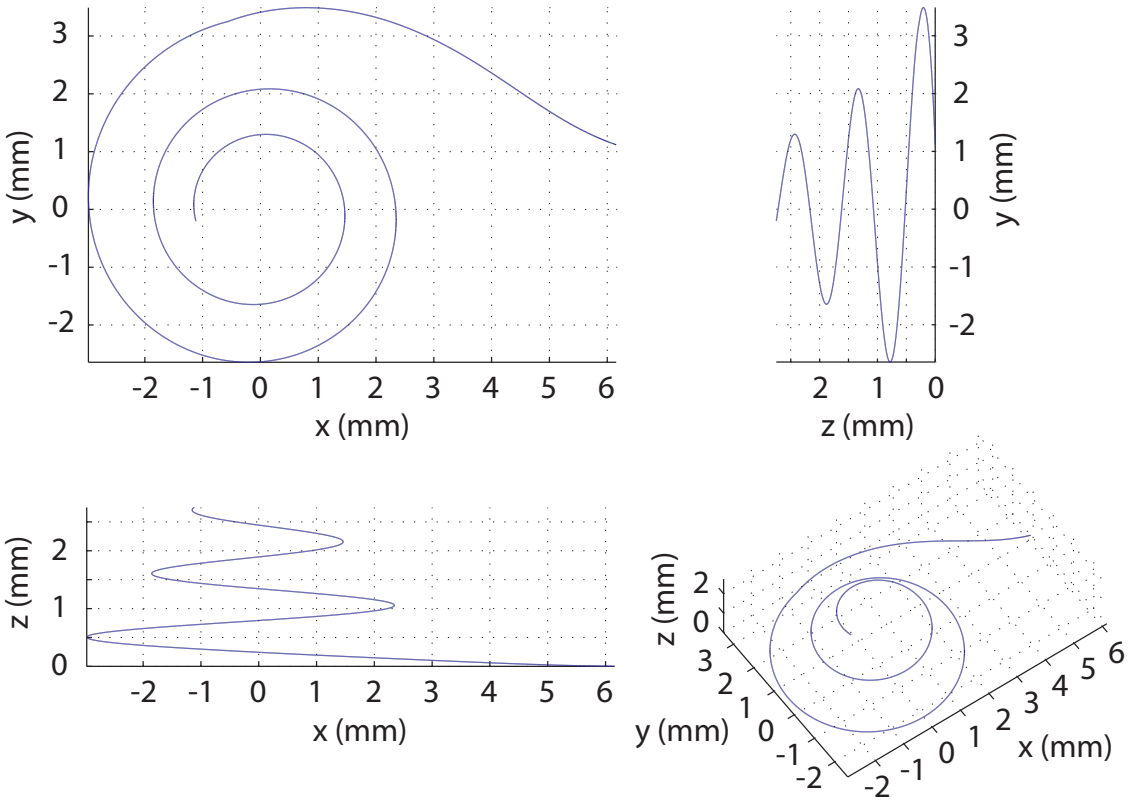

Figure 5.1. 1:1 scale 3D ST spiral path, generated in Matlab.

in the model are channel dimensions given in plots in [56]. Due to construction difficulties in SolidWorks (i.e., failure when trying to create a lofted cut between the profiles) when using the given final channel width of about 1.45 mm, the value for the previous channel width (1.25 mm) is used as the final channel width. The channel dimensions are given in Table 5.2. ST dimensions given in [56] for 0 mm and 1 mm along the ST length are neglected in this model since the given ST height and width values for 0 mm are reported as zero, and there is a large jump in both width and height values between 0 mm and 2 mm along the ST length. Values in Table 5.2 from 0 mm to 34 mm along the spiral curve correspond to values from 2 mm to 36 mm measured along the ST length given in [56]. Note that the values do not change monotonically. The height, width, and position values are multiplied by the scaling factor s so that scaling is correctly applied to dimension the ST channel profiles to place them at regular intervals along the spiral curve.

Zhang et al. [9] modeled the ST channel cross sections as ellipses. However, we

Table 5.2. ST Channel Dimensions, based on [56]. Position (Pos) is measured along the spiral from the basal end ($\theta = 10.3°$), h = profile height, w = profile width, ϕ = profile tilt angle relative to the xy-plane.

Pos (mm)	**0**	**1**	**2**	**3**	**4**	**5**	**6**	**7**
h (mm)	1.30	1.18	1.14	1.13	1.08	1.03	0.98	0.94
w (mm)	2.10	2.10	1.95	1.85	1.80	1.74	1.70	1.68
ϕ (rad)	0	0.01	0.02	0.03	0.04	0.05	0.06	0.07
Pos (mm)	**8**	**9**	**10**	**11**	**12**	**13**	**14**	**15**
h (mm)	0.90	0.86	0.84	0.83	0.82	0.82	0.81	0.81
w (mm)	1.63	1.60	1.59	1.51	1.50	1.54	1.46	1.45
ϕ (rad)	0.08	0.09	0.10	0.11	0.12	0.13	0.14	0.15
Pos (mm)	**16**	**17**	**18**	**19**	**20**	**21**	**22**	**23**
h (mm)	0.79	0.77	0.75	0.73	0.72	0.67	0.66	0.63
w (mm)	1.43	1.38	1.33	1.32	1.31	1.30	1.30	1.30
ϕ (rad)	0.16	0.17	0.18	0.19	0.20	0.21	0.22	0.23
Pos (mm)	**24**	**25**	**26**	**27**	**28**	**29**	**30**	**31**
h (mm)	0.59	0.54	0.47	0.43	0.37	0.34	0.29	0.28
w (mm)	1.30	1.30	1.30	1.30	1.31	1.31	1.26	1.15
ϕ (rad)	0.24	0.25	0.26	0.27	0.28	0.29	0.30	0.25
Pos (mm)	**32**	**33**	**34**					
h (mm)	0.26	0.35	0.30					
w (mm)	1.23	1.25	1.25					
ϕ (rad)	0.20	0.15	0.10					

model the ST cross sections as semicircular ends connected by straight segments, which we believe more closely match the general ST channel cross-section outline, as shown in Fig. 5.2. A profile tilt angle ϕ between the xy-plane and the major axis of the cross section is set for each profile to qualitatively approximate the angle observed in many cochlea cross-sectional views, in which the profile cross-section width directions are not perpendicular to the cochlea central spiral axis, as shown in Fig. 5.2. A profile example is shown in Fig. 5.3, with the angle ϕ defined relative to the xy-plane. The ϕ values used in this model are included in Table 5.2.

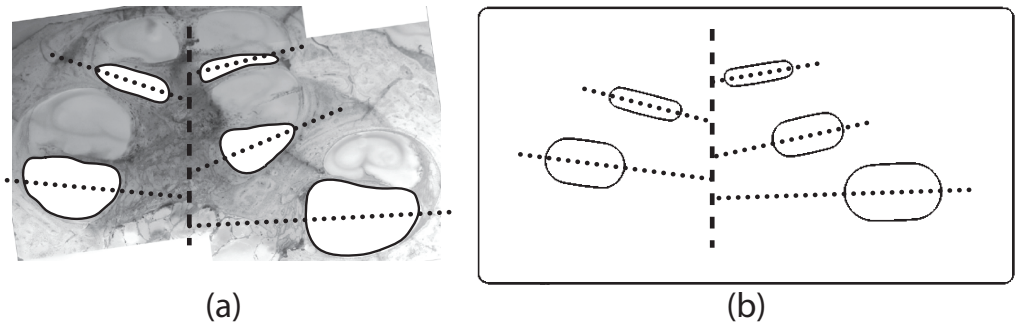

Figure 5.2. Cross sections showing ST channel profile outlines and tilt angles (dotted lines). The dashed vertical lines represent the cochlear central spiral axis. (a) Photograph of cochlea cross section (public domain image from [3]), with ST profiles outlined. (b) Model cross section.

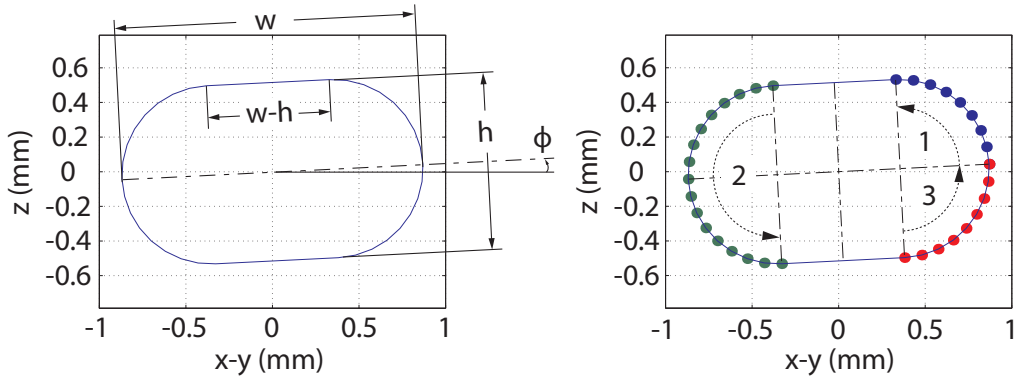

Figure 5.3. ST channel profile example. (left) Profile showing width (w), height (h) and angle (ϕ) of the profile relative to the xy-plane. (right) Order in which profile points are plotted: 1 (Eq. 5.8), 2 (Eq. 5.9), 3 (Eq. 5.10).

Our first goal is to place the cross sections along the length of the spiral curve, while temporarily neglecting their radial positioning. Ultimately, we are only concerned with the final placement of the cross sections and not with the spiral path itself. The discrete point along the curve which is used as the coordinate center of each cross-section profile is found based on the summed length of the path segments from the beginning of the curve to each point. The angle α of each profile relative to the model coordinate frame x-axis is also determined (Fig. 5.4). This is done by finding the direction of the xy-plane projection of the spiral curve that passes through each profile and rotating the direction by $\pi/2$ rad clockwise using the equation

$$\alpha = \text{atan2}\left(\Delta y, \Delta x\right) - \pi/2 \tag{5.7}$$

where α is the angle of the profile projection onto the xy-plane with respect to the x-axis, atan2 is the four-quadrant inverse tangent function, and Δy and Δx are the differences between the y and x coordinates of the center of the profile and the successive discrete point on the spiral curve. This effectively places each profile perpendicular to the xy-plane projection of the spiral curve passing through it.

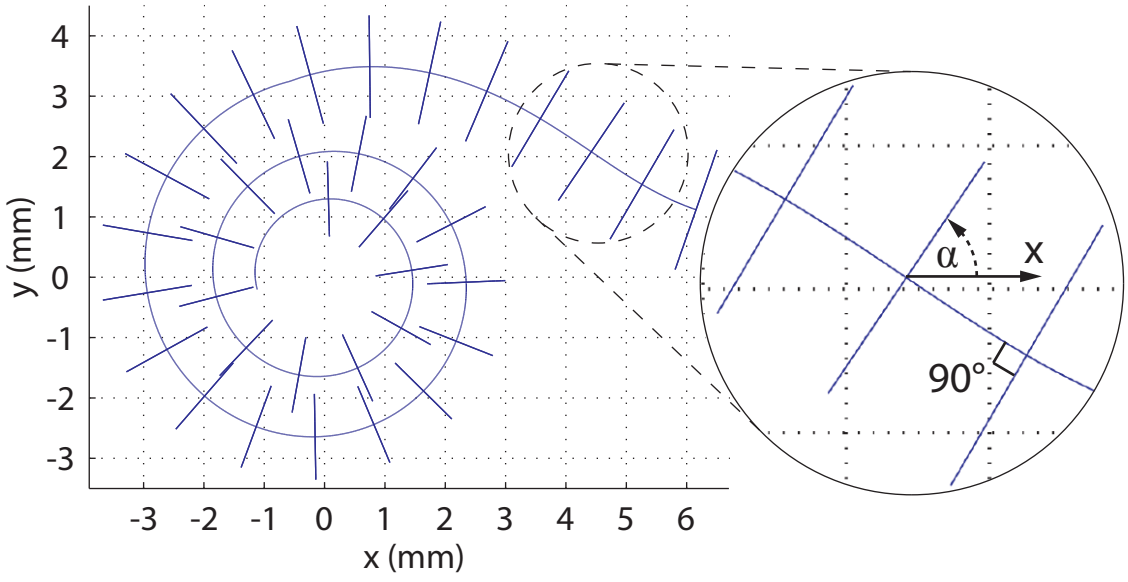

Figure 5.4. ST spiral curve with profiles positioned along its length. The channel profile angle α is shown, defined relative to the positive x-axis direction.

To create the oblong channel profiles, points defining each profile, with profile center (0,0), are calculated using the following equations inspired by ellipse equations:

$$\text{for } 0 \leq \theta \leq \pi/2: \tag{5.8}$$
$$x = \frac{w-h}{2}\cos(\phi) + \frac{h}{2}\cos(\theta+\phi)$$
$$z = \frac{w-h}{2}\sin(\phi) + \frac{h}{2}\sin(\theta+\phi)$$

$$\text{for } \pi/2 \leq \theta \leq 3\pi/2: \tag{5.9}$$
$$x = \frac{w-h}{2}\cos(\pi+\phi) + \frac{h}{2}\cos(\theta+\phi)$$
$$z = \frac{w-h}{2}\sin(\pi+\phi) + \frac{h}{2}\sin(\theta+\phi)$$

$$\text{for } 3\pi/2 \leq \theta \leq 2\pi: \tag{5.10}$$
$$x = \frac{w-h}{2}\cos(\phi) + \frac{h}{2}\cos(\theta+\phi)$$
$$z = \frac{w-h}{2}\sin(\phi) + \frac{h}{2}\sin(\theta+\phi)$$

where w and h are the width and height of a given profile, θ varies from 0 to 2π radians in increments of $\pi/16$ radians in the sets shown in Fig. 5.3, and ϕ is the tilt angle (radians) of a given profile. Note that two points are calculated at three angles: $\theta = 0, 2\pi$, $\theta = \pi/2$, and $\theta = 3\pi/2$. A solid profile outline is formed (Fig. 5.3) when the profile points are plotted in the order shown. Next, the individual 2D profiles of Fig. 5.3 are converted to the true 3D profiles as shown in Fig. 5.4. Arrays containing the (x_{pc},y_{pc},z_{pc}) coordinates, defining each profile in its correct 3D position and orientation, are then formed using the equations

$$x_{pc} = X_c + x\cos(\alpha) \tag{5.11}$$
$$y_{pc} = Y_c + x\sin(\alpha) \tag{5.12}$$
$$z_{pc} = Z_c + z \tag{5.13}$$

where x_{pc}, y_{pc}, and z_{pc} contain the coordinates of each calculated profile point with the profile positioned so that the ST spiral curve passes through its center; X_c, Y_c, and Z_c are the coordinates of the center of the profile; x and z contain the profile points calculated using Eqs. (5.8)–(5.10); and α is the orientation angle of the profile (see Eq. (5.7) and Fig. 5.4).

Fig. 5.4 shows the ST cross-section profiles placed along the spiral curve, with the curve passing through the profile centers. It can be seen in the figure that the final profile is not as close to the apex of the spiral path as it should be. We want to keep the profiles spaced at 1 mm increments along the curve as we shift them closer to the curve apex, which can be achieved by tightening the spiral. Recall that the spiral path from [53] was not intended to be used to describe the center of the ST channel, so some necessary tightening is expected. To tighten the spiral, the implementation of Eq. (5.2) is modified to incrementally enhance the decrease in R as θ increases by changing the value used for θ. The modification can be modeled by the empirical expression

$$\theta_{mod} = 0.0002\theta^2 + 0.98\theta \tag{5.14}$$

The calculation of R in Eqs. (5.1) and (5.2) should use this θ_{mod}. The tightened curve with positioned cross-section profiles is shown in Fig. 5.5.

With the profiles centered along the spiral path, the inner and outer walls of the channel formed by the ST cross sections measure 24.92 mm and 43.13 mm, respectively. These values exceed those of [57], which reports inner and outer ST wall lengths of 18.29 mm±1.47 mm and 40.81 mm±1.97 mm, respectively. This is again a logical and expected result, since Eqs. (5.1) and (5.2) give a mean template spiral for electrode arrays positioned close to the ST outer wall, not along the ST center. Accordingly, we shift the cross-section profiles inward, positioning the template spiral closer to the ST outer wall, and decreasing the ST inner- and outer-wall lengths. Each profile is shifted by a fraction of its width along the directions corresponding to the dotted lines in Fig. 5.2(b). Shifting the profiles by 1/4 of their respective widths achieves the desired result. The shifted coordinates

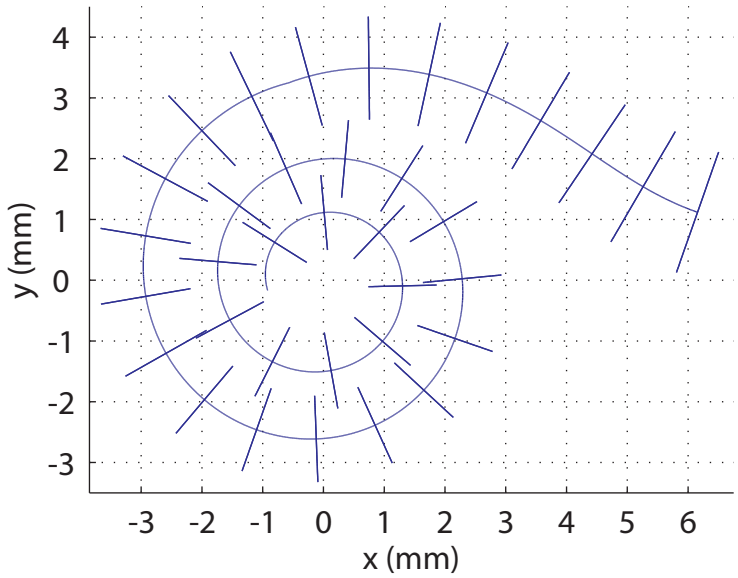

Figure 5.5. ST spiral curve with profiles centered, after spiral tightening to position the final profile closer to the curve apex.

for each profile are calculated using the equations

$$x_{ps} = x_{pc} - \frac{w}{4}\cos(\alpha)\cos(\phi) \tag{5.15}$$

$$y_{ps} = y_{pc} - \frac{w}{4}\sin(\alpha)\cos(\phi) \tag{5.16}$$

$$z_{ps} = z_{pc} - \frac{w}{4}\sin(\phi) \tag{5.17}$$

where x_{ps}, y_{ps}, and z_{ps} contain the shifted coordinates of each calculated point defining the profile; x_{pc}, y_{pc}, and z_{pc} are as previously defined; w is the profile width; and ϕ and α are the profile tilt and orientation angles as previously defined. Shifting the profiles yields a model with an ST inner-wall length of 20.55 mm and an ST outer-wall length of 38.54 mm, which are close to the values given in [57]. A view of the shifted profiles positioned along the length of the spiral curve is shown in Fig. 5.6.

5.3 Fabrication of an ST Phantom

A 3:1 scale 3D solid model was created in SolidWorks. The points generated for each ST profile were imported into SolidWorks as curves through XYZ points. A rectangular prism was created around the imported profiles, with the most basal

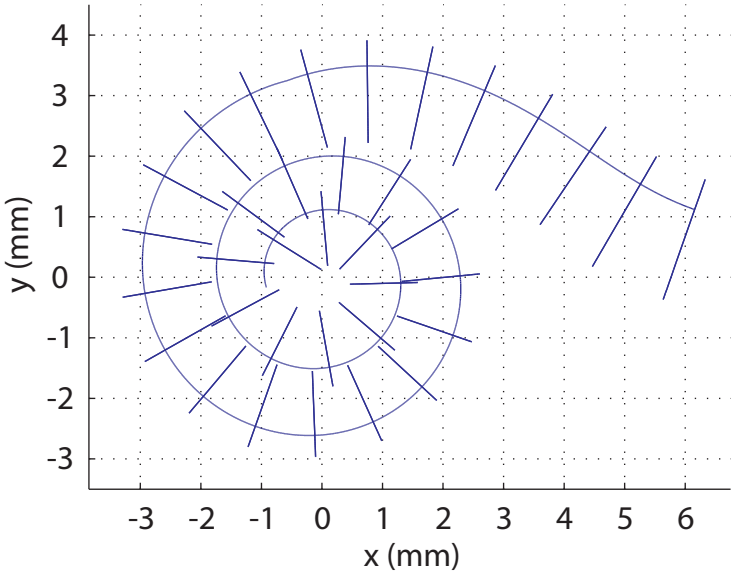

Figure 5.6. ST spiral curve with profiles shifted to decrease the length of the ST inner and outer walls. Compare with original model of Fig. 5.4 and intermediate model of Fig. 5.5.

profile positioned slightly outside of the prism. The ST channel was formed by creating a lofted cut connecting the profiles. Fig. 5.7 shows the imported profiles and channel formed by the lofted cut. The apical end of the channel was rounded by creating a sketch of half of the most apical channel profile and creating a 180° revolved cut, resulting in a semicircular end as shown in Fig. 5.8.

A 1 mm-diameter access hole was created from the face of the model extending into the semicircular end of the channel. This hole facilitates injection of soap solution into the channel, which is a standard method to lubricate phantoms for *in-vitro* insertions. The hole can be plugged after injecting the soap solution to avoid leaking. A mounting tab was created so that the phantom could be mounted for experiments. Using the generated 3D model, a phantom was manufactured by Javelin 3D (Park City, Utah) using an Objet 3D printer. Images of the phantom are shown in Fig. 5.9. The 1 mm access hole and mounting tab can be seen in several views. We used this phantom in the experiments described in Chapter 6.

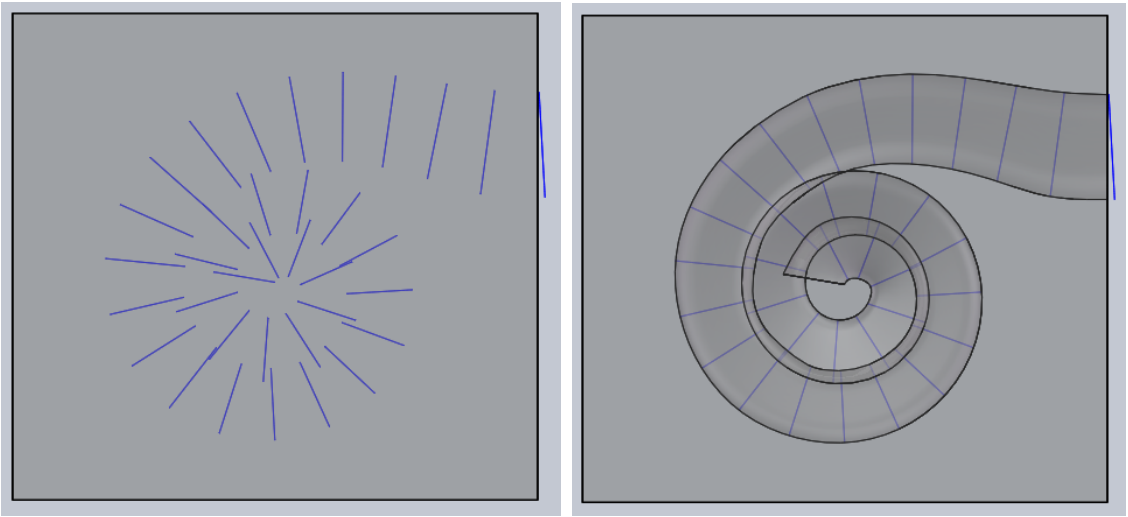

Figure 5.7. Views of SolidWorks model construction. (left) Imported channel profiles with surrounding rectangular prism. (right) Channel formed by connecting the profiles with a lofted cut.

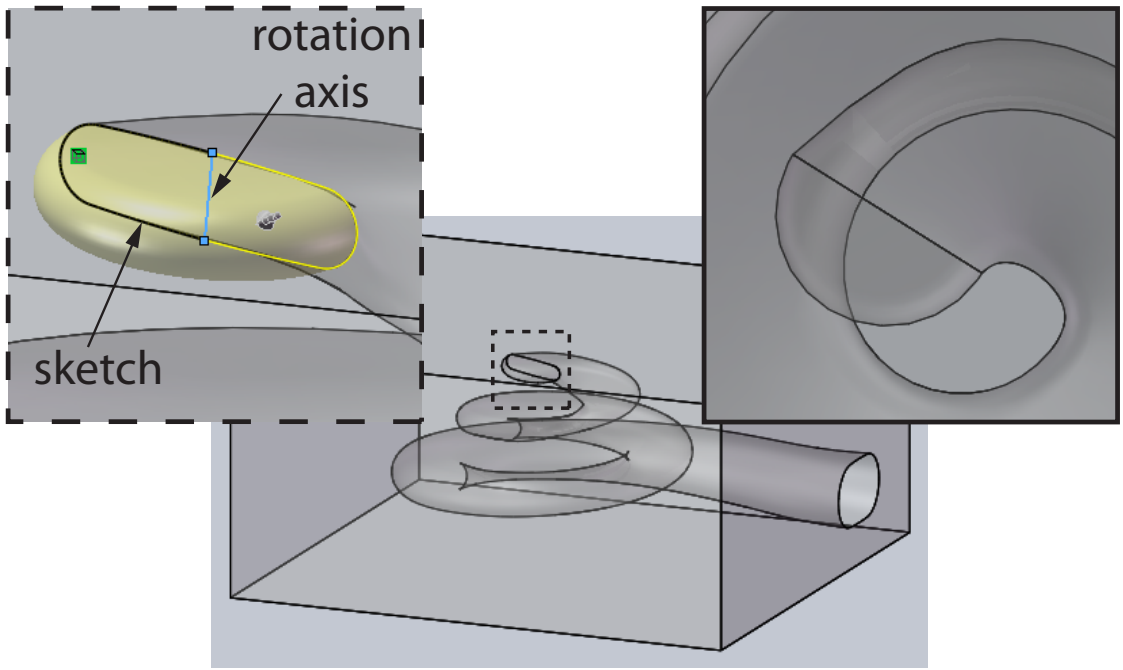

Figure 5.8. Semicircular cut created at the ST channel apical end. (inset, dashed border) Sketch and rotation axis used to create the revolved cut. (inset, solid border) Semicircular end.

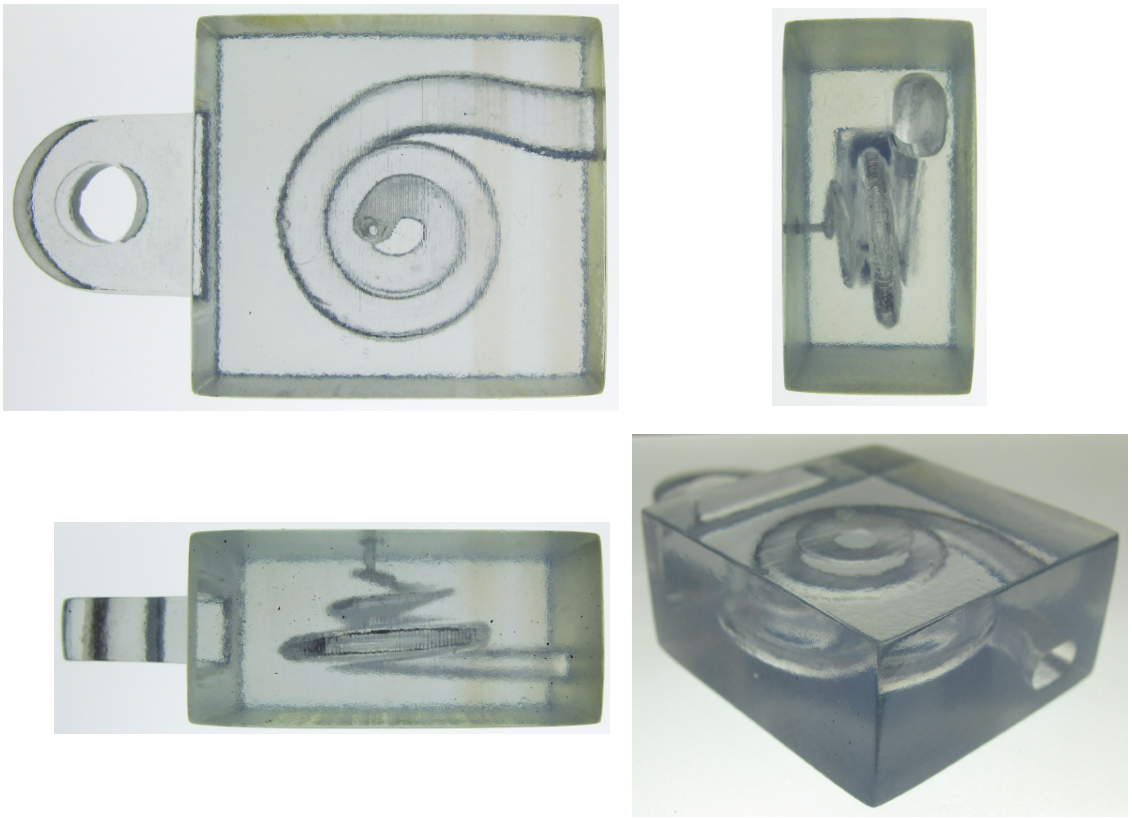

Figure 5.9. Fabricated 3:1 scale ST phantom. The rectangular prism has dimensions $31 \times 29 \times 15\,\mathrm{mm}^3$.

CHAPTER 6

EXPERIMENTS

The CI insertion experiments described in this chapter were performed to validate magnetic steering, compare insertion methods, and demonstrate proof of concept. We inserted a magnetically tipped implant prototype into a ST phantom with and without the aid of magnetic steering, and forces for each insertion were recorded. Comparison between nonguided and guided insertions using our prototype array provides a means to evaluate the potential effectiveness of magnetic steering. Our results demonstrate that guiding the tip using magnetic fields can decrease contact between the ST walls and implant and reduce insertion forces. A reduction in insertion force indicates that insertion trauma would likely be reduced during CI surgery. The magnetic guidance concepts and steering strategies (i.e., maximum-torque and maximum-field methods) used in these experiments are described in detail in Chapter 3.

6.1 Equipment

Thorlabs linear stages were used to insert the electrode prototype and position the manipulator relative to the ST. Two MTS50/M linear stages were used for implant insertion, and the RPM manipulator was attached to one MTS50/M-Z8 stage. Thorlabs mounting hardware (posts, post holders, etc.) was used to mount the linear stages and other experimental equipment to a Thorlabs metric optical table.

An ATI Nano17 6-axis force/torque sensor was used to collect force data during insertion experiments. The sensor and our sign convention for reporting forces measured along the sensor z-axis are shown in Fig. 6.1. Magnetic interactions between the manipulator magnet and force sensor had to be taken into account during

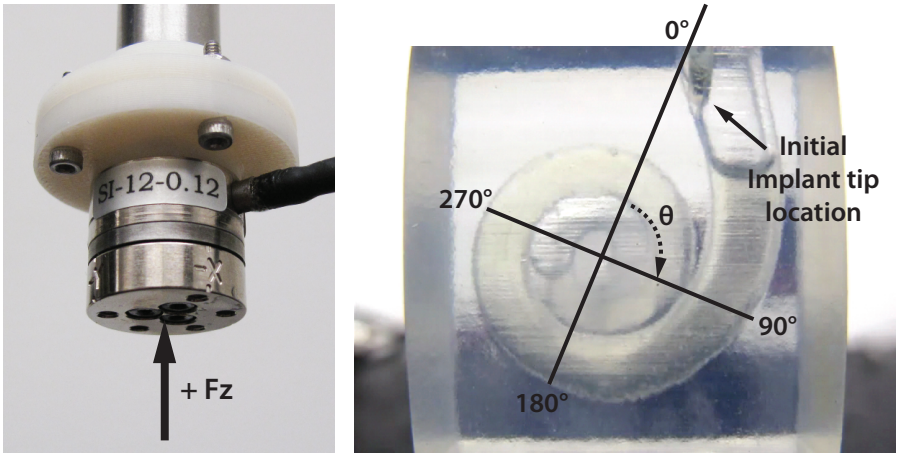

Figure 6.1. Experimental reporting conventions. (left) Nano17 force/torque sensor. Forces acting into the sensor along its z-axis (arrow) are reported as positive values in this Thesis. (right) Insertion angle based on the phantom model. The initial implant tip location is also shown.

experiments. Forces recorded during implant insertions do not only reflect contact between the implant and scala tympani; part of the total recorded insertion force is due to magnetic interactions between the force sensor and the manipulator magnet. Calibration force data can be recorded by removing the implant from the sensor and running the insertion experiment in the same way as if the implant were attached. This data can then be subtracted from the total force data recorded during implant insertions to yield a force profile that reflects interaction forces between the implant and ST. Calibration runs were performed for the experiments described in this chapter for insertions done using the maximum-torque and maximum-field steering strategies. We also had to be aware of sensor noise and temperature sensitivity. The minimum force resolution for the z-axis direction is 1/320 N. Taking readings with the sensor unloaded, we observed sensor noise on the order of ± 3 mN. This noise likely contributed to the presence of negative recorded force values, as is noted later in this chapter. To avoid data drift due to temperature fluctuation, care was taken to place the experimental setup in an area that was out of the path of direct flow from air vents. Care was also taken to touch the sensor as little as possible during the experimental procedure.

Custom mounting fixtures were designed to attach the sensor to a Thorlabs mounting post. Two mounting plates were modeled in SolidWorks and printed in ABS*plus*™ thermo-plastic using a Dimension 3D printer in the University of Utah Department of Mechanical Engineering. An exploded view of the sensor mounting assembly is shown in Fig. 6.2. The back mounting plate is first attached to the Thorlabs mounting post using an M6 screw. Three M2-0.40×6 screws are used to attach the Nano17 sensor to the front mounting plate. The documentation for the Nano17 sensor indicates that the interface depth for the M2 tapped holes is 3.5 mm and that this depth should not be exceeded to avoid sensor damage. Accordingly, the front plate was designed so that the M2 screws would reach a depth of 3 mm into the mounting holes with the plate attached to the sensor. The front and back plates are fastened together using four M2-0.40×10 screws and nuts. With the sensor attached to the mounting post, the whole assembly can be mounted to a Thorlabs linear stage using Thorlabs mounting and assembly hardware. Dimensioned drawings of the front and back mounting plates are shown in Fig. 6.3.

A CI holder was designed to attach the scaled-up implant prototype to the front (tool side) of the force sensor. The holder was modeled in SolidWorks and fabricated using the Dimension 3D printer. A dimensioned drawing of the implant holder is shown in Fig. 6.4. Three M2-0.40×6 screws are used to attach the holder to the force sensor. The thickness of the holder is 3.5 mm so that the mounting screws reach a depth of 2.5 mm into the sensor, not reaching or exceeding the maximum interface depth of 3.5 mm as indicated in the ATI documentation. The

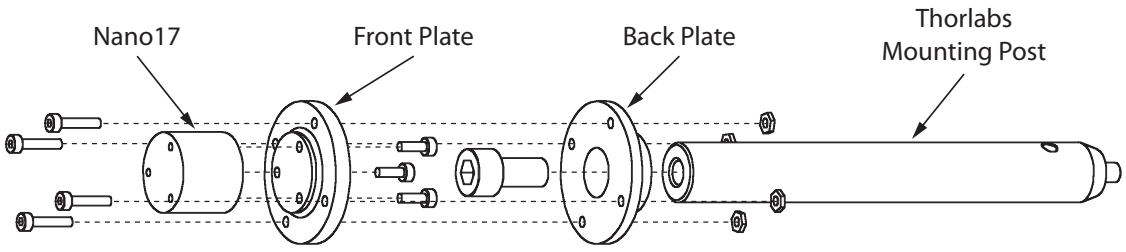

Figure 6.2. Assembly to mount the Nano17 sensor to a Thorlabs mounting post.

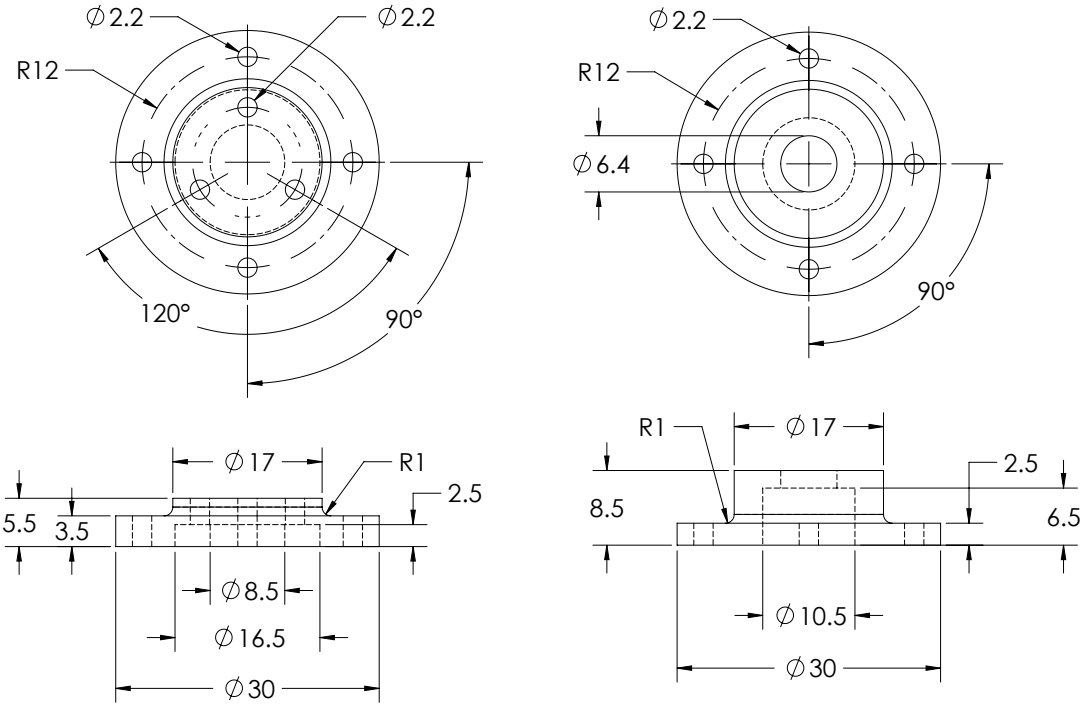

Figure 6.3. Mounting plates used to connect the Nano17 force/torque sensor to a Thorlabs mounting post. (left) Front mounting plate. (right) Back mounting plate.

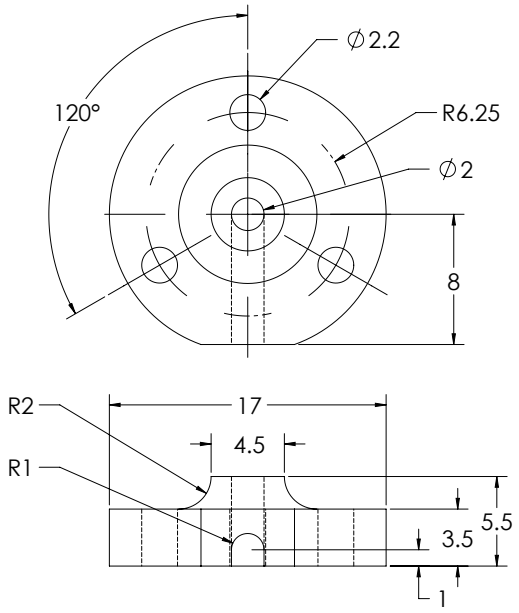

Figure 6.4. Implant holder used to mount the CI prototype to the Nano17 sensor.

groove on the bottom of the holder can accommodate extra electrode prototype length, allowing a portion of the implant to rest in the groove and protrude to the side of the sensor if extra length exists.

A rotating-permanent-magnet (RPM) manipulator prototype described in [50] was used in these experiments. The manipulator consists of a Delrin housing attached to a motor shaft with a permanent magnet placed in the housing. The cylinder magnet is 1 in in diameter and 1 in long, and has a hole along its cylindrical axis. The magnet is magnetized along its cylindrical axis of symmetry, which is referred to as axial magnetization, and its dipole strength is given in Chapter 3 of this Thesis. An incremental encoder was attached to the motor with a resolution of 2000 counts-per-revolution (after quadrature). An AMC DigiFlex Performance DPRALTE-020B080 digital servo drive was used to control the manipulator rotation position based on encoder counts, and was powered using a Gw Instek GPS-3303 power supply.

The ST phantom used in these experiments is the 3:1 phantom described in Chapter 5. The insertion angle based on the phantom model is shown in Fig. 6.1, and the initial implant tip position shown in the figure. The scaled-up implant prototype used with this phantom for these insertion experiments is described in Chapter 4.

Control for these experiments was implemented using C++ code. All aspects of the automated insertions were integrated into the code, including linear stage movement, manipulator rotation, and force recording.

6.2 Experiments

6.2.1 Setup

The experimental setup is shown in Figure 6.5. The manipulator was attached to a Thorlabs MTS50/M-Z8 linear stage mounted horizontally to the table. Two Thorlabs MTS50/M linear stages were mounted vertically in series, with one stage mounted to the platform of the other stage, allowing deeper implant insertion into the ST phantom with a total possible stage translation of 100 mm. The prototype attachment assembly with the scaled-up prototype was mounted to the stacked

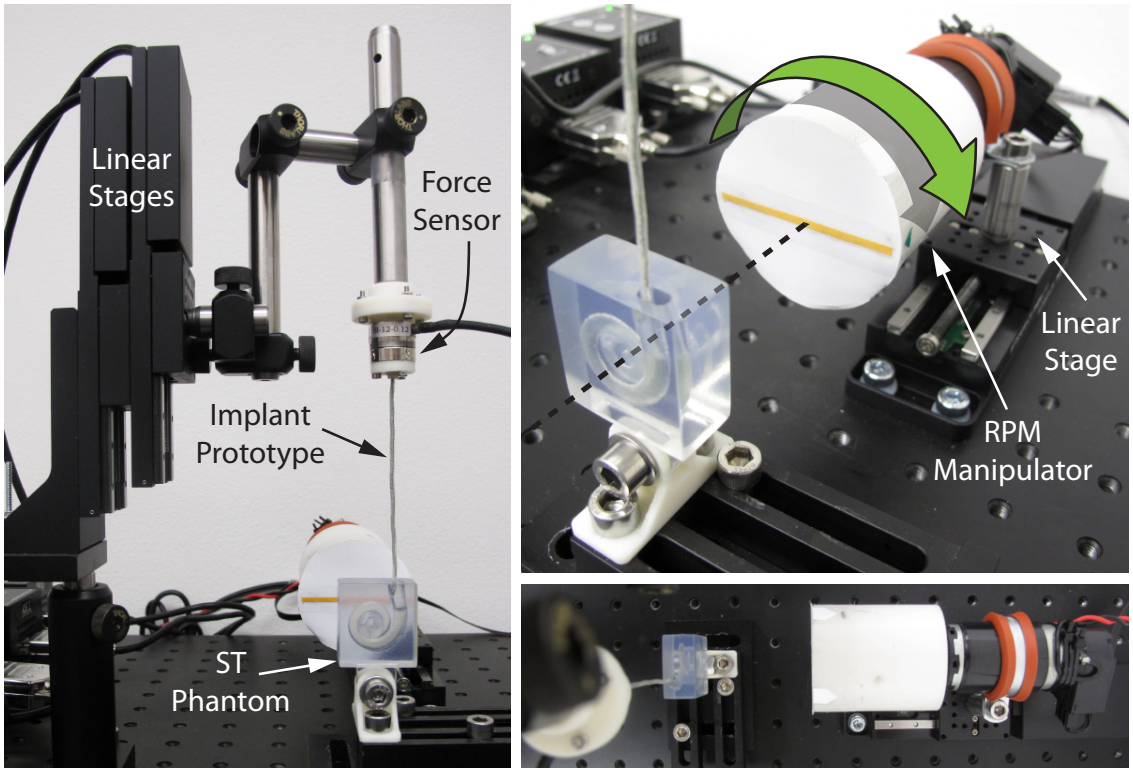

Figure 6.5. Experimental setup. (left) Front view. (top right) Oblique view. The dashed line shows that the manipulator rotation axis and cochlear central spiral axis are aligned. The curved arrow above the manipulator shows the manipulator rotation direction. (bottom right) Top view.

stages, with the array pointing downward. The 3:1 ST phantom was attached vertically to the table so that the entrance of the chamber was facing upward, with the ST chamber spiraling toward the manipulator magnet. Adjustments were made so that the manipulator rotation axis was aligned with the central spiral axis of the ST.

Both steering strategies discussed in Chapter 3 were implemented in these experiments using a series of discrete insertion steps. The steps were set up similarly for both strategies. The implant was initially positioned as shown in Fig. 6.5, with the vertical linear stage positions homed to 0 mm. For the first step of the maximum-torque method, the manipulator rotation was set to be horizontal, and the position of the stage to which it was attached was set to 0 mm. For the first step of the maximum-field method, the manipulator rotation was set to be vertical,

and the manipulator stage position was set to 50 mm, which positioned it as close as possible to the ST. For both methods, for each subsequent step the vertical stage positions were each increased by 0.5 mm, resulting in an implant insertion translation of 1 mm for each step. The manipulator rotation and manipulator stage translation were adjusted as necessary to orient the implant tip in the desired direction within the ST phantom to avoid wall contact. All three linear stage positions and the manipulator rotation (based on encoder counts) were recorded to a data file. The process was repeated for each step, inserting the implant in 1 mm increments until a total translation of 74 mm was achieved.

A file containing discrete positions was created for both guided insertion methods (i.e., maximum-torque, maximum-field). Several test insertion runs were performed, and adjustments were made in an attempt to optimize the insertion trajectories. For the maximum-torque method, the rotation angle and linear translation of the manipulator stage were adjusted to achieve a 90° angle between the manipulator magnetization direction and implant tip direction while avoiding contact between the implant tip and ST walls. A stripe attached to the manipulator (see Fig. 6.5) marked its magnetization direction, making it easier to see when a 90° angle had been achieved. For the maximum-field method, the manipulator was positioned as close as possible to the ST phantom, and only the manipulator rotation angle was adjusted to orient the tip away from the ST walls. A discrete-positions file was also created for nonguided insertions, with the implant inserted in 1 mm increments as in the other two cases. The manipulator was not translated or rotated during nonguided insertions.

6.2.2 Procedure

Before the experiments were started, all three linear stages were homed. In the home (zero) position, the implant was positioned with its tip resting inside the ST chamber, as shown in Fig. 6.5. The phantom was filled with soap solution. To orient the manipulator in its zero position, it was rotated manually so that the stripe was vertical. Supplying power to the AMC servo drive set this as the

zero-count position.

For a given insertion method, the respective discrete-positions file was read line by line. For each line, the motors were commanded to their stored positions. The step was considered complete when all three linear stages were within 0.001 mm of their desired step positions. For each run, the implant was advanced from 0 mm to 74 mm in 1 mm increments by simultaneously advancing each parallel-mounted stage by 0.5 mm for each step. The linear stages were run at their respective maximum velocities and accelerations. Before each insertion run in any insertion method, the manipulator was rotated to 500 encoder counts, rotating it 90° from its zero position. The manipulator is shown in this position in Fig. 6.5. Between insertion sets, a few drops of soap solution were added to the ST chamber to compensate for any that had been lost during the experiments.

Sensor data was collected after each discrete position along the insertion trajectory was reached. At each discrete point, 10 data points were collected and averaged, yielding one data point for each trajectory position, including the initial (0 mm) insertion position.

First, nonguided insertions were performed with the manipulator motor rotated 180° on its mounting post (pointed away from the ST phantom), positioning the manipulator magnet as far away from the implant as possible. Because of the large distance between the manipulator and implant with the manipulator in this position (close to 25 cm), magnetic effects between the manipulator and force sensor or implant were considered to be negligible. A series of insertion runs were performed. The manipulator was not rotated during these experiments, and the stage to which it was attached was kept in its zero position. After each run was complete, the two parallel linear stages were moved to their zero positions. The manipulator motor was then rotated on its mounting post to its original position, pointing toward the ST phantom (see Fig. 6.5), and the manipulator rotation was set to 500 counts. Insertion runs were performed using the maximum-torque method. After each run, the linear stages were sent to their zero positions and the manipulator was rotated to 500 counts. Insertion runs were then performed

using the maximum-field method. For each run, the first force/torque sensor data point was collected after the manipulator stage had reached its first position, with the manipulator positioned as close as possible to the ST phantom. After each run, the stages were sent to their zero positions and the manipulator was rotated to 500 counts. Calibration runs were then done for the maximum-torque and maximum-field methods so that magnet-sensor interaction forces could be subtracted from data taken with the implant in place. The number of runs averaged for each insertion method and calibration set are included in Table 6.1.

6.2.3 Results

The insertion force data for the experiments are shown in Figs. 6.6 and 6.7. For the maximum-torque and maximum-field insertion sets, the calibration runs were averaged for each set. The mean calibration values were then subtracted from the insertion data for each run in the set, giving calibrated force values reflecting implant-ST interaction forces. For each set, the standard deviation σ of force values for each insertion depth was then calculated using the calibrated insertion-run data. The solid vertical lines in Figs. 6.6 and 6.7(a) show the 95% (2σ) confidence interval for each data point. Insertion depths are based on implant translation from the initial implant position, which is shown in Fig. 6.1.

Figure 6.6 shows data for all 75 discrete insertion positions, including the initial implant position. The data shown represent the mean forces acting along the sensor z-axis for the three insertion methods used: nonguided, maximum-torque, and maximum-field. A notable spike in force for all three methods starts at an insertion depth of about 66 mm. This is likely associated with increased insertion friction and compression of the implant tip in the narrowing chamber. The eventual result

Table 6.1. Number of averaged insertion and calibration runs for each insertion method.

Insertion Method	# Runs with Implant	# Calibration Runs
Nonguided	6	N/A
Max-torque	7	6
Max-field	6	5

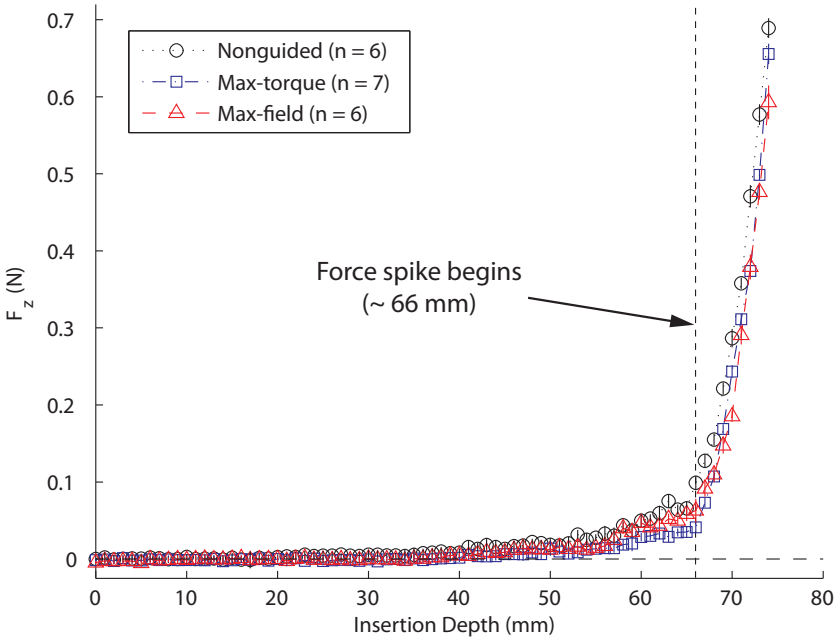

Figure 6.6. Experimental results showing data for the entire insertion range. The solid vertical bar with each data point shows the 95% (2σ) confidence interval (intervals are more visible in Fig. 6.7(a)). Insertion times were 112.5 s for the nonguided and maximum-field insertions, and 117.5 s for the maximum-torque insertions.

was implant buckling, which is shown in Fig. 6.8. Similar buckling occurred for all insertions, but occurred at slightly later insertion depths for the guided insertions as compared to the nonguided insertion. Bending the implant away from the ST outer wall may have decreased friction enough to allow slightly deeper insertion before buckling occurred. However, the implant was not narrow enough to allow a much deeper insertion and the tip became stuck between the lateral phantom walls, contributing to the increase in magnitude of recorded forces and buckling for all insertions. The final insertion depth corresponds to an angle of about 500° (see Fig. 6.1).

Figure 6.7 shows the data from Fig. 6.6 before the force spike occurs and in the region where all three insertion methods show near-zero forces, allowing force differences to be more easily distinguished. The vertical dashed lines in Fig. 6.7(a) show the approximate insertion depths where the implant first made contact with the cochlear outer wall during each insertion method. For the nonguided insertions,

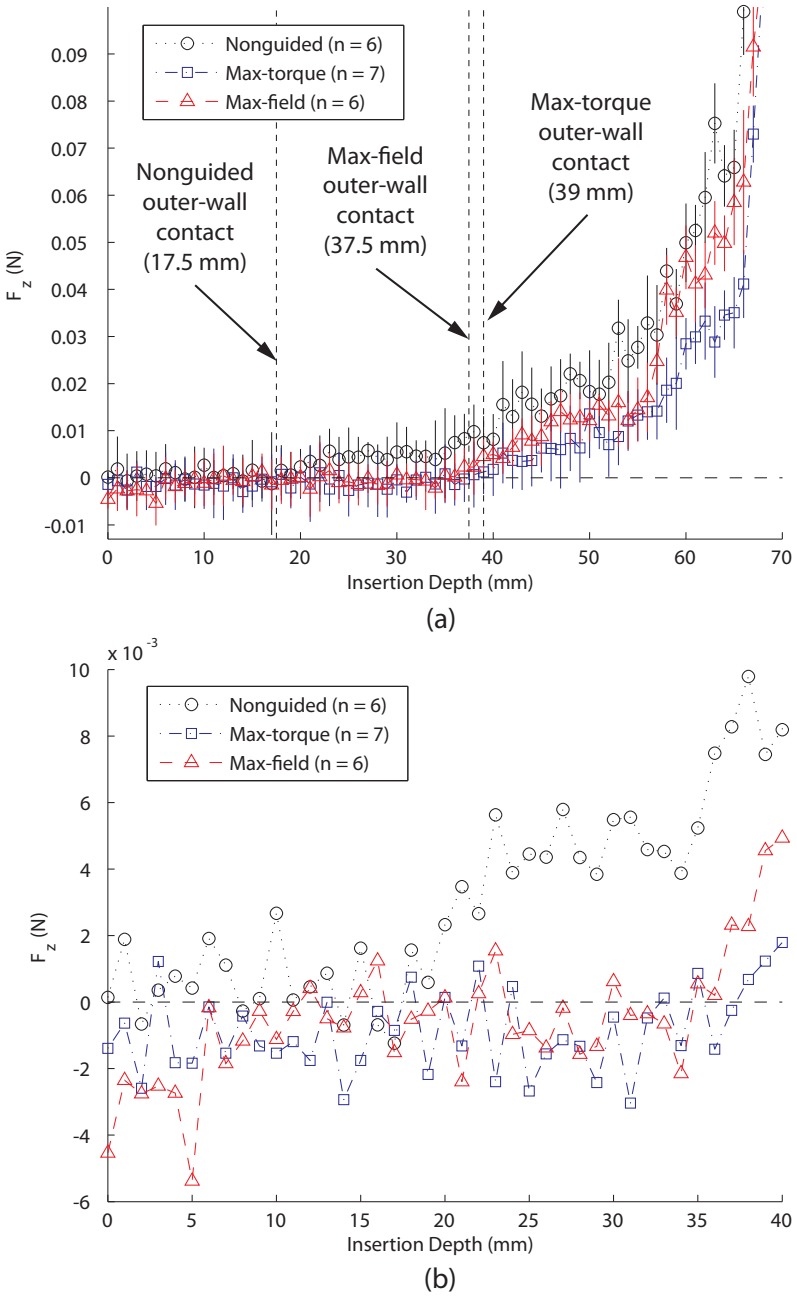

Figure 6.7. Detail plots of Fig. 6.6 shown so force differences in the regions are more easily distinguished. (a) Mean data markers for all three insertion methods shown for insertion depths from 0 mm to 66 mm. The solid vertical bar with each data point shows the 95% (2σ) confidence interval. Vertical dashed lines mark the approximate locations where the implant first made contact with the ST outer wall. (b) Mean data markers for all three insertion methods shown for insertion depths from 0 mm to 66 mm.

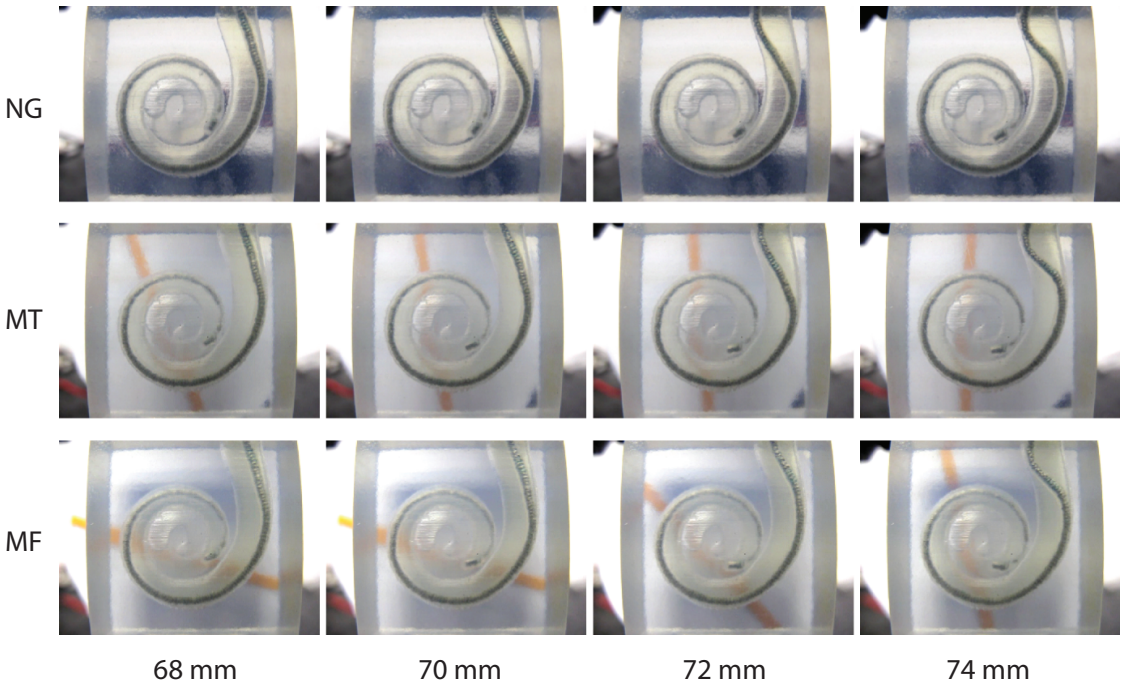

Figure 6.8. Examples of implant buckling at the end of insertion runs. Buckling can be seen near the entrance to the ST chamber (upper-right corner of the images). Insertion depths are shown beneath each image. NG = nonguided, MT = maximum-torque, MF = maximum-field.

outer-wall contact first occurred at about 17.5 mm. For the remainder of the insertion, the nonguided implant stays in contact with the ST outer wall. From the data, we see that as the nonguided implant tip slides against the ST outer wall, the mean force after 18 mm insertion depth gradually increases until there is a consistent visible gap between the nonguided and guided data. This is a logical trend since the friction between the implant and ST would increase the overall insertion force. At this point the guided implants have not yet made contact with the ST outer wall. During the maximum-field and maximum-torque insertions, the implant does not touch the wall until deeper insertion depths are reached. Fig. 6.9 shows the implant insertion through the first cochlear turn for the three steering methods. The nonguided implant slides against the outer wall, whereas the guided implants avoid outer-wall contact, conforming somewhat to the shape of the ST channel. The manipulator magnetization direction is marked by a straight line, which is

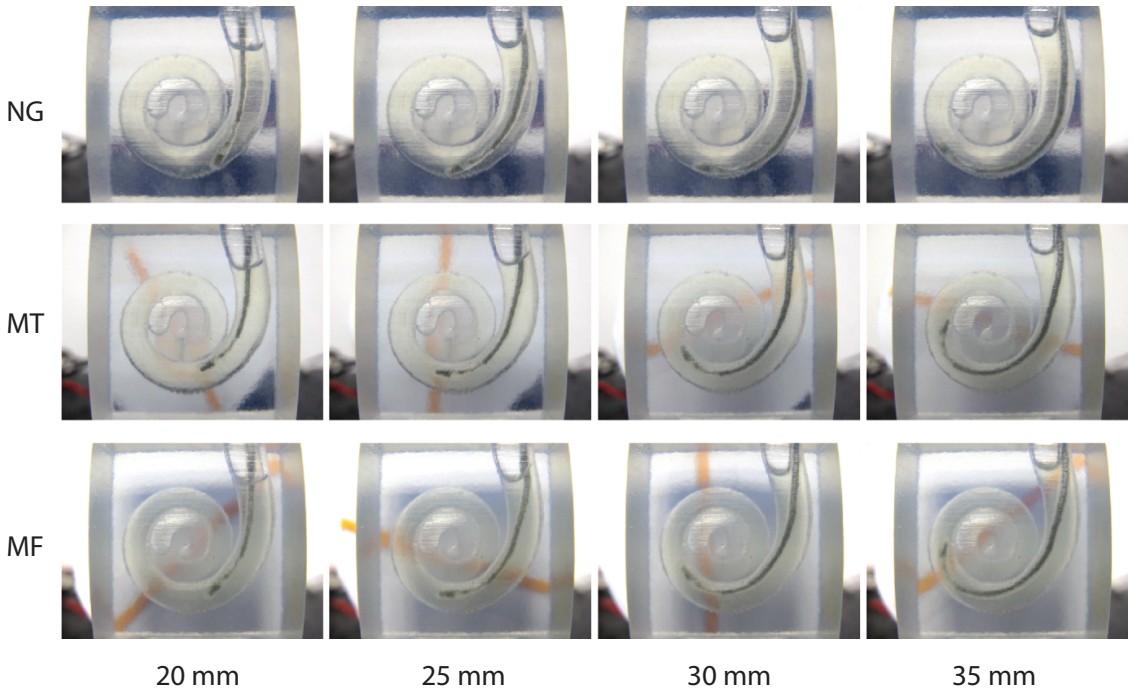

Figure 6.9. Image series showing the implant as it is advanced around the first cochlear turn. NG = nonguided, MT = maximum-torque, MF = maximum-field.

visible behind the ST. Note how the angle between the manipulator magnetization and implant tip is near perpendicular for the maximum-torque case, and is at a much shallower angle for the maximum-field case. Images of the implant contacting the ST outer wall for the three insertion methods are shown in Fig. 6.10. For the guided insertions, the physical bending characteristics of the implant dictate when it will make outer-wall contact; the more basal end of the implant is stiffer than the apical end, so the implant cannot continue to bend to follow the ST curve and is eventually advanced into the outer wall. For the maximum-field method, the implant first contacts the outer wall at an insertion depth of about 37.5 mm. For the maximum-torque method, first outer-wall contact occurs at a depth of about 39 mm. These observations are reflected in Fig. 6.7: the data for the insertions hover around zero until the outer-wall-contact insertion depths are reached. The forces then remain above zero and generally climb for both guided cases but are consistently lower than those of the nonguided insertions. Although the guided implant slides against the ST outer wall, note how the implant tip is directed away

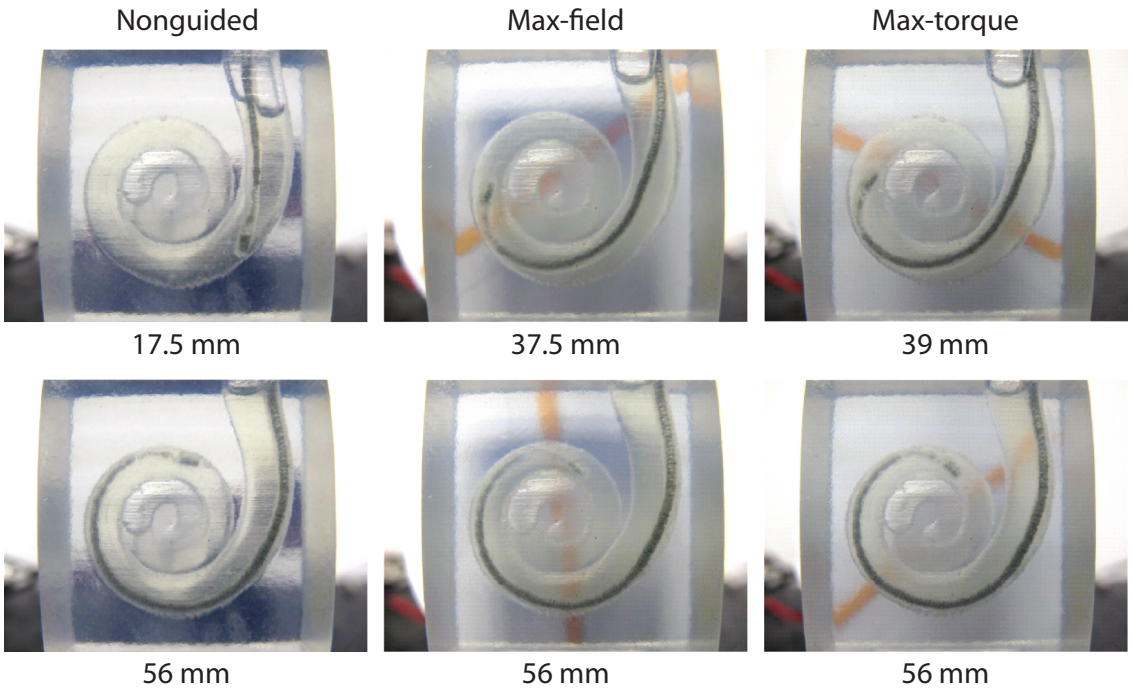

Figure 6.10. Images showing implant positions for selected insertion depths. The values below the images indicate the insertion depth. (top row) Approximate first instance of outer-wall contact. (bottom row) After outer-wall contact. Note how the tip of the implant is directed away from the outer wall in the maximum-torque and maximum-field images.

from the wall as shown in the bottom row of images in Fig. 6.10.

Note that many of the mean force values are negative for all three insertion methods in the region from 0 mm to 17 mm insertion depth, and for both guided methods until about 35 mm. There are several possible explanations for the occurrence of negative values: (1) Sensor noise causes the readings to fluctuate, even when no load is applied to the sensor. (2) The sensor readings for the guided methods have to be calibrated to compensate for magnetic interactions between the manipulator magnet and force sensor, and the calibrations may not perfectly compensate for these interactions. (3) Because of the dimensions of the ST, implant, and manipulator magnet, the implant tip is sometimes relatively far from the axial control region of the applied field. Magnetic forces could pull on the implant tip. (4) During guided insertions, the implant makes some contact with the ST inner wall (see Fig. 6.9). Forces from this contact could cause the implant to pull on the sensor

as the implant curls through the chamber. Negative forces due to precurled arrays contacting the ST inner wall have been noted in [1, 11], and a similar effect may have occurred when guiding our array. Forces related to the last two explanations could result in or be caused by contact between the implant and ST. We therefore treat any force deviation from 0 N as undesirable and use force magnitudes for our main analysis. Fig. 6.11 shows the mean forces plotted as magnitudes; any mean values which were previously negative are positive.

Quantitative comparisons between the insertion methods are presented in Fig. 6.12. We calculated the difference in mean force magnitude between nonguided and guided insertions using the formula

$$\Delta\,|\mathrm{F_z}| = |NG| - |G| \tag{6.1}$$

where NG and G are the nonguided and guided mean force magnitudes, respectively. The differences in mean z-axis force magnitudes between nonguided insertions and each guided insertion method are shown in Fig. 6.12(a). Values greater than zero indicate that the mean nonguided force magnitude is greater than the

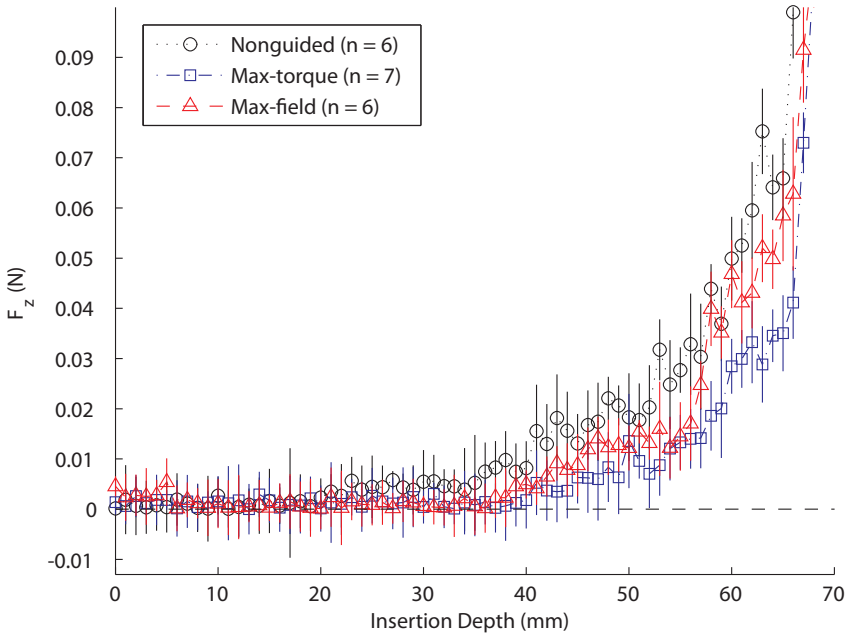

Figure 6.11. Experimental results plotted according to magnitude.

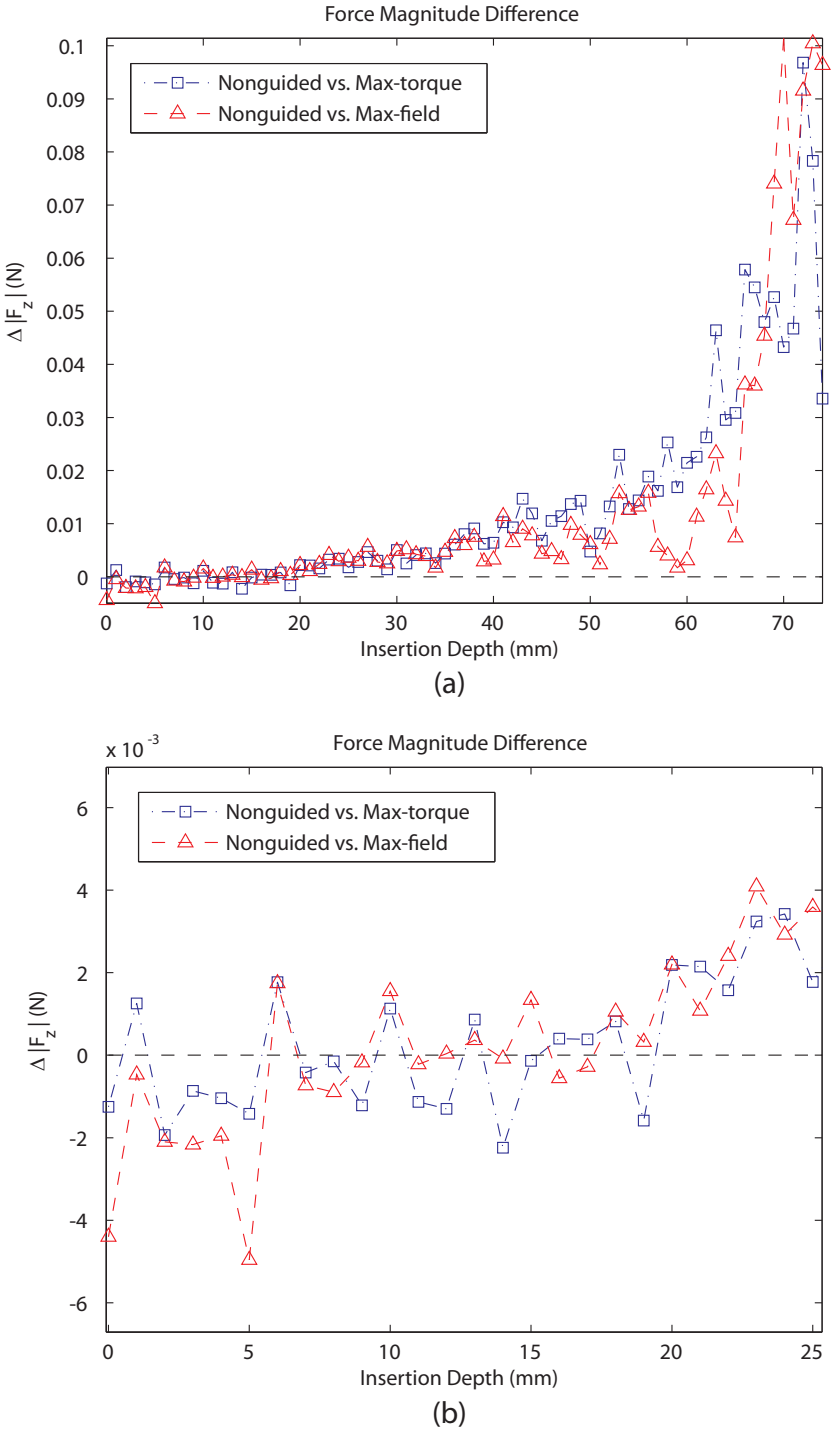

Figure 6.12. Difference between nonguided and guided insertion force magnitudes. (a) Force magnitude difference over the entire insertion range. (b) Detail showing data for the insertion range from 0 mm to 25 mm.

mean guided magnitude at that insertion depth, and values less than zero indicate that the nonguided magnitude is less than the guided magnitude. Fig. 6.12(b) is a detail of Fig. 6.12(a) and shows the data plotted from an insertion depth of 0 mm to 25 mm. Note that both negative and positive values exist in the region from 0 mm to 19 mm; the nonguided force magnitude is sometimes higher and sometimes lower than the guided force magnitudes. None of the three insertion methods shows a clear advantage in this region. However, the magnitude of the forces in this region are so small that they are of limited interest. After 20 mm, the magnitude difference values are consistently above zero, indicating that the mean nonguided force magnitude was always greater than the mean guided force magnitudes after this point. We therefore limit most of the remainder of our analysis to the data region from 20 mm through 74 mm, where a meaningful comparison between insertion methods can be made.

Both guided methods show general trends of increasing $\Delta |F_z|$ with deeper insertion depth. Over the insertion region from 20 mm through the end of the insertion, the maximum-torque method shows a mean decrease of $\Delta |F_z| = 0.0187$ N and a maximum decrease of $\Delta |F_z| = 0.0968$ N. The maximum-field method shows a mean decrease of $\Delta |F_z| = 0.0174$ N and a maximum decrease of $\Delta |F_z| = 0.101$ N. Fig. 6.13 shows the percentage of force decrease between the mean magnitude values of nonguided insertions and each guided insertion method. Percentages were calculated using the formula

$$\%\Delta |F_z| = \frac{|NG| - |G|}{|NG|} \times 100 \tag{6.2}$$

In the region from 20 mm to 74 mm, both methods show a gradual decrease in $\%\Delta |F_z|$ as insertion depth increases. The maximum-torque method shows a mean decrease of $\%\Delta |F_z| = 58.2$ and a maximum decrease of $\%\Delta |F_z| = 97.4$. In the same region, the maximum-field method shows a mean decrease of $\%\Delta |F_z| = 47.4$ and a maximum decrease of $\%\Delta |F_z| = 97.3$. These results are summarized in Table 6.2.

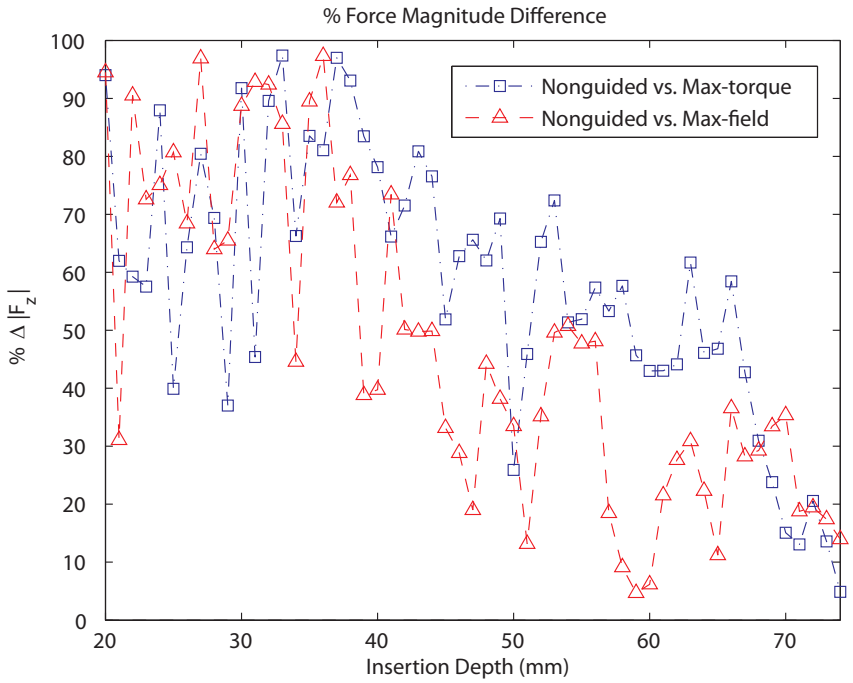

Figure 6.13. % Force magnitude difference between nonguided and guided insertions.

Table 6.2. Summary of experimental results. Values are for data magnitudes in the insertion range from 20 mm through 74 mm.

Comparison	**Mean** $\%\lvert\Delta F_z\rvert$	**Max** $\%\lvert\Delta F_z\rvert$	**Mean** $\lvert\Delta F_z\rvert$ **(N)**	**Max** $\lvert\Delta F_z\rvert$ **(N)**
Max-torque	58.2	97.4	0.0187	0.0968
Max-field	47.4	97.3	0.0174	0.101

6.2.4 Discussion

In our experiments, the implant prototype made significant contact with the ST outer wall during insertions for each insertion method. In the region from 0 mm to 17 mm shown in Fig. 6.7, all three insertion methods generally show near-zero values, with values both above and below 0 N. As previously discussed, during nonguided insertions, the implant tip first made contact with the ST outer wall at an insertion depth of about 17.5 mm, and the mean force from 18 mm through the rest of the insertion remains above zero as the implant slides against the wall. The force data for the guided insertions stay close to zero until their respective outer-wall-contact depths are reached. Thereafter, the forces for both methods increase

as the implant slides against the ST outer wall. As long as outer-wall contact is avoided, the force results show near-zero trends. This result is encouraging when evaluating the magnetically guided methods. During guided insertions and before outer-wall contact, the shape of the bent implant approximates the shape of the ST chamber. At the point where the bent implant shape no longer approximates that of the ST, the implant makes contact with the outer wall. If the implant were constructed and guided so that its bent shape approximated that of the ST channel during the entire insertion range, we could conceivably achieve near-zero insertion force throughout the insertion using magnetic guidance.

Although the implant shape did not approximate that of the ST for the entire insertion range in these experiments, the force results recorded after implant outer-wall contact indicate that magnetic guidance provided a decrease in insertion force. As discussed in Chapter 3, as a nonguided implant slides against the ST outer wall, the mechanical restoring torque due to the stiffness of the implant presses it against the wall. The normal force acting against the wall results in friction and increased insertion force. During magnetically guided insertions, the magnetic torque acting on the implant counteracts this mechanical restoring torque. The net effect is a decrease in normal force between the implant and ST wall. Friction is reduced, and the force required to advance the implant into the ST is decreased. Our experimental results support this theory. The mean force for both guided methods is consistently lower than that of the nonguided insertions, even in the region where the implant is in contact with the outer wall. Bending the implant away from the wall results in a decrease in friction and insertion force. As can be seen in Fig. 6.13, there is a gradual trend of decreasing $\%\Delta\,|F_z|$ as insertion depth increases. This trend is especially prominent after an insertion depth of about 37 mm, which corresponds to the approximate location where the implant first contacts the ST outer wall during guided insertions. As noted earlier, the implant contacts the ST outer wall during guided insertions because of the physical characteristics of the implant. At the point where the implant makes contact with the ST outer wall, the implant is being bent as far as possible with the applied magnetic field. As

the implant slides along the ST outer wall, a near-constant torque is applied to its tip. The mechanical restoring torque acting in the opposite direction, however, increases as the implant is advanced into the channel. The net effect is a gradual increase in frictional forces and a corresponding decrease in benefit due to magnetic bending.

A comparison between the maximum-torque and maximum-field data suggests that gradient forces present during the latter may increase insertion force. Non-guided insertions generally resulted in the highest force and the maximum-torque generally resulted in the lowest force, with the maximum-field force in between. This is especially visible in the data after an insertion depth of about 37 mm. As shown in Fig. 6.12, neither guided method shows a clear advantage over the other in the range between 20 mm and 37 mm. In Fig. 6.12(a) and (b), we see that from about 37 mm to about 68 mm, the maximum-torque method usually yields a greater decrease in force. Since the implant and manipulator dipoles are more aligned in the maximum-field method than in the maximum-torque method, this increase in maximum-field force could be due to field-gradient forces pulling the implant tip toward the manipulator. As previously noted, the insertion region from about 68 mm to 74 mm is the region in which implant buckling occurred, mostly due to channel constriction. Both guided insertion methods show a decrease in force as compared to the nonguided data. Interestingly, the maximum-torque method shows the greater benefit in this region. Since the implant tip became more constricted within the ST channel in this region, the gradient force may not have as much of an effect as in the region between 37 mm and 68 mm.

The possible effect of the gradient force increasing friction is not obvious in the region from 20 mm to 36 mm; the maximum-torque and maximum-field values in this region are similar. One reason why the maximum-field forces may increase relative to the maximum-torque forces after this point is that the implant tip is progressively moved closer to the manipulator. The ST spirals toward the manipulator, so as the implant is advanced through the chamber, the distance between the implant and manipulator decreases. This could cause the effect of

gradient force to become more significant.

As noted earlier in this chapter, the dimensions of the ST, manipulator, and implant are such that the implant tip is sometimes relatively far from the axial control region of the applied field. This is especially apparent when using the maximum-field method, with the manipulator positioned as close to the ST as possible. As can be seen in Fig. 6.7(b), all of the first six maximum-field forces (0 mm to 5 mm) are negative and have a generally larger magnitude than most of the other maximum-field values in the range from 0 mm to about 36 mm. This could be due to a component of gradient force pulling down on the implant tip. Fig. 6.14 shows how a gradient force could contribute to negative force readings. With the manipulator positioned close to the ST as in Fig. 6.14(b), we observed that the implant tip was directed outward, away from the manipulator. This tip magnet direction and location relative to the manipulator magnet is illustrated in Fig. 6.14(c), with the small magnet positioned above the axial control region and aligned with the field. The resulting gradient force pulls the magnet toward the large magnet and downward. The downward force component could pull on the

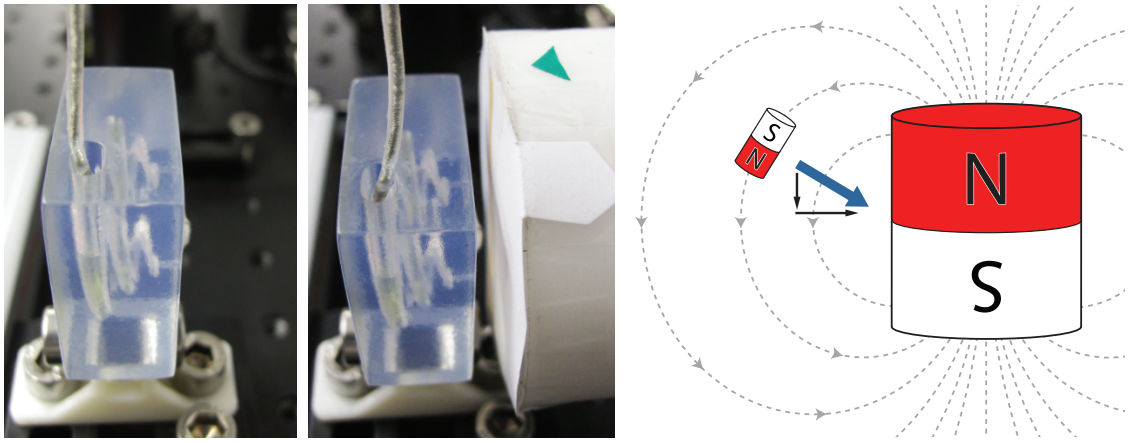

Figure 6.14. The possible effect of gradient forces outside of the applied field axial control region. (a) Implant tip inside the ST entrance with the manipulator positioned far from the phantom. (b) When the manipulator is positioned close to the phantom, the tip is pointed outward as it becomes more aligned with the applied field. (c) The vertical component of the resulting gradient force could pull the implant down, causing insertion force readings to become more negative.

implant and cause the force readings to become more negative than they otherwise would be. As the implant is advanced farther into the ST, the tip moves closer to the axial region of the field, and this type of effect likely decreases.

Insertion force results recorded during our experiments indicate that magnetically guiding a CI during surgery could reduce the incidence of intracochlear trauma. Compared to nonguided insertions using our prototype implant, we recorded a decrease in mean insertion forces when using both the maximum-torque and maximum-force magnetic steering methods. For the insertion region from 20 mm to 74 mm, the maximum-field method provided a mean force decrease of 47.4%, while the maximum-torque method provided a mean decrease of 58.2%. Zhang et al. conducted similar experiments using their prototype array described in Chapter 2, performing insertions with and without active implant bending. They report a prominent decrease in insertion force of 68% when using their path planning and implant bending strategy described in [8], which outperforms our current results. We expect to be able to achieve a greater reduction in force as we improve and enhance our experiments, as will be discussed in Chapter 7.

CHAPTER 7

CONCLUSIONS AND FUTURE WORK

Cochlear implants can provide hearing ability to individuals with sensorineural hearing loss. As a CI electrode array is inserted into the cochlea during surgery, it often damages delicate intracochlear structures. This damage could lead to loss of residual hearing, infection, and reduced implant performance. Several of the experimental electrode array designs discussed in Chapter 2 use active bending strategies to decrease the incidence of intracochlear trauma during insertion into the ST. In Chapter 3, we described a strategy that utilizes magnetic fields to achieve implant steering. A permanent magnet embedded in the tip of the electrode array can be manipulated during insertion using a magnetic field applied by a large external magnet. We created magnetically tipped prototype arrays, and fabrication details for a scaled-up prototype that we used for insertion experiments were given in Chapter 4. We inserted this prototype into a custom 3:1 scale ST phantom described in Chapter 5. To evaluate the benefit of magnetic steering, we recorded forces for insertions done with and without magnetic guidance and compared the results in Chapter 6. Our initial experimental results indicate that magnetically guiding a CI can decrease insertion forces, and thus could be a viable means to reduce intracochlear trauma during CI surgery. The results are promising, but the problem is not completely solved. Several improvements can be made to our implant design, and various insertion techniques will have to be explored before the use of magnetic guidance for CI insertion can be clinically realized.

In the experiments described in this thesis, we use force sensing only for analysis after the insertion has been performed. Real-time feedback of insertion forces during surgery could help achieve atraumatic implant placement without a precise

model of the cochlea. According to Rebscher et al. [3], preoperative imaging of the cochlea is not a current practice for CI surgery, so the patient's specific cochlear dimensions are not known during surgery. Force feedback could be used to adjust implant insertion trajectory to reduce trauma without knowing the patient's cochlear dimensions. Zhang et al. [9] used force feedback to regulate insertion speed during their experiments using a steerable prototype array. They report both an increase and a decrease in insertion force in their experimental results when using force feedback, and suggest they need to find an optimal force feedback control law to provide consistent results. However, some of their experiments show decreased insertion forces using force feedback. In future experiments using magnetic guidance for CI insertion, force feedback could be used to adjust insertion speed, implant translation, manipulator translation (i.e., distance from the ST), manipulator rotation, and insertion angle. Also, we only analyzed forces sensed along one axis of our force sensor. As suggested in [1], future work and insertion force analysis could include all data collected from our 6-axis force-torque sensor to provide more complete information about the overall insertion force.

The authors of [3] suggest that preoperative imaging would be useful to plan the surgery for each patient. They conducted insertion experiments with the Cochlear Contour Advance array using the AOS technique, and note that variability in human cochlea dimensions poses a challenge when using the AOS technique since early or late stylet removal could lead to increased intracochlear trauma. Cochlear dimension variability could pose a challenge for other insertion techniques, including magnetically guided CI surgery. In our experiments, we inserted our prototype implant into a transparent ST phantom using a series of discrete steps. For each step, we advanced the implant 1 mm farther into the phantom and set the position and rotation of our manipulator to visually bend the implant away from the ST walls. This would not be a viable technique in clinical practice, and we know of no method to provide safe and effective real-time cochlear imaging during surgery. Preoperative imaging could provide a model of the patient's cochlea that the surgeon could use to plan robotic-assisted CI surgery using magnetic guidance to

more effectively avoid contact between the implant and ST walls. A mathematical model of the ST could be used in future work to steer the implant based on known ST dimensions.

An accurate mathematical bending model of our implant would also be useful. Our current implant was made to qualitatively mimic some properties of a commercial free-fitting straight array. We do not have an accurate mathematical representation of our implant and its bending characteristics. Future work could include the development of a bending model for a magnetically guided implant. This model could be integrated into a robotic control algorithm to achieve correct manipulator placement and orientation during insertion for optimized insertion trajectory.

The implant used in our experiments mimics a straight, free-fitting electrode array, but its design could be improved in many ways. As discussed in Chapter 4, real CI arrays have a tapered shape; they are thicker at the base and thinner at the tip. Our array has a constant diameter. Future array prototypes should be tapered to more accurately model real arrays. The physical dimensions of our array limited insertion into our 3:1 ST model to a depth of about 560° (see Chapter 6). Tapering the array to have a tip with a smaller diameter (and a smaller embedded magnet) would allow deeper insertion into the ST, but the tapered shape would help provide the necessary basal stiffness to avoid buckling. The bent shape of the array can also be greatly improved. As discussed in Chapter 6, the shape of our bent array only approximated the shape of the ST well for a portion of the insertion. Ideally, as the implant is advanced through the ST and guided using magnetic fields, its bent shape should approximate the shape of the ST chamber. This would minimize wall contact. Implant prototypes used in future work should have a bent shape that approximates the ST spiral to minimize insertion forces.

Improved implant shape could also be achieved using wire coils embedded in the implant. Our current prototype has a permanent magnet embedded in its tip. In future arrays, the magnet could be replaced by a coil of wire that could be used as an electromagnet. Passing a current through the coil would generate a magnetic

field and allow magnetic steering. With no current passing through the coil, the implant would be unaffected by an applied magnetic field. Multiple coils could be positioned along the implant length and selectively energized to apply a specific torque to different points along the array length, yielding improved shape control. However, to generate useful levels of torque, significant current may be required, and heating may become a problem.

Ideally, the array should be precurled to hug the ST inner wall. Straight free-fitting arrays, like our prototype, do not achieve a perimodiolar placement within the ST. As can be seen in Fig. 6.8, the final position of a free-fitting array is against the ST outer wall. Magnetically tipped precurled arrays should be made for future magnetic guidance experiments. To avoid trauma to the basal portion of the ST as the precurled array is inserted, the array could be straightened and placed in a tube, and the tube could be advanced into the ST to a location near the first cochlear turn. The array could then be advanced out of the tube, and the applied magnetic field could be oriented to keep the implant from immediately bending toward the ST inner wall. As the implant tip approached the first cochlear turn, the magnetic field could be relaxed, allowing the implant to bend away from the wall. Advancing the array and further relaxing the applied magnetic field would allow the array to return to its spiral shape, avoiding wall contact and achieving a perimodiolar position. The tube could then be removed, allowing the basal portion of the array to rest in the ST channel.

The array design could also include the use of a stylet and improve the AOS technique. An AOS insertion is shown in Fig. 7.1. As can be seen in Fig. 7.1(c), the implant tip makes contact with the ST inner wall as it assumes its precurled shape. Fig. 7.2 is plot from [11]. The figure shows cumulative mean force curves for insertions done using the AOS and SIT techniques (these techniques are described in Chapter 2). Both [11] and [1] state that the negative force values for the AOS curve are likely due to implant contact with the ST inner wall, like the contact shown in Fig. 7.1(c). This contact could potentially damage structures along the ST inner wall, and all wall contact should be avoided. In future work using magnetic

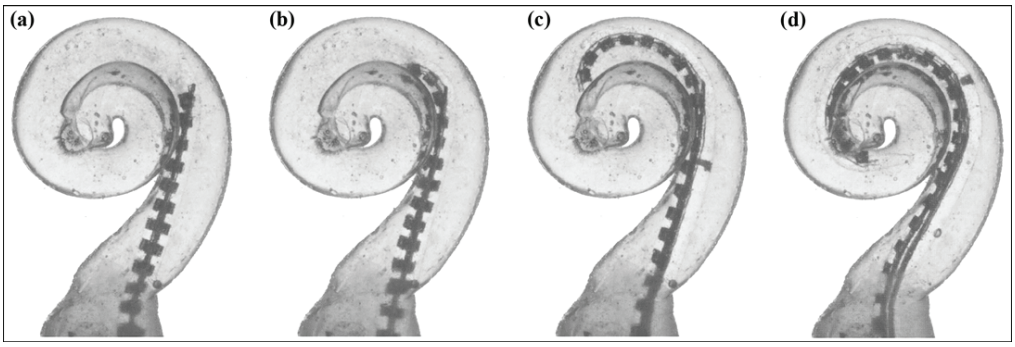

Figure 7.1. AOS insertion series from [3]. (a) Array and stylet are advanced into the ST. (b) Stylet is held in place while the array is advanced farther. (c)-(d) As it is inserted, the precurled array assumes its original shape to achieve a perimodiolar position and avoid contact with the ST outer wall.

fields, we could steer the tip of the implant during this portion of the insertion to avoid inner-wall contact.

The AOS force curve in Fig. 7.2 shows near-zero insertion forces for most of the insertion. As discussed in Chapter 6, our experimental results for magnetically guided insertions show near-zero forces for the portion of the insertion where the implant is not touching the ST outer wall (up to about 37 mm insertion depth,

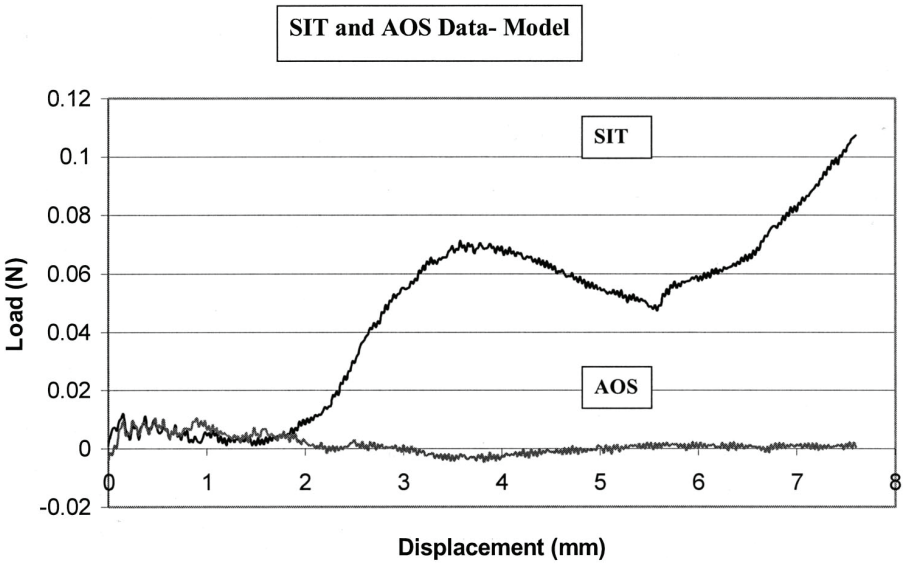

Figure 7.2. Plot from [11] (used with permission from John Wiley & Sons, Inc.) showing cumulative mean force curves for insertions done using the AOS and SIT techniques.

see Fig. 6.11). A goal of future work should be to achieve a near-zero insertion force profile using magnetic guidance. This could first be done using custom arrays of our own design to compare guided and nonguided insertions. Eventually, a 1:1 scale implant will have to be fabricated and compared with insertion results for commercial arrays to evaluate the possible advantages of magnetic steering. This will likely include the use of both synthetic ST phantoms and, eventually, cadaver temporal bones for clinical feasibility studies.

Clearly, much work needs to be done before magnetic guidance of CI arrays can be implemented clinically. Several improvements to our current array design and steering strategy can be made to further reduce insertion forces. Although improvements can be made, the experiments described in this thesis demonstrate the potential of magnetic steering to decrease insertion forces during CI insertion. These promising results represent the first steps toward improved cochlear implant insertion using magnetic guidance.

REFERENCES

[1] Todd, C. A., Naghdy, F., and Svehla, M. J., 2007. "Force application during cochlear implant insertion: An analysis for improvement of surgeon technique." *IEEE Trans. Biomedical Engineering,* **54**(7), pp. 1247–1255.

[2] Gstoettner, W., Franz, P., Hamzavi, J., H. Plenk, J. W. B., and Czerny, C., 1999. "Intracochlear position of cochlear implant electrodes." *Acta Otolaryngol,* **119**(2), pp. 229–233.

[3] Rebscher, S. J., Hetherington, A., Bonham, B., Wardrop, P., Whinney, D., and Leake, P. A., 2008. "Considerations for design of future cochlear implant electrode arrays: Electrode array stiffness, size, and depth of insertion." *J. Rehabilitation Research and Development,* **45**(5), pp. 731–748.

[4] Briggs, R. J. S., Tykocinski, M., Saunders, E., Hellier, W., Dahm, M., Pyman, B., and Clark, G. M., 2001. "Surgical implications of perimodiolar cochlear implant electrode design: avoiding intracochlear damage and scala vestibuli insertion." *Cochlear Implants Int.,* **2**(2), pp. 135–149.

[5] Adunka, O., and Kiefer, J., 2006. "Impact of electrode insertion depth on intracochlear trauma." *Otolaryngology - Head Neck Surg.,* **135**(3), pp. 374–382.

[6] Majdani, O., Schurzig, D., Hussong, A., Rau, T., Wittkopf, J., Lenarz, T., and Labadie, R. F., 2010. "Force measurement of insertion of cochlear implant electrode arrays in vitro: comparison of surgeon to automated insertion tool." *Acta Oto-Laryngol.,* **130**(1), pp. 31–36.

[7] Rebscher, S. J., Heilmann, M., Bruszewski, W., Talbot, N. H., Snyder, R. L., and Merzenich, M. M., 1999. "Strategies to improve electrode positioning and safety in cochlear implants." *IEEE Trans. Biomedical Engineering,* **46**(3), pp. 340–352.

[8] Zhang, J., Roland Jr., J. T., Simaan, N., and Manolidis, S., 2006. "A pilot study of robot-assisted cochlear implant surgery using steerable electrode arrays." In MICCAI 2006, LNCS 4190, pp. 33–40.

[9] Zhang, J., Roland Jr., J. T., Manolidis, S., and Simaan, N., 2009. "Optimal path planning for robotic insertion of steerable electrode arrays in cochlear implant surgery." *ASME J. Medical Devices,* **3**(011001).

[10] Zhang, J., Bhattacharyya, S., and Simaan, N., 2009. "Model and parameter identification of friction during robotic insertion of cochlear-implant electrode arrays." In IEEE Int. Conf. Robotics and Automation, pp. 3528–3533.

[11] Roland Jr., J. T., 2005. "A model for cochlear implant electrode insertion and force evaluation: Results with a new electrode design and insertion technique." *The Laryngoscope,* **115**(8), pp. 1325–1339.

[12] Schurzig, D., Labadie, R. F., Hussong, A., Rau, T. S., and Webster III, R. J., 2010 (*in press*). "Design of a tool integrating force sensing with automated insertion in cochlear implantation." *IEEE Trans. Mechatronics.*

[13] Tykocinski, M., Cohen, L. T., Pyman, B. C., Roland Jr., T., Treaba, C., Palamara, J., Dahm, M. C., Shepherd, R. K., Xiu, J., Cowan, R. S., Cohen, N. L., and Clark, G. M., 2000. "Comparison of electrode position in the human cochlea using various perimodiolar electrode arrays." *Am. J. Otology,* **21**(2), pp. 205–211.

[14] Wardrop, P., Whinney, D., Rebscher, S. J., Roland Jr., J. T., Luxford, W., and Leake, P., 2005. "A temporal bone study of insertion trauma and intracochlear position of cochlear implant electrodes. i: Comparison of Nucleus banded and Nucleus Contour^{TM}electrodes." *Hearing Research,* **203**(1-2), pp. 54–67.

[15] Wardrop, P., Whinney, D., Rebscher, S. J., Luxford, W., and Leake, P., 2005. "A temporal bone study of insertion trauma and intracochlear position of cochlear implant electrodes. ii: Comparison of spiral clarion^{TM}and hifocus ii^{TM}electrodes." *Hearing Research,* **203**(1-2), pp. 68–79.

[16] Adunka, O., Unkelbach, M. H., Mack, M., Hambek, M., Gstoettner, W., and Kiefer, J., 2004. "Cochlear implantation via the round window membrane minimizes trauma to cochlear structures: A histologically controlled insertion study." *Acta Otolaryngol,* **124**(7), pp. 807–812.

[17] Roland, P. S., Gstöttner, W., and Adunka, O., 2005. "Method for hearing preservation in cochlear implant surgery." *Operat. Tech. Otolaryngol. Head Neck Surg.,* **16**(2), pp. 93–100.

[18] von Ilberg, C., Kiefer, J., Tillein, J., Pfenningdorff, T., Hartmann, R., Stürzebecher, E., and Klinke, R., 1999. "Electric-acoustic stimulation of the auditory system. New technology for severe hearing loss." *ORL,* **61**(6), pp. 334–340.

[19] Paprocki, A., Biskup, B., Kozłowska, K., Kuniszyk, A., Bien, D., and Niemczyk, K., 2004. "The topographical anatomy of the round window and related structures for the purpose of cochlear implant surgery." *Folia Morphol.,* **63**(3), pp. 309–312.

[20] Adunka, O., Pillsbury, H. C., and Kiefer, J., 2006. "Combining perimodiolar electrode placement and atraumatic insertion properties in cochlear implantation - fact or fantasy?." *Acta Oto-Laryngologica,* **126**(5), pp. 475–482.

[21] Roland, P. S., Wright, C. G., and Isaacson, B. I., 2007. "Cochlear implant electrode insertion: The round window revisited." *The Laryngoscope,* **117**(8), pp. 1397–1402.

[22] Nadol Jr., J. B., Shiao, J. Y., Burgess, B. J., Ketten, D. R., Eddington, D. K., Gantz, B. J., Kos, I., Montandon, P., Coker, N. J., Roland Jr., J. T., and Shallop, J. K., 2001. "Histopathology of cochlear implants in humans." *Ann. Otology, Rhinology & Laryngology,* **110**(9), pp. 883–891.

[23] Gani, M., Valentini, G., Sigrist, A., Kós, M.-I., and Böex, C., 2007. "Implications of deep electrode insertion on cochlear implant fitting." *J. Assoc. Res. Otolaryngol.,* **8**(1), pp. 69–83.

[24] Gstoettner, W. K., Adunka, O., Franz, P., Hamzavi, J., H. Plenk, J., Susani, M., Baumgartner, W., and Kiefer, J., 2001. "Perimodiolar electrodes in cochlear implant surgery." *Acta Otolaryngol,* **121**(2), pp. 216–219.

[25] Balkany, T. J., Eshraghi, A. A., and Yang, N., 2002. "Modiolar proximity of three perimodiolar cochlear implant electrodes." *Acta Otolaryngol,* **122**(4), pp. 363–369.

[26] Eshraghi, A. A., Yang, N. W., and Balkany, T. J., 2003. "Comparative study of cochlear damage with three perimodiolar electrode designs." *Laryngoscope,* **113**(3), pp. 415–419.

[27] Bell, T. E., Wise, K. D., and Anderson, D. J., 1998. "A flexible micromachined electrode array for a cochlear prosthesis." *Sensors and Actuators A,* **66**, pp. 63–69.

[28] Bhatti, P. T., Arcand, B. Y., Wang, J., Butala, N. V., Friedrich, C. R., and Wise, K. D., 2003. "A high-density electrode array for a cochlear prosthesis." In Int. Conf. Solid-State Sensors, Actuators and Microsystems, Vol. 2, pp. 1750–1753.

[29] Wang, J., Gulari, M., Bhatti, P., Arcand, B. Y., Beach, K., Friedrich, C., and Wise, K. D., 2005. "A cochlear electrode array with built-in position sensing." In Int. Conf. Micro Electro Mechanical Systems, pp. 786–789.

[30] Tang, Y., Aslam, D. M., Wang, J., and Wise, K. D., 2005. "Technology and integration of poly-crystalline diamond piezoresistive position sensor for cochlear implant probe." In Int. Conf. Solid-State Sensors, Actuators and Microsystems, Vol. 1, pp. 543–546.

[31] Wang, J., Gulari, M. N., and Wise, K. D., 2006. "A parylene-silicon cochlear electrode array with integrated position sensors." In IEEE EMBS Annual Int. Conf., pp. 3170–3173.

[32] Bhatti, P. T., and Wise, K. D., 2006. "A 32-site 4-channel high-density electrode array for a cochlear prosthesis." *IEEE J. Solid-State Circuits,* **41**(12), pp. 2965–2973.

[33] Wu, J., Yan, L., Xu, H., Tang, W. C., and Zeng, F.-G., 2005. "A curvature-controlled 3d micro-electrode array for cochlear implants." In TRANSDUCERS '05. 13^{th} Int. Conf. Solid-State Sensors, Actuators and Microsystems, Vol. 2, pp. 1636–1639.

[34] Mirzadeh, H., and Abbasi, F., 2004. "Segmented detachable structure of cochlear-implant electrodes for close-hugging engagement with the modiolus." *J. Biomedical Materials Research,* **68B**(2), pp. 191–198.

[35] Chen, B. K., Kha, H. N., and Clark, G. M., 2007. "Development of a steerable cochlear implant electrode array." In IFMBE Int. Conf. Biomed. Eng., Vol. 15, pp. 607–610.

[36] Hussong, A., Rau, T., Eilers, H., Baron, S., Heimann, B., Leinung, M., Lenarz, T., and Majdani, O., 2008. "Conception and design of an automated insertion tool for cochlear implants." In EMBS Ann. Int. Conf. IEEE, pp. 5593–5596.

[37] Zhang, J., Roland Jr., J. T., Simaan, N., and Manolidis, S., 2008. "Path planning and workspace determination for robot-assisted insertion of steerable electrode arrays for cochlear implant surgery." In Medical Image Computing and Computer-Assisted Intervention, Vol. 5242, pp. 692–700.

[38] Judy, J. W., Muller, R. S., and Zappe, H. H., 1995. "Magnetic microactuation of polysilicon flexure structures." *J. Microelectromechanical Systems,* **4**(4), pp. 162–169.

[39] Tunay, I., 2004. "Modeling magnetic catheters in external fields." In IEEE EMBS Annual Int. Conf., Vol. 1, pp. 2006–2009.

[40] Tunay, I., 2004. "Position control of catheters using magnetic fields." In IEEE Int. Conf. Mechatronics, pp. 392–397.

[41] Eng, M. J., Viswanathan, R. R., Werp, P. R., Tunay, I., Pandey, A. K., and Munger, G. T., 2008. Electrophysiology catheter United States Patent, Patent No. US 7,346,379 B2,.

[42] Garibaldi, J. M., and Blume, W. M., 2006. Method of and apparatus for navigating medical devices in body lumens by a guide wire with a magnetic tip United States Patent, Patent No. US 7,066,924,.

[43] Garibaldi, J. M., Sell, J. C., Hastings, R. N., and Hall, A. F., 2004. Magnetically navigated pacing leads, and methods for delivering medical devices United States Patent, Patent No. US 6,817,364 B2,.

[44] Garibaldi, J. M., and Blume, W. M., 2002. Methods of and apparatus for treating vascular defects United States Patent, Patent No. US 6,375,606 B1,.

[45] Werp, P. R., Ritter, R. C., and Blume, W. M., 1999. Method of and apparatus for intraparenchymal positioning of medical devices United States Patent, Patent No. 5,931,818,.

[46] Maghribi, M. N., Krulevitch, P. A., Davidson, J. C., and Hamilton, J. K., 2006. Implantable devices using magnetic guidance United States Patent Application Publication, US2006/0052656 A1,.

[47] Kha, H. N., and Chen, B. K., 2006. "Determination of frictional conditions between electrode array and endosteum lining for use in cochlear implant models." *J. Biomechanics,* **39**(9), pp. 1752–1756.

[48] Warren, F. M. Department of Otolaryngology, Division of Otology and Skull Base Surgery, Oregon Health and Science University Personal correspondence.

[49] Abbott, J. J. Assistant Professor, Department of Mechanical Engineering, University of Utah Personal correspondence.

[50] Fountain, T. W. R., Kailat, P. V., and Abbott, J. J., 2010. "Wireless control of magnetic helical microrobots using a rotating-permanent-magnet manipulator." In IEEE Int. Conf. Robotics and Automation, pp. 576–581.

[51] Abbott, J. J., Ergeneman, O., Kummer, M. P., Hirt, A. M., and Nelson, B. J., 2007. "Modeling magnetic torque and force for controlled manipulation of soft-magnetic bodies." *IEEE Trans. Robotics,* **23**(6), pp. 1247–1252.

[52] Rebscher, S. J., Talbot, N., Bruszewski, W., Heilmann, M., Brasell, J., and Merzenich, M. M., 1996. "A transparent model of the human scala tympani cavity." *J. Neuroscience Methods,* **64**(1), pp. 105–114.

[53] Cohen, L. T., Xiu, J., Xu, S. A., and Clark, G. M., 1996. "Improved and simplified methods for specifying positions of the electrode bands of a cochlear implant array." *American J. Otology,* **17**(6), pp. 859–865.

[54] Yoo, S. K., Wang, G., Rubinstein, J. T., Skinner, M. W., and Vannier, M. W., 2000. "Three-dimensional modeling and visualization of the cochlea on the internet." *IEEE Trans. Information Technology in Biomedicine,* **4**(2), pp. 144–151.

[55] Gulya, A. J., and Steenerson, R. L., 1996. "The scala vestibuli for cochlear implantation: An anatomic study." *Ann. Otolaryngol. Head Neck Surg.,* **122**(2), pp. 130–132.

[56] Wysocki, J., 1999. "Dimensions of the human vestibular and tympanic scalae." *Hearing Research,* **135**(1-2), pp. 39–46.

[57] Kawano, A., Sheldon, H. L., and Clark, G. M., 1996. "Computer-aided three-dimensional reconstruction in human cochlear maps: Measurement of the lengths of organ of Corti, outer wall, inner wall, and Rosenthal's canal." *Ann. Otol. Rhinol. Laryngol.,* **105**(9), pp. 701–709.